The observational characteristics of accreting white dwarfs and their connection to Type Ia supernovae

Jere Kuuttila

München 2021

The observational characteristics of accreting white dwarfs and their connection to Type Ia supernovae

Jere Kuuttila

Dissertation
an der Fakultät für Physik
der Ludwig–Maximilians–Universität
München

vorgelegt von
Jere Kuuttila
aus Seinäjoki, Finnland

München, den 12.3.2021

Erstgutachter: Prof. Dr. Rashid Sunyaev
Zweitgutachter: Prof. Dr. Werner Becker
Tag der mündlichen Prüfung: 18.5.2021

Contents

Zusammenfassung **xi**

Summary **xiii**

1 Introduction **1**
1.1 Type Ia supernovae . . . 1
1.1.1 Type Ia supernova progenitors . . . 3
1.2 Accreting white dwarfs . . . 5
1.2.1 Nuclear burning white dwarfs . . . 8
1.2.2 Symbiotic binaries . . . 12
1.3 This thesis . . . 15

2 Excluding SSSs as SNe Ia progenitors **17**
2.1 Introduction . . . 18
2.2 Observations . . . 20
2.3 Methods . . . 20
2.3.1 Spectra of the remnants . . . 20
2.3.2 Simulations . . . 23
2.4 Results . . . 24
2.5 Discussion . . . 29

3 The symbiotic binary LIN 358 **33**
3.1 Introduction . . . 34
3.2 LIN 358 overview . . . 35
3.2.1 Mass estimation . . . 35
3.2.2 Orbital parameters . . . 36
3.3 Observations . . . 37
3.4 Data . . . 39
3.4.1 He II 4686 Å . . . 39
3.4.2 He I lines . . . 40
3.4.3 Balmer lines . . . 40
3.4.4 [Fe X] 6374 Å . . . 41
3.4.5 O VI 6830 Å Raman feature . . . 41

3.5 Cloudy simulations setup . . . 42
3.5.1 Density structure . . . 43
3.6 Results . . . 45
3.6.1 Colour temperature of the white dwarf . . . 46
3.6.2 White dwarf luminosity . . . 48
3.6.3 Mass-loss rate of the donor star . . . 48
3.6.4 Structure of the emission regions of principal lines . . . 49
3.7 Discussion . . . 49
3.7.1 Low excitation lines . . . 52
3.7.2 Mass accretion rate . . . 53
3.7.3 Circumstellar absorption . . . 55
3.7.4 LIN 358 in the context of the origin of SN Ia . . . 56
3.8 Conclusions . . . 57

4 Observational properties of symbiotic binaries 59
4.1 Introduction . . . 60
4.2 Model description . . . 61
4.2.1 Cloudy simulations . . . 61
4.2.2 Binary parameters . . . 62
4.2.3 Accretion rate . . . 63
4.2.4 Luminosity and temperature of the WD . . . 64
4.3 Results . . . 65
4.3.1 Column density of the CSM . . . 65
4.3.2 Line emission . . . 65
4.3.3 Line ratios . . . 70
4.4 Conclusions . . . 76

5 Conclusions 79

References 81

Acknowledgements 88

List of Figures

1.1 A schematic representation of a type Ia supernova lightcurve. 2
1.2 An example of a type Ia supernova spectrum. 3
1.3 Artist's representation of the two main progenitor channels. 4
1.4 A schematic representation of the Roche potential. 7
1.5 The stable burning regime on the $M - \dot{M}$ plane. 9
1.6 The ionized nebula around CAL 83. 11
1.7 A schematic picture of the WRLOF in symbiotic binaries. 14

2.1 All supernova remnants in Hα with WiFeS. 22
2.2 An example of the observed spectrum of the interstellar medium. 23
2.3 Surface brightness of He II 4686Å as a function of radius. 25
2.4 Upper limits on the luminosity as a function of temperature for each source. 27
2.5 Upper limits on the luminosity as a function of density. 28
2.6 Upper limits on the luminosity as a function of electron temperature. . . . 28
2.7 Comparison of upper limits on the luminosity as a function of temperature for SNR 0519-69.0. 29

3.1 The spectrum of LIN 358 as observed with WiFeS. 38
3.2 The observed line profiles of He II 4686Å, Hβ, Hα, and the Raman scattered O VI 6830 Å. 39
3.3 The Hα line profile with fitted components. 42
3.4 The geometrical configuration of the CLOUDY simulations. 44
3.5 The density distribution as seen by the WD. 45
3.6 Simulated [Fe X] 6374 Å luminosity as a function of temperature. 46
3.7 Simulated [Fe X] 6374 Å and He II 4686 Å luminosities as a function of the WD luminosity. 47
3.8 The observed and simulated line luminosities shown as a function of the mass-loss rate. 48
3.9 Structure of the emission region in the best-fitting simulation. 50
3.10 Distribution of line luminosity around the WD as a function of θ. 51
3.11 The emissivity of as a function of the distance from the ionising source. . . 51
3.12 The photospheric temperature and radius of the WD shown as a function of the mass-accretion rate. 53

3.13 The neutral hydrogen column density around the WD as a function of θ. . 55

4.1 The geometrical configuration of the CLOUDY simulations. 62
4.2 Temperature and luminosity of the white dwarf. 66
4.3 The neutral fraction of the CSM around the white dwarf. 67
4.4 The luminosity of four different emission lines. 68
4.5 Line luminosity as a function of the mass-loss rate for 3 AU. 69
4.6 Line luminosity as a function of the mass-loss rate for 14 AU. 70
4.7 The [O III] 5007/Hβ vs. [O III] 4363/Hγ line ratio diagram. 71
4.8 The line ratio diagrams of Kniazev et al. (2008). 72
4.9 The [Ne III] 3869/[O III] 4363 vs. [O III] 5007/[N II] 5755 line ratio diagram. 74
4.10 The He I line ratio diagram. 75

List of Tables

2.1 List of observed sources with relevant properties. 21
2.2 3σ upper limits on the He II 4686Å surface brightness for each source. . . . 25

3.1 List of the luminosities of the brightest observed emission lines. 39

Zusammenfassung

In dieser Dissertation untersuche ich die massenakkretierenden weißen Zwerge in binären Systemen, wie ihre Emission das zirkumstellare Material formt, was wir über diese Binärsysteme lernen können, indem wir die Emission des ionisierten Gases um sie herum beobachten und wie diese Systeme mit Supernovae vom Typ Ia verwandt sein können. Diese Supernovae, die das Ergebnis einer thermonuklearen Explosion des Weißen Zwergs sind, stehen seit Jahrzehnten im Mittelpunkt intensiver Forschung, da sie eine entscheidende Rolle bei der Messung von Entfernungen spielen und die beschleunigte Expansion des Universums beweisen. Trotzdem sind sie immer noch von vielen Fragen ohne Antwort umgeben. Eine der Hauptfragen ist, wie der Weg und die Anfangsbedingungen zu diesen Supernovae führen. Es ist allgemein anerkannt, dass die Supernova vom Typ Ia durch eine Explosion eines weißen Zwergs verursacht wird, aber es ist nicht bekannt, wie diese weißen Zwerge vom thermischen Gleichgewicht zum Massenwachstum, zur Zündung und zur Explosion gebracht werden.

Eine der Hauptkategorien möglicher Vorläufer ist der sogenannte einzelne entartete Vorläufer, bei dem ein weißer Zwerg in einem binären System mit einem anderen, nicht entarteten Begleiter, entweder einem Hauptreihenstern oder einem entwickelten Riesenstern, lebt. In diesem Szenario sammelt der Weiße Zwerg Material vom Begleiter an und explodiert schließlich nach Erreichen einer kritischen Masse. Damit der Weiße Zwerg die Masse effizient halten kann, muss das Material durch Kernfusion wieder aufbereitet werden. Dieser Prozess setzt große Mengen an Energie frei, was darauf hindeutet, dass diese massen-wachsenden weißen Zwerge in ionisierender Strahlung sehr leuchtend sind. Eine solche Emission würde die Umgebung aufgrund der langen Rekombinationszeit des interstellaren Gases nachhaltig prägen, und daher hat sich die Suche nach diesen Reliktnebeln als wirksames Instrument zur Einschränkung der Vorläuferkanäle erwiesen.

Bisher wurde jedoch nur ein solcher Nebel entdeckt, während die Theorie vorhersagt, dass die meisten, wenn nicht alle akkretierenden weißen Zwerge mit nuklearer Verbrennung von Wasserstoff auf ihrer Oberfläche einen haben sollten. Während der Hauptgrund eine geringe Helligkeit dieser Nebel zu sein scheint, die durch die geringe Gasdichte verursacht wird, wurden auch andere Gründe vorgeschlagen, wie beispielsweise die Verschleierung der Emission von weißen Zwergen durch zirkumstellares Material. In binären Systemen mit einem weiterentwickelten Riesenstern ist der Sternenwind sehr dicht und es wird angenommen, dass er sowohl die Emission des weißen Zwerges verdecken als auch die Umgebung beeinflussen kann. Diese als symbiotisch bekannten binären Systeme sind von einer komple-

xen zirkumstellaren Umgebung umgeben, deren Emissionsmechanismen vom infrarotemittierenden warmen Staub bis zum heißen weißen Zwerg reichen, der weiche Röntgenstrahlen emittiert. Diese symbiotischen Binärsysteme sind nicht nur interessante Kandidaten für Supernovae vom Typ Ia und die Bildung von Neutronensternen, sondern auch hervorragende Laboratorien für Sternentwicklung, binäre Interaktion und interagierende Winde.

In dieser Arbeit benutze ich das Fehlen ionisierter Nebel um vier Supernova-Überreste vom Typ Ia in der Großen Magellanschen Wolke, um den heißen und leuchtenden akkretierenden Vorläuferkanal der Weißen Zwerge einzuschränken. Die Nichterkennung dieser Nebel ermöglicht es mir, die Temperatur und Leuchtkraft des Vorläufers dieser Überreste streng zu beschränken, wodurch jegliche in jüngster Zeit akkretierende und nuklear brennende weißen Zwerge ausgeschlossen werden. Anschließend untersuche ich diese Binärsysteme der Weißen Zwerge im Detail und wie sich ihre Emission auf das umgebende Gas auswirkt und was wir über die Akkretionsprozesse im Binärsystem lernen können, indem ich die Emission des ionisierten Gases untersuche. Insbesondere konstruiere ich eine neue Methode, um das optische Spektrum zu modellieren, das aus dem zirkumstellaren Gas in symbiotischen Binärsystemen stammt mit 2D-Photoionisationssimulationen. Mit dieser Methode kann ich zusammen mit optisch-spektroskopischen Beobachtungen die Temperatur, Leuchtkraft und Massenakkretionsrate des Weißen Zwergs in dem symbiotischen binären System LIN 358 messen. Mit dieser Methode kann ich auch Vorhersagen für die beobachtbaren Größen wie Emissionslinienstärken dieser symbiotischen Binärsystemen liefern und zeigen, wie diese Observablen von den binären Systemparametern abhängen, wie z. B. der Orbitaltrennung und der Massenverlustrate vom Spenderstern. Darüber hinaus kann ich zeigen, dass insbesondere im wichtigsten Teil des Parameterraums für Supernova-Vorläufer vom Typ Ia die dichten Winde in symbiotischen Binärsystemen größtenteils ionisiert sind und die Emission des Weißen Zwergs, die dem System frei entweicht, nicht verdecken können.

Summary

In this dissertation I study the mass-accreting white dwarfs in binary systems, how their emission shapes the circumstellar material, what we can learn about these binaries by observing the emission from the ionized gas around them, and how these systems may be related to the Type Ia supernovae. These supernovae, which are the results of a thermonuclear explosion of the white dwarf, have been the focus of intense research for decades due to their critical role in measuring distances and proving the accelerated expansion of the Universe. Despite this, they are still surrounded by many questions without an answer. One of the major questions is, what is the path and initial conditions leading to these supernovae. It is generally accepted that a type Ia supernova is caused by an explosion of a white dwarf, but it is not known how these white dwarfs are pushed from thermal equilibrium to mass growth, ignition and explosion.

One of the main categories of possible progenitors is the so-called single degenerate progenitor, where a white dwarf resides in a binary system with an another, non-degenerate companion, either a main-sequence star or an evolved giant star. In this scenario the white dwarf accretes material from the companion and eventually explodes after reaching a critical mass. For the white dwarf to retain mass efficiently, the material needs to be reprocessed by nuclear fusion. This process releases large amounts of energy, suggesting that these mass-growing white dwarfs are very luminous in ionizing radiation. Such emission would leave a long-lasting imprint on the surroundings due to the long recombination time of the interstellar gas, and thus searching for these relic nebulae has been proven a powerful tool in constraining the progenitor channels.

However, only one such nebula has been detected to date, while theory predicts that most, if not all of the accreting white dwarfs with nuclear burning of hydrogen on their surface should have one. While the main reason seems to be a low brightness of these nebulae caused by the low gas density, other reasons have been suggested as well, such as obscuration of the white dwarf emission by circumstellar material. In binaries with an evolved giant star the stellar wind is very dense and thought to be able to both obscure the emission of the white dwarf and also affect the surroundings. These systems, known as symbiotic binaries, are surrounded by a complex circumstellar environment with emission mechanisms ranging from infrared-emitting warm dust to the hot white dwarf emitting soft X-rays. In addition to being interesting candidates for type Ia supernovae, and formation of neutron stars, these symbiotic binaries are excellent laboratories of stellar evolution, binary interaction, and interacting winds.

In this work, I use the lack of ionizing nebulae around four type Ia supernova remnants in the Large Magellanic Cloud to constrain the hot and luminous accreting white dwarf progenitor channel. The non-detection of said nebulae allows me to place stringent constraints on the temperature and luminosity of the progenitor of these remnants, ruling out any recent accreting and nuclear burning white dwarfs. I then continue to study these white dwarf binaries in detail and how their emission affects the surrounding gas, and what we can learn about the accretion processes in the binary by studying the emission from the ionized gas. Especially I construct a new method to model the optical spectrum originating from the circumstellar gas in symbiotic binaries with 2D photoionization simulations. Using this method together with optical spectroscopic observations I am able to measure the temperature, luminosity, and mass-accretion rate of the white dwarf in an symbiotic binary LIN 358. With this method I also provide predictions for the observables, such as emission line strengths, of these symbiotic binaries and show how these observables depend on the binary system parameters, such as orbital separation and mass-loss rate from the donor star. In addition, I am able to show that especially in the most important part of the parameter space for type Ia supernova progenitors, the dense winds in symbiotic binaries are mostly ionized and can not obscure the white dwarf emission, which escapes the system freely.

Chapter 1

Introduction

Low mass stars stars like the Sun spend most of their lifetime in the so-called main sequence burning hydrogen in their core. At the end of their life the stars' photosphere expands and forms a red giant, eventually blowing the outer layers away and forming a planetary nebula. Low and intermediate mass stars ($\lesssim 8$ $M_\odot$) leave behind a bound remnant known as a white dwarf. These white dwarfs have typically a mass of ~ 0.6 $M_\odot$ but a radius comparable to that of the Earth. The white dwarfs are typically composed of carbon and oxygen, but a higher mass white dwarfs can consists of oxygen, neon, and magnesium.

White dwarfs are held together by the degenerate electron pressure. White dwarfs are very compact and the electrons are pushed very close together. According to the Pauli Exclusion principle no two electrons can occupy identical states, but the electrons are forced out of the ground state and to the higher energy states. This creates a pressure that supports the white dwarf against the gravity. However, there is an upper limit to this pressure and so white dwarfs with masses above a critical limit of ~ 1.4 $M_\odot$, known as the Chandrasekhar mass, will collapse under their own gravity. This collapse will result in, depending on certain conditions, either a formation of a neutron star, or a runaway thermonuclear explosion known as Type Ia supernova.

1.1 Type Ia supernovae

Type Ia supernovae are defined as supernovae without hydrogen or helium lines in their spectra nearby their maximum luminosity (type I), in addition to exhibiting strong neutral and single ionized silicon lines (Filippenko 1997). This distinguishes them from type Ib and Ic supernovae, which together with the type II supernovae are nowadays understood to originate via the core-collapse mechanism, wherein the explosion is powered by the gravitational collapse of the iron core of massive stars (Woosley et al. 2002).

Type Ia supernovae, however, are thermonuclear explosions of carbon-oxygen white dwarfs (for a recent review see e.g. Wang 2018). During the explosion a large fraction of the carbon and oxygen fuses into heavier elements, up to iron and nickel. The typical explosion energy of $\sim 10^{51}$ ergs is enough to disrupt the whole star and distribute the

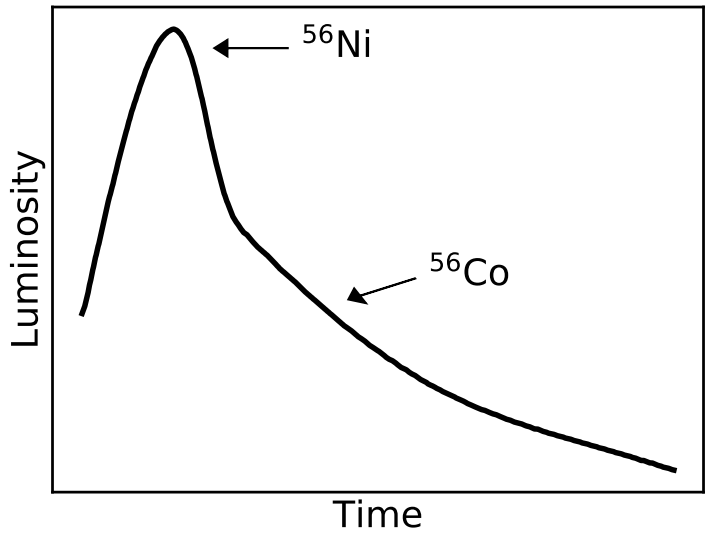

Figure 1.1: A schematic representation of a type Ia supernova lightcurve. The timescale for the peak, which is powered by the decay of ^{56}Ni, is a few tens of days, and the timescale for the cooling tail, which is powered by ^{56}Co, is a few hundred days.

material in the surrounding space. After the initial explosion the Type Ia supernovae are powered by the radioactive decay of the unstable nuclei produced during the explosion (Arnett 1982; Branch & Tammann 1992). The main isotope produced in the explosion is ^{56}Ni, which will decay to ^{56}Co with a half-life of 6.1 days, which in turn will decay to a stable isotope ^{56}Fe with a half-life of 77.3 days (see Fig. 1.1). During the months following the explosion the supernova will slowly fade when most of the radioactive material decays to stable isotopes. The shock wave produced in the explosion and the remnant of the supernova will continue to expand and be observable for thousands of years until finally mixing with the surrounding interstellar medium, enriching it with heavy elements (e.g. Matteucci & Greggio 1986).

Due to the radioactive nature of Type Ia supernova light curves, they can be used as standard candles to measure distances in the Universe. Not every supernova is equally bright, but there exists a relationship between the peak luminosity and the speed of the luminosity decay known as the Phillips relation (Phillips 1993; Phillips et al. 1999). According to this relationship, the brighter the supernova, the longer it takes for the luminosity to decay. This relation has been successfully used to measure distances in the Universe, measure the Hubble constant, and eventually to prove the accelerating expansion of the Universe (Riess et al. 1998; Perlmutter et al. 1999).

Despite their importance in enriching galaxies with heavy elements and measuring cosmic distances, the origin of Type Ia supernovae remains poorly understood beyond a simplified picture. It has been widely accepted that type Ia supernovae are the outcomes of thermonuclear explosions of carbon-oxygen white dwarfs with a mass close to the Chandrasekhar mass; this model explains well the observed light curves and spectroscopy

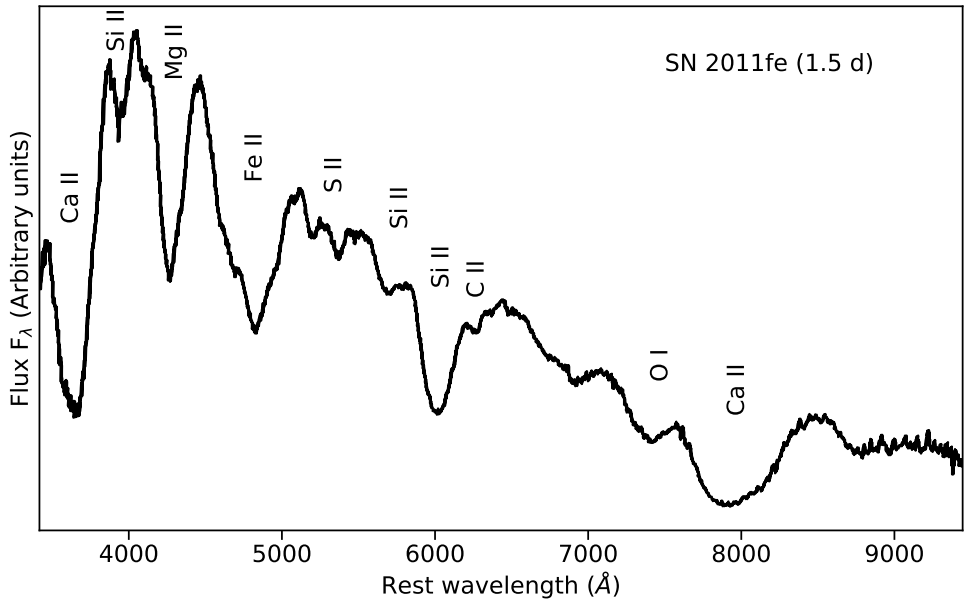

Figure 1.2: Optical spectrum of the type Ia supernova SN 2011fe taken 1.5 days after the explosion (Nugent et al. 2011). The main spectral features are shown above the spectrum.

of most SNe Ia (e.g. Nomoto 1984; Hoeflich et al. 1996; Podsiadlowski et al. 2008; Leung & Nomoto 2018). However, the Chandrasekhar limit for a non-rotating sphere composed of C and O is ≈ 1.4 $M_\odot$, but detailed stellar-evolutionary calculations of Umeda et al. (1999) suggest that the normal evolution of an isolated star may produce a carbon-oxygen white dwarf with a mass less than ≈ 1.1 $M_\odot$(see also Doherty et al. 2015, 2017). Thus, the conclusion is that WD needs to obtain enough mass from another companion star via some method prior to the explosion. The nature of such a companion star and the method of the mass transfer, in addition to the evolutionary pathways leading the WD from stable equilibrium to ignition and explosion, are still poorly understood after decades of research (Wang 2018).

1.1.1 Type Ia supernova progenitors

Various progenitor models have been proposed to explain how the white dwarfs reach the critical mass and to explain the observed diversity among SNe Ia. Most of these models may be broadly grouped into two categories (see Fig. 1.3). In the single degenerate scenario (Whelan & Iben 1973) a carbon-oxygen white dwarf accretes H/He-rich material from a main sequence or an evolved giant companion star, and grows through nuclear-burning of this material on its surface until reaching the Chandrasekhar mass and triggering an explosion. Alternatively, in the double degenerate scenario (Webbink 1984; Iben & Tutukov 1984) two carbon-oxygen white dwarfs orbiting each other eventually merge together due to shedding of angular momentum through gravitational wave radiation.

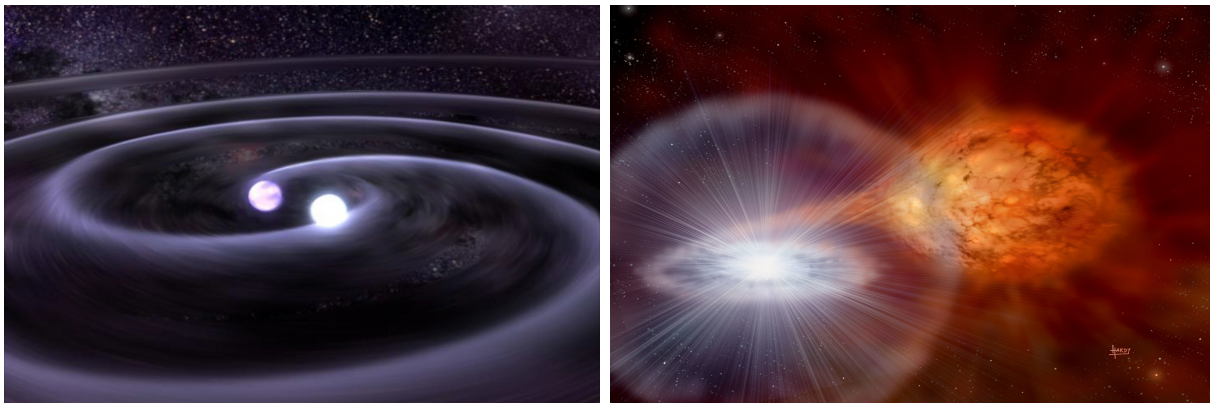

Figure 1.3: Artist's representation of the two main progenitor channels. On the left is the double degenerate channel, where a white dwarf binary is losing angular momentum through gravitational radiation and eventually merging. On the right is the single degenerate scenario, where a white dwarf accretes H/He-rich material from a non-degenerate companion star. Image credits: Tod Strohmayer (GSFC)/Dana Berry (CXC), David A. Hardy & PPARC.

Historically, the single degenerate scenario was favoured for many years. The merger of two white dwarfs had been thought to almost always lead to an accretion-induced collapse before the conditions necessary for an explosion were reached during the merger (Saio & Nomoto 1985, 1998; Nomoto & Iben 1985). The high accretion rate during the merger may cause an off-centre carbon ignition, which propagates inwards converting the carbon-oxygen white dwarf to an oxygen-neon white dwarf. Such a white dwarf will collapse into a neutron star rather than explode as type Ia supernova. However, recent development has found that the collapse can be avoided in a violent merger scenario and that the explosion of the white dwarf merger remnant is feasible (Pakmor et al. 2010, 2011, 2012).

Meanwhile, the single degenerate channel is facing an increasing amount of observational evidence against it. On one hand, the donor star in this scenario will survive the explosion and it should be identifiable from other nearby stars due to e.g. its anomalous velocity, composition, rotation, temperature, or luminosity (Marietta et al. 2000; Canal et al. 2001; Liu et al. 2013; Pan et al. 2013; Shappee et al. 2013). Numerous studies have searched for these surviving companions, but no such star has been found (e.g. Rest et al. 2008; Badenes et al. 2008; Schaefer & Pagnotta 2012; Edwards et al. 2012; Olling et al. 2015). On the other hand, there is no pre-explosion evidence for a single degenerate progenitor. Various studies of pre-explosion images of the explosion sites have placed stringent constrains on the progenitors (e.g. Li et al. 2011; Nielsen et al. 2012; Graur et al. 2014; Graur & Woods 2019).

In addition to direct imaging, the single degenerate channel has been constrained with various other observational arguments. In the canonical picture the white dwarf is accreting material from the companion and the accreted hydrogen is processed through nuclear burning on the surface of the white dwarf, which produces luminosities of $\sim 10^{38}$ erg s^{-1}

(van den Heuvel et al. 1992). Any viable single degenerate channel predicts a large number of accreting and nuclear burning white dwarfs which would significantly affect the total emission of a galaxy. However, the existence of such large populations of ionizing white dwarfs has been constrained by observations (Gilfanov & Bogdán 2010; Woods & Gilfanov 2013; Johansson et al. 2014; Woods & Gilfanov 2016). However, despite these problems the single degenerate scenario remains a plausible progenitor channel for type Ia supernovae, especially for the more peculiar events.

1.2 Accreting white dwarfs

For a white dwarf (WD) to grow in mass, it must accrete and retain matter from a companion star. This accretion can emit large amounts radiation due to the release of the gravitational potential energy of the infalling matter. If all of this energy is released as radiation at the stellar surface, the accretion luminosity is

$$L_{\rm acc} = \frac{GM\dot{M}}{R_*}, \tag{1.1}$$

where $\dot{M}$ is the mass-accretion rate, and M and R_* are the mass and radius of the accretor, which in this case is the white dwarf. In reality, only half of this luminosity is radiated at the WD surface and the other half is radiated by an accretion disk.

In most cases of accretion in binary systems, the transferred material cannot land on the accreting star until it has rid itself of most of its angular momentum. The material will settle on an orbit around the accreting star, creating an accretion disk, and later spiral inwards due to loss of angular momentum via viscous torques. These torques will also heat up the material in the disk, which will then emit thermal radiation. For a standard optically thick accretion disk, the temperature structure is given by (e.g. Shakura & Sunyaev 1973; Frank et al. 2002)

$$T(R) = \left\{ \frac{3GM\dot{M}}{8\pi R^3 \sigma_{\rm SB}} \left[1 - \left(\frac{R_*}{R} \right)^{1/2} \right] \right\}^{1/4}, \tag{1.2}$$

where $\sigma_{\rm SB}$ is the Stefan-Boltzmann constant and R is the radial distance from the star. The disk reaches the maximum temperature $T_{\rm max} = 0.488\, T_*$, where

$$T_* = \left(\frac{3GM_*\dot{M}}{8\pi R_*^3 \sigma_{\rm SB}} \right)^{1/4}, \tag{1.3}$$

at a radius $R = \frac{49}{36} R_*$. The accretion disk will emit roughly half of the accretion luminosity as thermal radiation with multi-temperature blackbody spectrum.

The other half of the accretion luminosity is released by a boundary layer near the surface of the WD. The angular velocity of the infalling matter in the disk remains close to the Keplerian value

$$\Omega_{\rm K}(R) = \left(\frac{GM}{R^3} \right)^{1/2}, \tag{1.4}$$

which means that the gas must slow down to the stellar rotation velocity Ω_* near the surface in the boundary layer. Thus the excess kinetic energy radiated from the boundary layer has a form of

$$L_{BL} = \frac{GM\dot{M}}{2R_*}\left(1 - \frac{\Omega_*}{\Omega_K}\right)^2, \tag{1.5}$$

which reduces to $\frac{1}{2}L_{\rm acc}$ for $\Omega_* \ll \Omega_K$.

The spectrum of the boundary layer can be quite complicated and depends on many factors. However, if the accretion rate, and thus density, is high enough that the boundary layer becomes optically thick, the spectrum can be well approximated with a blackbody radiation. In this case, the colour temperature of the boundary layer is

$$T_{\rm BL} = T_*\left(\frac{3GM_*\mu m_{\rm H}}{8kR_*T_*}\right)^{1/8}, \tag{1.6}$$

where μ is the mean molecular weight, $m_{\rm H}$ is the mass of hydrogen, and k is the Boltzmann constant. For white dwarfs, the accretion rate limit is $\sim 10^{16}$ g s^{-1} (Pringle & Savonije 1979; Popham & Narayan 1995), below which the the boundary layer is optically thin with temperatures of up to 10^8 K and a complicated spectrum (Pringle 1977; Popham & Narayan 1995; Suleimanov et al. 2014). For higher accretion rates the boundary layer is optically thick with typical temperatures of 10^{5-6} K. This simple picture is in agreement with the theoretical BL simulations of e.g. Hertfelder et al. (2013); Suleimanov et al. (2014).

This transfer of matter from one star to the other in binaries, happens usually in one of the two main ways: stellar wind accretion or Roche lobe overflow. In the former case, the donor star of the binary will at some point of its evolution eject some fraction of its mass in the form of a stellar wind. A part of this material will then be captured gravitationally by the white dwarf and accreted onto its surface. The stellar wind accretion is often described with the Bondi-Hoyle-Lyttleton formalism (Hoyle & Lyttleton 1939; Bondi & Hoyle 1944). The wind accretion is often quite unefficient and only a small fraction of the matter ejected as a wind will be accreted by the white dwarf, thus leading to faint emission and negligible mass growth. For this reason, the more efficient Roche lobe overflow is the more interesting case, when considering type Ia supernova progenitors.

In the Roche lobe overflow the accreted matter is stripped from the outer layers of donor star by the gravitational pull of the white dwarf. This form of matter transfer can happen only in close binaries, and it is often initiated when either the binary orbit shrinks due to loss of angular momentum via e.g. gravitational radiation, or the companion star expands and fills its Roche lobe during its evolution off the main-sequence. This so-called Roche lobe is the region around each star, inside which the material is bound to that star. Following the motion of a massless test particle in the gravitational field of the two stars with masses M_1 and M_2, one can calculate the effective potential in a co-rotating frame by:

$$\Phi(\vec{r}) = -\frac{GM_1}{|\vec{r} - \vec{r_1}|} - \frac{GM_2}{|\vec{r} - \vec{r_2}|} - \frac{1}{2}(\vec{\omega} \times \vec{r})^2. \tag{1.7}$$

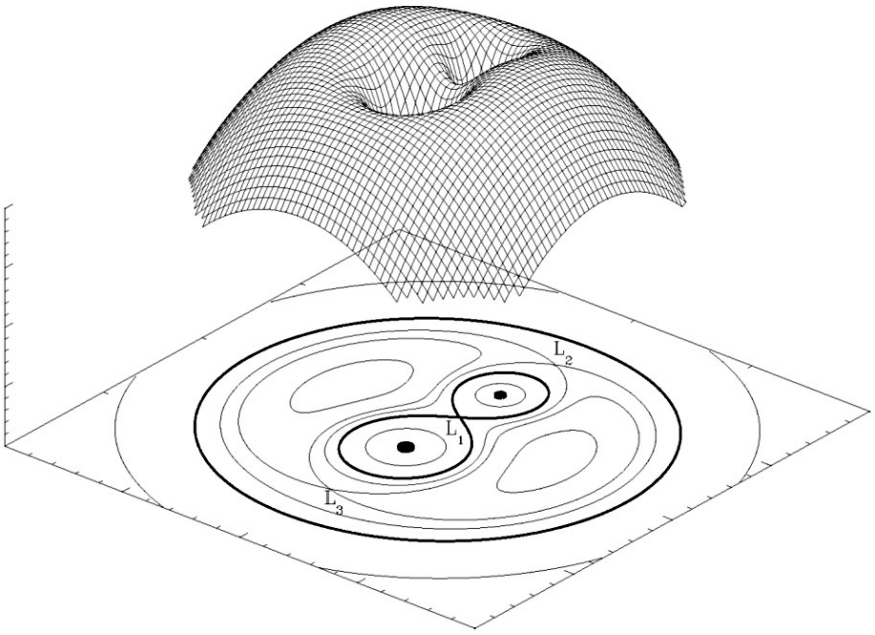

Figure 1.4: The Roche potential for a binary system with a mass ratio of 2, in the co-rotating frame. The droplet-shaped figures in the equipotential plot at the bottom show the Roche lobes of the stars. L1, L2, and L3 show the locations of three Lagrangian points. Image credit: Marc van der Sluys.

In this equation the first and second term consider the gravitational pull of each star, and the last term describes the centrifugal force to the rotation of the binary. This Roche potential is illustrated in Fig. 1.4, where both a 3D surface representing the Roche potential and a section in the orbital plane are shown with the equipotential surfaces of $\Phi(\vec{r})$. The most interesting parts of this figure are the places where the equipotential surfaces cross, i.e. the points where the gravitational pulls of each stars are equal:

$$\nabla\Phi(\vec{r}) = 0. \tag{1.8}$$

These five points are known as Lagrangian points and they are of great importance to many topics in orbital mechanics. The inner Lagrangian point L_1 is a saddle point located between the two stars. The Roche lobe of each star can be defined as the surface surrounding the star with the potential equal to that of the L_1 point. This point is also of particular interest, because it connects the gravitational spheres of influence of the two stars. This means that, if one star expands and fills its Roche lobe, the matter can flow through the L_1 point into the Roche lobe of the other star (see e.g. Paczyński 1971; Podsiadlowski et al. 2002; Leahy & Leahy 2015).

The shape of the Roche lobe is quite complicated and non-spherical, but the size is often estimated as the radius of a sphere with the same volume. Due to the complicated form of

Eq. (1.7), approximate analytical formulas are typically used to calculate this radius. The equation

$$R_{L,1} = a \times \frac{0.49q^{2/3}}{0.6q^{2/3} + \ln(1 + q^{1/3})}, \tag{1.9}$$

where a is the orbital separation of the two stars and $q = M_1/M_2$ is the mass ratio, presented by Eggleton (1983) gives a good fit across the whole range of mass ratios.

1.2.1 Nuclear burning white dwarfs

The simple estimates for the luminosity and temperature of an accreting white dwarf presented above hold quite well for many observed systems. At high accretion rates, however, these predictions fall short of the observations. The luminosities of the white dwarfs in systems with high accretion rate are of the order of 10^{37-38} erg s^{-1}, which is an order of magnitude higher than predicted by Eq. (1.1). In these systems the luminosity is sustained by nuclear fusion of hydrogen into helium on the surface of the white dwarf. The energy released in this nuclear burning is

$$\Delta E_{\rm nuc} = 0.007\, m\, c^2. \tag{1.10}$$

Comparing this to Eq. (1.1), one can see that for a typical white dwarf the energy release from nuclear burning is more efficient than the accretion by a factor of ~ 30.

The exact appearance of a nuclear burning white dwarf depends heavily on the accretion rate. While the luminosity of a steadily nuclear burning white dwarf is

$$L = \epsilon\, \chi\, \dot{M} \tag{1.11}$$

for a given accretion rate, where $\epsilon \approx 6.4 \times 10^{18}$ erg g^{-1} is the energy released from a nuclear burning (cf. Eq. 1.10) and χ if the hydrogen fraction of the accreted material (≈ 0.72 for solar composition), such a steady nuclear burning is possible only in a narrow range of accretion rates (Shen & Bildsten 2007; Wolf et al. 2013). For a 1 M$_\odot$ white dwarf the hydrogen burning is stable and occurs at the same rate as the accretion only for accretion rates of $\sim (2-4) \times 10^{-7}$ M$_\odot$ year^{-1}, as shown in Fig. 1.5. Within this range, any increase in the temperature of the nuclear burning layer causes the cooling rate to increase faster than the nuclear burning rate and thus any perturbation is damped out (Shen & Bildsten 2007).

For higher mass accretion rates, the hydrogen will continue to burn steadily, but the nuclear burning rate is limited, which causes the excess matter to pile up on the white dwarf. This causes the WD photosphere to expand and to transition to a more red-giant-like structure, while the luminosity of the WD stays roughly constant and the effective temperature decreases.

At lower accretion rates than the limit for stable nuclear burning the white dwarf will experience nova outbursts. The accreted matter will accumulate on the surface of the white dwarf until a certain envelope mass is reached and the nuclear burning is triggered.

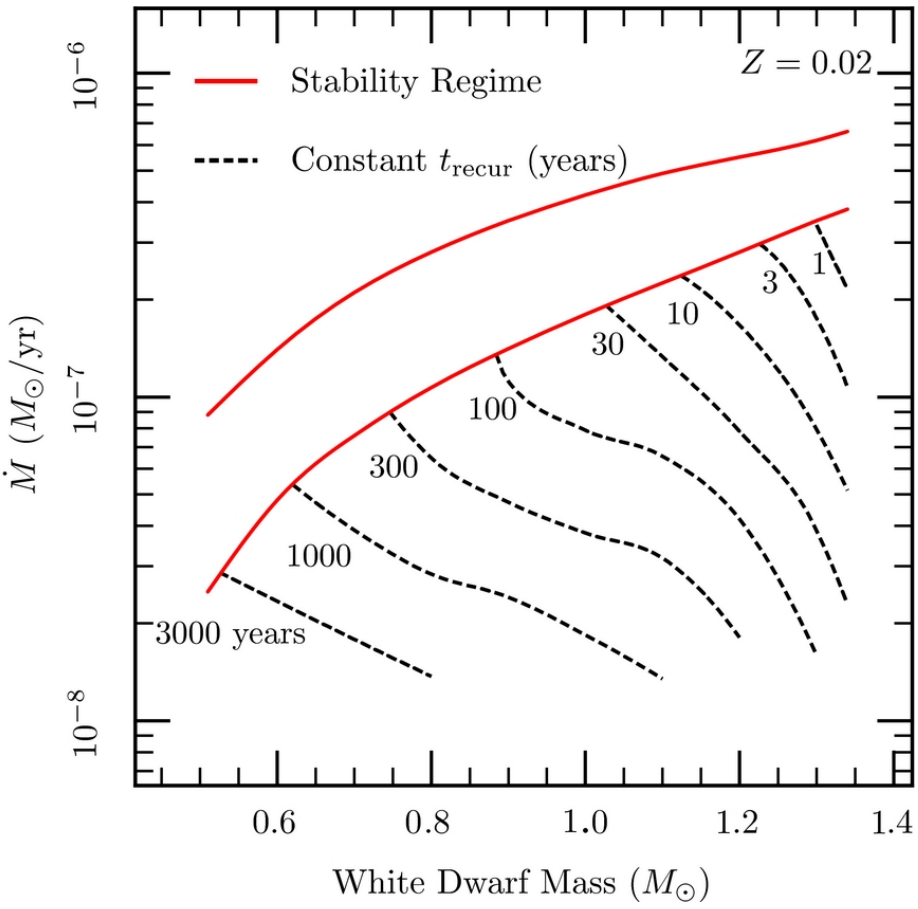

Figure 1.5: The location of the stable-burning regime as a function of the WD mass and accretion rate. The lower red line illustrates the lower boundary for stable nuclear burning, and the upper red line shows the maximal steady accretion rate. Below the stability regime the dashed lines show the regions for recurrent novae with the recurrence times shown in years. The figure is from Wolf et al. (2013).

However, at these lower accretion rates the burning is unstable, contrary to the stable burning regime. Any temperature perturbation causes the nuclear heating rate to increase faster than the cooling rate, which causes a runaway thermonuclear reaction, which burns all the available fuel. These novae recur after certain intervals depending on the accretion rate and the mass of the WD "recurrent novae", but the timescale can be too long measure on human timescales "classical novae" (Yaron et al. 2005; Wolf et al. 2013).

The steadily nuclear burning white dwarfs are the most interesting ones in the context of type Ia supernovae, because in this regime the WD can retain most of the accreted matter and thus grow efficiently in mass. In lower accretion rates only a fraction of the accreted matter is retained and most of the mass is ejected in the nova outbursts. This has some important implications on the population of type Ia supernova progenitors. As mentioned above, the nuclear burning releases a lot of energy, and these nuclear burning white dwarfs are very bight in extreme ultraviolet and soft X-rays, with luminosities of 10^{37-38} erg s^{-1} and temperatures of 10^{5-6} K. Thus these white dwarfs emit large amounts of ionizing radiation, which affects their surrounding ISM and can be observed. This will create an ionized nebula around such a white dwarf, known as the Strömgren sphere (Strömgren 1939). An example of such a ionized nebula around an accreting and nuclear burning white dwarf CAL 83 is shown in Fig. 1.6.

For such an ionized nebula in an ionization equilibrium the rate of photoionisations is balanced by the rate of recombinations at any point in the nebula. For pure hydrogen, the ionization equilibrium equation is (see e.g. Osterbrock & Ferland 2006):

$$n_{\mathrm{H}} \int_{\nu_0}^{\infty} \frac{4\pi J_\nu}{h\nu}\, a_\nu(\mathrm{H}^0)\, d\nu = n_e\, n_p\, \alpha(\mathrm{H}^0, T), \tag{1.12}$$

where J_ν is the mean intensity of radiation (in erg cm^{-2} s^{-1} steradian^{-1} Hz^{-1}), $a_\nu(\mathrm{H}^0)$ is the ionization cross section of hydrogen, $\alpha(\mathrm{H}^0, T)$ is the recombination coefficient, and n_{H}, n_e, and n_p denote the number densities of hydrogen, electrons, and protons, respectively. With various approximations, e.g. spherically symmetric nebula containing only hydrogen and case B recombination, one can use this description to get a picture of a nearly completely ionized nebula, "Strömgren sphere", separated by a thin transition region from an outer neutral gas cloud. The radius of the ionized region, called the Strömgren radius, can be calculated as:

$$R_S = \left(\frac{3\dot{N}_{\mathrm{ph}}}{4\pi n^2 \alpha_B}\right)^{1/3} \approx 35 \text{ pc} \left(\frac{\dot{N}_{\mathrm{ph}}}{10^{48} \text{ s}^{-1}}\right)^{1/3} \left(\frac{n_{\mathrm{ISM}}}{1 \text{ cm}^{-3}}\right)^{-2/3}, \tag{1.13}$$

where $\dot{N}_{\mathrm{ph}}$ is the number of ionizing photons and α_B is the case B recombination coefficient (Strömgren 1939; Osterbrock & Ferland 2006). In reality, however, the situation is usually more complex and the interstellar medium consists of also other elements than just hydrogen. Numerical methods, such as the photoionization and spectral synthesis code CLOUDY (Ferland et al. 2017), are often used to get a more accurate picture of the real situation.

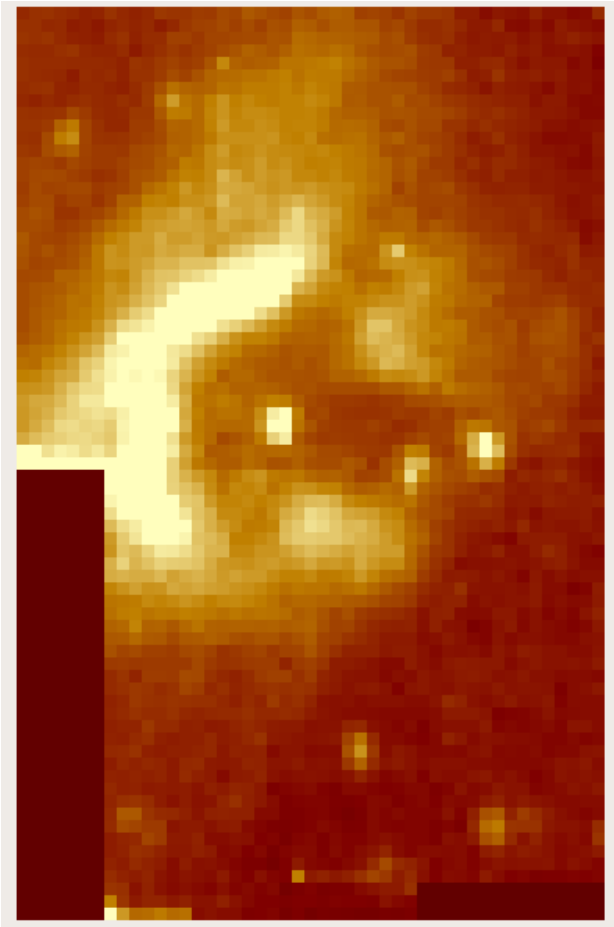

Figure 1.6: The ionized nebula around the accreting and nuclear burning white dwarf CAL 83 observed with the wide-field imaging spectrograph (WiFeS) mounted on the 2.3m ANU telescope in Siding Spring Observatory, Australia (observation ID: 4180034, PI: I. Seitenzahl).

These ionized nebulae can be used to constrain the possible type Ia supernova progenitors. The typical hydrogen recombination time in the interstellar medium is

$$\tau_{rec} = \left(n_e \alpha_B(H^0, T)\right)^{-1} \approx 10^5 \times \left(\frac{n_{\rm ISM}}{1{\rm cm}^{-3}}\right)^{-1} {\rm years}, \tag{1.14}$$

which means that an ionized nebula created by an accreting and nuclear burning white, i.e. the prime single degenerate progenitor candidate, should be visible for $\sim 10^5$ years after the ionizing source has been switched off. These nebulae are mostly unaffected by the supernova explosion, and thus searching for these relic nebula can be used to constrain the progenitor scenarios of type Ia supernovae (Bisnovatyi-Kogan 1972; Woods & Gilfanov 2016; Woods et al. 2017; Kuuttila et al. 2019).

1.2.2 Symbiotic binaries

Symbiotic binaries, also known as symbiotic stars, are white dwarfs (or sometimes neutron stars) accreting from a red giant companion star. These binaries can have very long orbital periods, up to tens of years (e.g. 43.6 years for R Aqr; Gromadzki & Mikołajewska 2009), but despite this the white dwarf is often accreting efficiently from the wind of the donor star. Symbiotic binaries are often classified into two main categories based on their infrared emission. In the S-type binaries the infrared emission is dominated by the continuum radiation of the cool giant star, whereas in the D-type binaries (e.g. Mira type variables) the infrared emission is dominated by the warm dust in the wind of the donor star. S-type binaries have typically shorter periods, from 1 to 6 years, while the dust dominated D-type binaries have even longer periods (Gromadzki et al. 2013).

The presence of both a cool and a hot component in the binary means that the spectra of symbiotic binaries can be quite complex: the same star may exhibit features both typical to the coolest M giants, like the TiO bands, and emission lines from highly excited ions, for example He II, O VI, and Fe X. The symbiotic binaries are surrounded by a complex circumstellar medium, which is the result of the interaction of the dense neutral wind from the donor star, orbital mechanics, ionizing emission from the WD, and possible high-velocity ionized winds and even jets from the WD. This all means that symbiotic binaries are excellent laboratories for binary interaction and evolution due to the phenomena such as jets, accretion disks, and colliding winds. In addition, symbiotic binaries exhibit all the other common characteristics of accreting and nuclear burning white dwarfs, such as nova outbursts, as outlined in the previous chapter (Mikołajewska 2012; Munari 2019).

Symbiotic binaries have often very wide orbital separations, which makes the typical Roche lobe overflow accretion scenario, where the donor star expands and fills its Roche lobe allowing the matter to flow to the white dwarf via the L1 point, impossible. In addition, interaction via the Roche lobe overflow with an AGB star with a deep convective envelope may often lead to unstable mass transfer (Hjellming & Webbink 1987; Chen & Han 2008, though see e.g., Woods & Ivanova 2011) and a common envelope phase, which will decrease the size of the orbit (Paczynski 1976).

AGB stars are known to have strong stellar winds with mass-loss rates on the order of $10^{-8} - 10^{-5}$ $M_\odot$ yr^{-1} and low velocities on the order of $5 - 30$ km s^{-1} (Höfner & Olofsson 2018). Therefore, it is commonly assumed that, instead of the Roche lobe overflow, the WD is accreting material from the wind of the donor star. However, the standard Bondi-Hoyle-Lyttleton (BHL; Hoyle & Lyttleton 1939; Bondi & Hoyle 1944) wind accretion scenario often fails to explain the required mass accretion rates. The typical accretion efficiencies of the BHL scenario are only a few per cent, and to explain the observed luminosities in many symbiotic binaries, accretion rates on the order of $10^{-7} - 10^{-6}$ $M_\odot$ yr^{-1} are required. The BHL description is often a good approximation of the wind accretion when the outflow velocity is fast compared to the orbital velocity, which is not the case for typical AGB winds, which are slow ($5 - 30$ km s^{-1}) and comparable to the orbital velocities of symbiotic binaries.

To solve the problem of wind accretion in symbiotic binaries, many detailed simulations have been carried out (e.g. Mohamed & Podsiadlowski 2007; de Val-Borro et al. 2009; Mohamed & Podsiadlowski 2012; Abate et al. 2013; de Val-Borro et al. 2017; Abate et al. 2018; Saladino et al. 2018, 2019). These simulations suggest a new mode of mass transfer, that lies somewhere in between the Roche lobe overflow and the BHL wind accretion. In this mode, often called wind Roche lobe overflow (WRLOF), the star itself does not fill the Roche lobe, but the slow wind slowly fills the Roche lobe and eventually flows through the L1 point to the white dwarf. The mass accretion efficiency of this method can reach up to 50 per cent of the mass-loss rate of the donor star, which is much higher than the BHL efficiency.

The WRLOF can occur only in binaries where the wind is slow and gravitationally confined to the Roche lobe of the donor star. The initial velocity of the wind is not sufficient to escape spherically from gravitational pull of the donor star so the wind can efficiently fill up the Roche lobe. The exact mechanism that drives this wind the AGB stars is not yet fully known. In the generally accepted model the outflow happens in two stages (Höfner 2015; Höfner & Olofsson 2018): in the first stage stellar pulsations cause shock waves, which push the gas from the stellar photosphere outwards up to a few stellar radii. At these distances the temperature ($\lesssim 1500$ K) is low enough for the dust grains to condensate. These dust grains are then accelerated by the radiation pressure, dragging the surrounding gas along due to the collisional momentum transfer (Höfner 2007). Therefore the wind acceleration radius coincides with the dust formation, which depends on the temperature of the donor star and the chemical composition.

The conditions necessary for the WRLOF are often estimated with the ratio of the Roche lobe size of the donor to the wind acceleration radius, $R_d/R_{L,1}$. According to the hydrodynamical simulations, the maximum efficiency is reached with $R_d/R_{L,1} \approx 1.5$. The WRLOF scenario is illustrated in Fig.1.7.

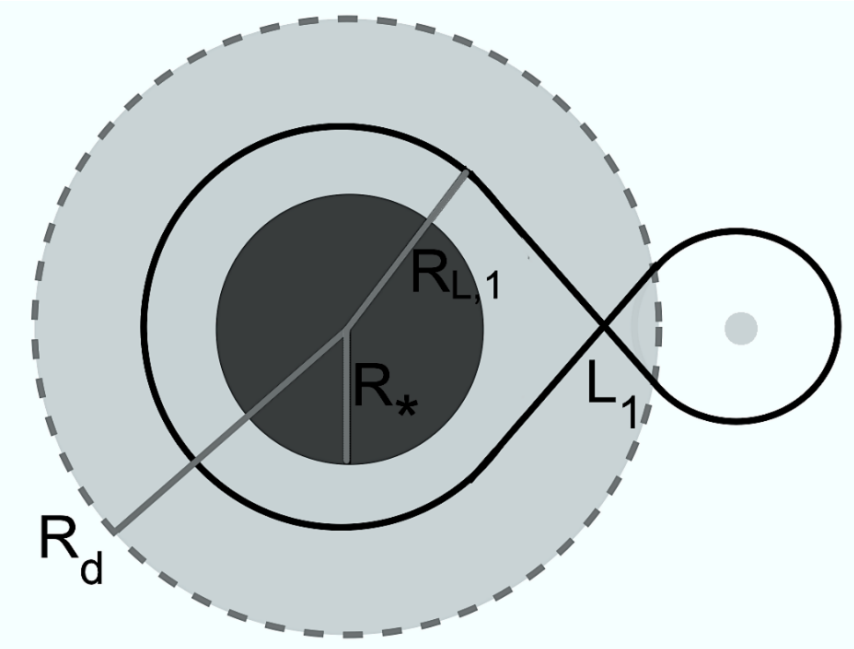

Figure 1.7: A schematic picture of the WRLOF conditions. R_d is the wind acceleration radius, i.e. the dust formation radius, $R_{L,1}$ is the Roche lobe size of the donor star, and R_* represents the radius of the donor star (sizes are not to scale). The figure is adapted from Abate et al. (2013).

1.3 This thesis

After decades of research, there are still many unknowns related to the type Ia supernova progenitors and the contribution to their explosion rate from the accreting white dwarfs. In addition, the observational appearance of these progenitor systems remains unclear in many situations. In this thesis I study these objects and aim to shed some new light on their nature and explore their observational appearance.

In Chapter 2 we study four different young type Ia supernova remnants located in the Large Magellanic Cloud and observed with the wide-field imaging spectrograph WiFeS on the 2.3m ANU telescope in Siding Spring Observatory (observation IDs: 4140118 and 4150145, PI: I. Seitenzahl). We studied these remnants in order to detect relic ionized nebulae around them. A detection of such a nebula would provide direct proof of a single degenerate progenitor for these supernovae. We focus especially on the He II 4686 Å emission line, which is a clear signature of an accreting and nuclear burning white dwarf. We do not detect a nebula around any of these supernova remnants and thus, using photoionization simulations, place stringent upper limits on the temperature and luminosity of the progenitors of these supernova remnants. This work has been published in Kuuttila et al. (2019).

In Chapter 3 we turn to study the accreting and nuclear burning white dwarfs and how they shape their surroundings. We especially focus on a steadily accreting and nuclear burning symbiotic binary LIN 358. We observed this source with optical spectrograph WiFeS, and together with our newly developed method to use the photoionization code CLOUDY to perform 2D radiative transfer simulations, we measured the temperature and luminosity of the white dwarf, and the main system parameters such as the wind mass-loss rate from the donor star. In addition, we showed how the white dwarf is capable of ionizing the majority of the donor star wind despite the high mass-loss rate. This work has been published in Kuuttila et al. (2021).

In Chapter 4 we expand the results of the previous chapter and using our 2D photoionization simulations method we present a grid of simulations showing how the binary properties, such as the wind mass loss rate and the orbital separation, affect the observables of symbiotic binaries. In particular we show how these parameters affect the optical emission line luminosities and the emission line ratios, which are often used to separate symbiotic binaries from e.g. planetary nebulae. In addition, we present simulations showing how the wind is ionized in these binaries and how the local column depth affects the observability of these systems. This work will be submitted for publication after the submission of this thesis.

Chapter 2

Excluding super-soft X-ray sources as progenitors for four Type Ia supernovae in the Large Magellanic Cloud

The contents of this chapter have been published in Kuuttila et al. (2019) Monthly Notices of Royal Astronomical Society, 484, 1317

Abstract Type Ia supernovae are vital to our understanding of the Universe due to their use in measuring cosmological distances and their significance in enriching the interstellar medium with heavy elements. They are understood to be the thermonuclear explosions of white dwarfs, but the exact mechanism(s) leading to these explosions remains unclear. The two competing models are the single degenerate scenario, wherein a white dwarf accretes material from a companion star and explodes when it reaches the Chandrasekhar limit, and the double degenerate scenario, wherein the explosion results from a merger of two white dwarfs. Here we report results which rule out hot, luminous progenitors consistent with the single degenerate scenario for four young Type Ia supernova remnants in the Large Magellanic Cloud. Using the integral field spectrograph WiFeS, we have searched these remnants for relic nebulae ionized by the progenitor, which would persist for up to $\sim 10^5$ years after the explosion. We detected no such nebula around any of the remnants. By comparing our upper limits with photoionization simulations performed using Cloudy, we have placed stringent upper limits on the luminosities of the progenitors of these supernova remnants. Our results add to the growing evidence disfavouring the single degenerate scenario.

2.1 Introduction

Type Ia supernovae (SNe Ia) are runaway thermonuclear explosions of carbon-oxygen white dwarfs (CO WDs) (see e.g. Hillebrandt et al. 2013; Maoz et al. 2014, for reviews). SNe Ia can be used for distance measurements on cosmic scales due to a correlation between their peak luminosity, the rate of decline after maximum light, and the colour at maximum. This so-called Phillips relation (Phillips 1993; Phillips et al. 1999) has been used to show the acceleration of the Universe's expansion (Riess et al. 1998; Perlmutter et al. 1999). SNe Ia are also important to the chemical evolution of galaxies, since a typical SN Ia enriches the interstellar medium (ISM) with $\sim$0.7 $M_\odot$ of iron and a similar amount of other elements (Matteucci & Greggio 1986; Wiersma et al. 2011).

Despite their significance to our understanding of the Universe, the formation channel for SNe Ia is still uncertain. The two leading models are the single degenerate (SD) scenario, in which a single WD reaches the critical carbon ignition density through accretion from either a main-sequence or an evolved companion star (Whelan & Iben 1973); and the double degenerate scenario, in which the explosion results from the merger of a binary pair of WDs (Iben & Tutukov 1984).

In the double degenerate scenario, the progenitor system is typically too faint to be detectable with current instruments prior to the explosion. In the single degenerate scenario, however, progenitor systems should be detectable both before and, most importantly, after the explosion. In particular, if steady nuclear burning of hydrogen occurs on the surface of a WD, as expected from the single degenerate channel, then in the most efficient regime for mass accumulation the accreting WD should reveal itself as a strong super-soft X-ray source (SSS) (van den Heuvel et al. 1992; Kahabka & van den Heuvel 1997).

The first of these SSSs were discovered in the Large Magellanic Cloud (LMC) using the Einstein Observatory (HEAO-2, Long et al. 1981). SSSs are typically luminous ($L_{\rm bol} \gtrsim 10^{37-38}$ erg s^{-1}) and characterized by effective temperatures of $T_{\rm eff} \sim 10^6$ K (Greiner 2000). Due to their high temperatures and luminosities, SSSs emit significant fluxes of UV and soft X-ray photons, which will strongly ionize any surrounding interstellar gas. This in turn will create a characteristic ionization nebula with a typical ("Strömgren") radius of

$$\mathrm{R_S} = \left(\frac{3}{4\pi} \frac{\dot{\mathrm{N}}_{\rm ph}}{\mathrm{n}_{\rm ISM}^2 \alpha} \right)^{\frac{1}{3}} \approx 35\mathrm{pc} \left(\frac{\dot{\mathrm{N}}_{\rm ph}}{10^{48}\,\mathrm{s}^{-1}} \right)^{\frac{1}{3}} \left(\frac{\mathrm{n}_{\rm ISM}}{1\,\mathrm{cm}^{-3}} \right)^{-\frac{2}{3}}, \tag{2.1}$$

where α is the recombination coefficient, $\dot{\mathrm{N}}_{\rm ph}$ is the number of ionizing photons per second, and $\mathrm{n_{ISM}}$ is the number density of the ISM (Rappaport et al. 1994; Woods & Gilfanov 2016). In addition to the direct emission from the central SSS, significant ionization nebulae can be also produced by the emission from the accretion disc when the accretion rate is too low for the hydrogen fusion to be ignited (Woods et al. 2017).

To date, only one such emission-line nebula has been detected, surrounding a SSS in the LMC known as CAL 83 (Remillard et al. 1995). These authors, in fact, conducted also imaging observations of nine other known SSSs in the LMC and SMC, but did not detect nebulae around them. Later, Gruyters et al. (2012) observed a part of the nebula

around CAL 83 using the VLT/VIMOS and detected for the first time also the He II 4686Å emission line. The high ionization potential of He II (54.4 eV) requires a hot ($\gtrsim 10^5$ K) ionizing source, making the He II emission an easily recognizable signal of an accreting WD with steady nuclear burning on its surface. Models for SSS nebulae indeed predict that these nebulae should be bright in He II 4686Å and [O III] 5007Å , making them distinct from other astrophysical nebulae (Rappaport et al. 1994; Woods & Gilfanov 2016). For this reason, the He II 4686Å emission line has been used to constrain the suitability of SSSs as progenitors for SNe Ia, either by examining pre-explosion archival observations of the explosion site (Graur et al. 2014), or by comparing the observed total He II emission of galaxies to the expected emission from population synthesis models (Woods & Gilfanov 2013; Johansson et al. 2014).

If a single degenerate SN Ia progenitor spends a significant amount of time as a SSS prior to the explosion, then the ionized nebula should remain detectable after the WD is destroyed in the explosion, until the majority of the ionized gas has recombined. If the gas in the nebula is initially fully ionized (i.e. $n_e \approx n_{\rm ISM}$), the typical hydrogen recombination time can be estimated as

$$\tau_{rec} = \left(n_e \alpha_B(H^0, T \approx 10^4 K)\right)^{-1} \approx 10^5 \times \left(\frac{n_{\rm ISM}}{1{\rm cm}^{-3}}\right)^{-1} {\rm years}, \tag{2.2}$$

where $\alpha_B(H^0, T)$ is the Case B recombination coefficient (Woods & Gilfanov 2016; Woods et al. 2017). For helium the corresponding time-scale is $\approx 7 \times 10^4$ years (see e.g. Pequignot et al. 1991). Searching for these relic nebulae around young supernova remnants and determining the ionization state of the surrounding gas can thus be used effectively to constrain the properties of the progenitor.

Previous efforts in determining the ionization state of the gas around SNRs have focused on the forward shocks. Many shock fronts around SNe Ia remnants are so-called Balmer-dominated shock fronts, where the optical emission is dominated by both broad and narrow Balmer line emission. This emission is understood to be the result of the shock interacting with the surrounding neutral hydrogen, and can thus be used in estimating the ionized fraction of hydrogen (Ghavamian et al. 2000, 2001, 2003). This method has recently been used to place stringent upper limits on the luminosity of the progenitors for SNe Ia remnants in the Galaxy and LMC (Woods et al. 2017, 2018). Any method used to determine the ionization state of the gas is very sensitive to the density of the gas, but the expanding shocks can also be used to determine the density of the surrounding gas (Badenes et al. 2007; Yamaguchi et al. 2014).

Here we report a different method for constraining the nature of SNe Ia progenitors. We have searched directly for the relic ionization nebulae around four known SNe Ia remnants in the LMC (see Table 2.1 for list of sources). Using integral field spectroscopy, we searched for and did not find any He II 4686Å emission ahead of the forward shocks. With comparison to numerical simulations performed with the photoionization code Cloudy, we placed upper limits on the luminosities as a function of the effective temperatures of the progenitors that created the observed four LMC remnants. Using these upper limits, we excluded the presence of accreting nuclear burning WDs at the sites of the remnants during

the last $\sim 10^5$ years before the explosions.

This paper is organized as follows: In Sec. 2.2 we describe our observations and the data reduction procedure. In Sec. 2.3 we describe the methods used in this paper, specifically the spectral extraction (Sec. 2.3.1) and the Cloudy simulations (Sec. 2.3.2). In Sec. 2.4 we describe our results and then discuss them and the possible implications in Sec. 2.5.

2.2 Observations

We have observed the four LMC SN Ia remnants SNR 0509-67.5, SNR 0505-67.9, SNR 0509-68.7, and SNR 0519-69.0 with the Wide Field Spectrograph (WiFeS) mounted on the Nasmyth A focus of the Australian National University 2.3 m telescope at the Siding Spring Observatory (Dopita et al. 2007, 2010). SNR 0505-67.9, SNR 0509-68.7, and SNR 0519-69.0 were observed on the nights of 2014 December 18–20 (P.I.: Seitenzahl; Proposal ID: 4140118) and SNR 0509-67.5 was observed on 2015 December 13 (P.I.: Seitenzahl; Proposal ID: 4150145). Here we provide only a short summary of the data reduction method, which is also described in detail by Dopita et al. (2016) and Ghavamian et al. (2017).

The observations were performed in the 'binned mode', which provided us a field of view of 25 × 35 spatial pixels (or spaxels), each of them $1'' \times 1''$ in angular size. The instrument is a double-beam spectrograph providing simultaneous and independent channels for both the blue and red wavelength ranges. We used the B3000 and R7000 gratings, providing a spectral resolution of R = 3000 ($\Delta v \approx 100$ km s^{-1}) in the blue wavelength range (3500–5700 Å) and R = 7000 ($\Delta v \approx 45$ km s^{-1}) in the red (5300–7000 Å).

SNR 0509-67.5, SNR 0509-68.7, and SNR 0519-69.0 were observed in a mosaic of two overlapping fields, and SNR 0505-67.9 was observed with ten fields in order to cover the whole remnant. Each field was observed in 2 × 1800s exposures, with 2 × 900s blank sky exposures, which were subtracted from the two co-added frames for each field.

The data were reduced with the PYWIFES v0.7.3 pipeline (Childress et al. 2014a,b), which provided us a wavelength calibrated, sensitivity corrected, and photometrically calibrated data cube. The final mosaics were then combined from the individually reduced cubes, with the respective alignment of each field in the mosaic derived by comparing the reconstructed continuum frames from the red cubes with the Digitized Sky Survey 2 red band image of the area. The final mosaic for SNR 0505-67.9 has dimensions of $94'' \times 96''$, and for the three other sources the dimensions are $40'' \times 36''$, which correspond to fields of 22.8 × 23.3 pc and 9.7 × 8.7 pc, respectively, assuming a distance of 50 kpc to the LMC.

2.3 Methods

2.3.1 Spectra of the remnants

In order to study the properties of the possible nebulae around the observed supernova remnants with as high sensitivity as possible, we extracted spectra from large areas sur-

Table 2.1: List of observed sources with relevant properties.

Source	Size (pc)	Age (yrs)	n_0 (cm^{-3})	N_H (10^{21} cm^{-2}) [1]	References
SNR 0509-67.5	4	400 ± 120	0.4–0.6	1.64 ± 0.07	[2]
SNR 0505-67.9[1]	7–9	∼ 4700	0.5–1.5	0.28 ± 0.001	[3]
SNR 0509-68.7[2]	4	685 ± 20	1–2.5	$3.09\ ^{+0.20}_{-0.11}$	[4]
SNR 0519-69.0	4	680 ± 200	2.4 ± 0.2	0.96 ± 0.04	[5]

[1]: Maggi et al. (2016), [2]: Rest et al. (2005); Kosenko et al. (2008), [3]: Hughes et al. (1998); Ghavamian et al. (2003), [4]: van der Heyden et al. (2002); Williams et al. (2014), [5]: Rest et al. (2005); Kosenko et al. (2010)

[1] also known as DEM L71

[2] also known as N103B

rounding each remnant. Since the expected brightness of an emission line decreases as a function of distance (see Fig. 2.3), we used the area between the outer edge of the forward shock (∼ 4 pc from the centre) and a distance of about 5 pc from the approximate geometrical centre of each source for SNR 0509-67.5, SNR 0509-68.7, and SNR 0519-69.0; for SNR 0505-67.9 the corresponding values are 7–9 pc and 10 pc. We avoided any areas with residuals from foreground star subtraction. In Fig. 2.1 we show all the four remnants with the spectral extraction areas marked.

For each source, the spectra were averaged over the specified area, corrected for the average redshift of 277.5 km s^{-1}, which was measured from the Hβ and [O III] 4959, 5007 Å emission lines (LMC peculiar velocity is 262.2 km s^{-1}; McConnachie 2012), and dereddened using the average LMC extinction curves of Weingartner & Draine (2001) with a carbon abundance $b_c = 2\times10^{-5}$ and using the H column densities for each source listed in table 2.1. An example spectrum is shown in Fig. 2.2.

No He II 4686Å emission was detected in any source before the forward shock, as is evident in Fig. 2.2. We used this lack of noticeable line emission to derive upper limits for the He II 4686Å flux by estimating the maximum level of emission which would be inseparable from the noise. In order to determine the noise level, we calculated the standard deviation of the observed flux within a wavelength window with an approximate width of 200 Å, positioned around 4686 Å so that no bright emission lines, namely Hβ, were inside the window.

Then, because the nebular He II emission is expected to be narrower than the instrumental resolution and would thus be spectrally unresolved (Gruyters et al. 2012), we assumed a gaussian line with a fixed width corresponding to the instrumental resolution of B3000 (∼ 100 km s^{-1}), and using a chi-squared test we calculated the minimum amplitude of a line, which would be statistically separable from the estimated noise level. The line was taken to be distinct from the noise, when adding the line on the spectrum increased the χ^2 value by 9, corresponding to 3σ, or 99.7 % confidence. The flux of such a gaussian line was then taken to be the upper limit of the possible He II 4686Å line flux and compared against the simulations described in Sec. 2.3.2.

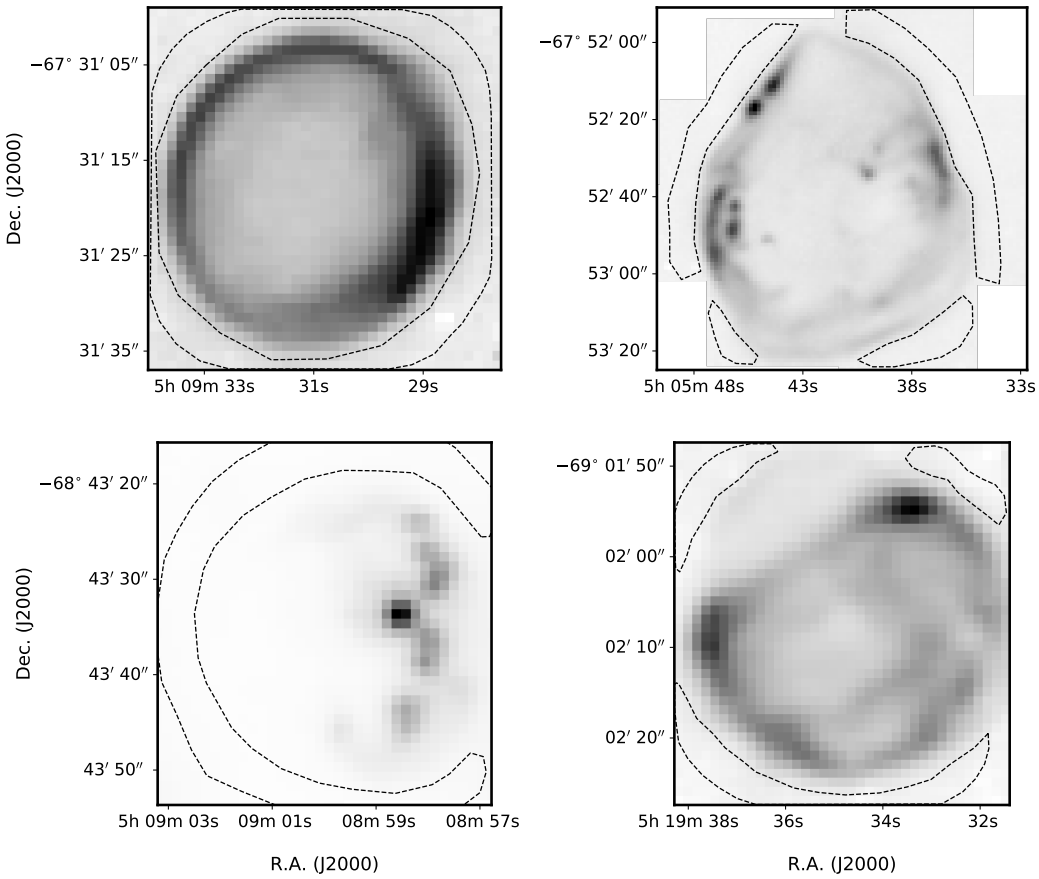

Figure 2.1: All supernova remnants in Hα with WiFeS. Top row from left to right: SNR 0509-67.5 and SNR 0505-67.9; bottom row from left to right: SNR 0509-68.7 and SNR 0519-69.0. The spectral extraction areas are outlined with the black dashed lines.

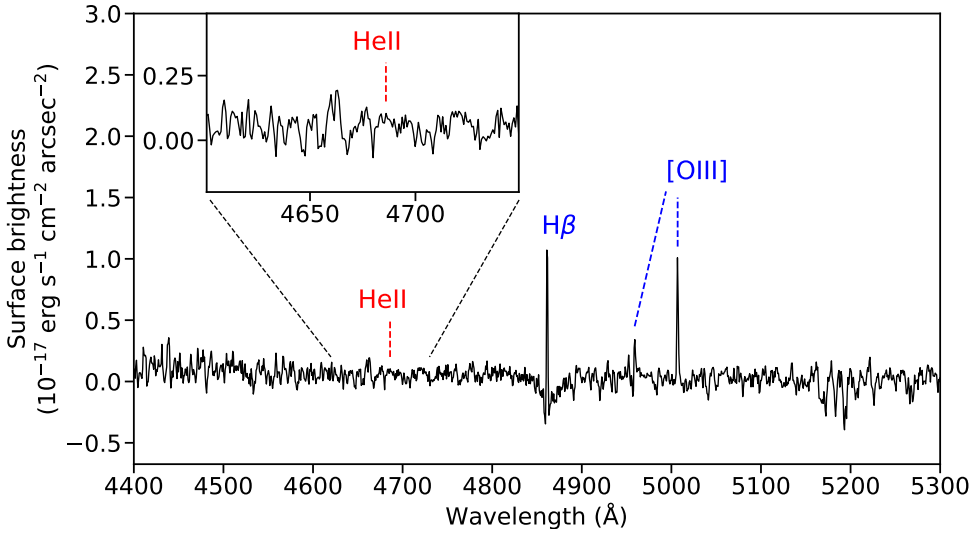

Figure 2.2: An example spectrum of the interstellar gas ahead of the forward shock around SNR 0519-69.0. On the y-axis is the mean surface brightness in units 10^{-17} erg s^{-1} cm^{-2} arcsec^{-2} and on the x-axis is the wavelength in units of Å. The inset figure shows the spectrum in more detail around the 4686 Å wavelength. In blue are marked the brightest emission lines Hβ and [O III] , and the red dashed lines indicate the 4686 Å wavelength.

2.3.2 Simulations

We computed a grid of numerical photoionization models with Cloudy[1] (v17.01; Ferland et al. 2017). We assumed a spherically symmetric and static configuration with the central ionizing source emitting a blackbody spectrum, which provides a reasonable approximation of the ionizing emission of nuclear-burning WDs, except far into the Wien tail (Chen et al. 2015; Woods & Gilfanov 2016). The effective temperature of the ionizing radiation was varied from 10^4 to 10^7 K and the bolometric luminosity from 10^{35} to 10^{38} erg s^{-1} with logarithmically evenly spaced steps. In light of the pre-shock densities of the remnants shown in Table 2.1, the density of the ambient gas was kept fixed at either 0.5, 1, or 2.4 cm^{-3}, while dust was neglected. The metallicity of the gas was set to $Z = 0.3\ Z_\odot$, where $Z_\odot$ is the solar metallicity, based on the average results of several studies on the metallicity of the ISM around many LMC SNRs, including for example SNR 0505-67.9 and SNR 0519-69.0 (Hughes et al. 1998; Maggi et al. 2016; Schenck et al. 2016).

The calculations were performed in three different ways with regard to the gas temperature: in the first case, the ambient gas temperature was calculated self-consistently and the calculations were stopped when the gas temperature dropped below 3000 K. While this is an idealized assumption, this case offers a possibility to study as an example an isolated situation, where the only source of energy is the central ionizing source. In reality,

[1] www.nublado.org

there is a diffuse emission field originating from stars and other sources in addition to the central ionizing source. Depending on the strength of the diffuse emission field, and properties of the gas, such as density, the ISM has been historically classified roughly into three different phases: a hot and very low density phase ($n \sim 10^{-2.5}$ cm^{-3}, $T \sim 10^6$ K), a warm low density phase ($n \sim 10^{-0.5}$ cm^{-3}, $T \sim 10^4$ K), and a cold dense phase ($n \sim 10^{1.5}$ cm^{-3}, $T \sim 10^2$ K) (McKee & Ostriker 1977). In the hot phase the gas is already ionized and any possible SSS would not then change the ionization state of the ISM. In the cold phase the central SSS would be the main source of energy and an ionization nebula would be clearly detectable. This phase corresponds mostly to the self-consistent temperature calculations. However, the estimated gas density limits of the SNRs studied here point mostly to the warm phase. Thus, to include the contribution from the diffuse emission in our simulations, we ran the calculations with a fixed gas temperature in addition to calculating it self-consistently. Although the relatively low temperatures of the warm low density phase are not expected to contribute significantly to the ionization of He^+ due to its high ionization potential (54.4 eV), we ran the calculations with the temperature set to either 5000 K or 10000 K in order to test the effect of the gas temperature on the He II 4686Å emission.

From the Cloudy simulations we get the volume emissivity $\epsilon_i(r)$ of a line i as a function of the distance r from the ionizing source. This can be used to find the surface brightness of a line i:

$$\mathrm{SB_i}(r) = \int_l \frac{\epsilon_i(r)}{4\pi} \mathrm{d}l, \tag{2.3}$$

where we have integrated along the line of sight l through the emission nebula. Examples of the He II 4686Å surface brightness as a function of radius for the central source temperatures of 10^{5-6} K and luminosities 10^{36-37} erg s^{-1} are shown in Fig. 2.3.

From these surface brightness profiles, we calculated the average surface brightness of the He II 4686Å emission line in the data extraction range of 4–5 pc (or 7–10 pc for SNR 0505-67.9) for each point in the temperature–luminosity grids. Then, comparing the upper limits acquired from the WiFeS observations to the grids of simulated brightnesses, we can constrain the luminosity as a function of the assumed emission temperature of the central ionizing sources.

2.4 Results

The 3σ upper limits for the surface brightness of the He II 4686Å emission line acquired for each source with the method explained in Sec. 2.3.1 are shown in Table 2.2. No noticeable He II emission was detected ahead of the forward shock in any source and the derived upper limits are within a factor of two from each other. How well the progenitor properties can be constrained, depends, however, on the size of the remnant and the density of the surrounding gas. SNR 0505-67.9 is much older and thus much larger than the other three SNRs. As shown in Fig. 2.3, the expected surface brightness decreases with the distance from the ionizing source, making it harder to constrain the progenitor luminosities of older

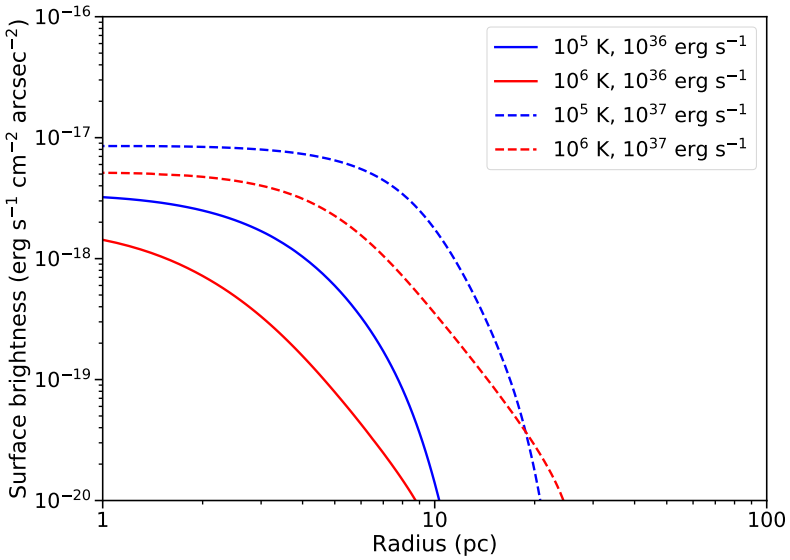

Figure 2.3: Surface brightness (in units of erg s^{-1} cm^{-2} arcsec^{-2}) profiles for He II 4686Å as a function of radius (in parsecs). Blue and red lines have blackbody temperatures of 10^5 and 10^6 K, and the solid and dashed lines have luminosities of 10^{36} and 10^{37} erg s^{-1}, respectively. The density of the gas was set to 1 cm^{-3}.

and larger SNRs.

To transform the surface brightness upper limits to limits on the progenitor luminosities, we compared the results to the Cloudy simulations, as explained in Sec. 2.3.2. The upper limits on the bolometric luminosity as a function of the assumed emission colour temperature for each source are shown in Fig. 2.4. In this figure, the parameter space above each line is ruled out, and the area below is unconstrained. Here the temperature is calculated self-consistently and the gas density is set to 1 cm^{-3}. The limits of the three young and small remnants are all almost the same. SNR 0505-67.9 deviates from the others mostly because of its greater size; the surface brightness around SNR 0505-67.9 is studied at a distance of $\approx$ 8 pc, which together with the expected surface brightness profiles of

Table 2.2: 3σ upper limits on the He II 4686Å surface brightness for each source.

Source	Surface brightness ($\times 10^{-19}$ erg s^{-1} cm^{-2} arcsec^{-2})
SNR 0509-67.5	4.2
SNR 0505-67.9	4.7
SNR 0509-68.7	5.7
SNR 0519-69.0	5.3

Fig. 2.3 results in lower constraints.

For comparison, in Fig. 2.4 are shown also the temperatures and luminosities of the accreting nuclear-burning white dwarf models of Wolf et al. (2013), with the white dwarf mass ranging from 0.51 $M_\odot$ to 1.4 $M_\odot$. All of these models lie well above the derived upper limits for all the SNRs studied in this paper. In Fig. 2.4 are also shown the parameter ranges for four well-known super-soft X-ray sources located in the Magellanic clouds: 1. CAL 87 (LMC); 2. 1E 0035.4-7230 (SMC); 3. RX J0513.9-6951 (LMC); and 4. CAL 83 (LMC) (Greiner 2000). All of these four SSSs lie in the ruled-out regions of the three young sources, with the latter three SSSs having similar temperatures and luminosities as the nuclear-burning WD models. The upper limit of the largest remnant, SNR 0505-67.9, overlaps with the parameter range of CAL 87, but one should note that CAL 87 (number 1 in Fig. 2.4), which has the lowest claimed luminosity of the four, is viewed almost edge-on, meaning that its unobscured luminosity is likely much higher (Ness et al. 2013).

In Fig. 2.4, the results for each source are shown with the gas density of the simulations set to 1 cm^{-3}, but as mentioned before, the results are affected by the assumed gas density of the simulations. To test this effect, we ran the simulations also with the gas density set either to 0.5 or 2.4 cm^{-3}, which correspond to the upper limits of the density around SNR 0509-67.5 and SNR 0519-69.0 (see Table. 2.1), respectively. The effect of the density on the results is shown in Fig. 2.5. As is evident from this figure, the highest density provides the least constraining limits, while the low and mid density limits differ only slightly from each other, with the mid density limits being the most constraining.

In addition to the density, we tested how the assumed temperature of the gas affects the results. This effect is demonstrated in Fig. 2.6, where we show the upper limits with the temperature either calculated self-consistently, fixed at 5000 K, or fixed at 10000 K. From this figure one can see that the chosen simulation temperature affects the results only very little. The reason for this is the high ionization potential of He II (54.4 eV), which requires much higher energies than available in a typical warm interstellar medium.

The upper limits on the bolometric luminosity as a function of the assumed emission colour temperature for the progenitor of SNR 0519-69.0 are also shown in Fig. 2.7. Based on the analysis presented in this paper, the parameter space above the blue line is ruled out. For comparison, the upper limits for the same source derived by Woods et al. (2018) are shown in the same figure with a black dashed line. For effective temperatures higher than $\sim 10^5$ K, our analysis provides significantly tighter constraints on the bolometric luminosity than that of Woods et al. (2018), who derived the limits using the Balmer-dominated forward shocks of the supernova remnant (see also e.g. Ghavamian et al. 2003; Woods et al. 2017). On the other hand, for temperatures lower than $\sim 10^5$ K, the work of Woods et al. (2018) provides lower upper limits on the luminosity than ours, because the incident radiation field does not possess significant amount of photons with sufficient energies to ionize He^+ ions, causing this regime to be poorly constrained by our work, while Woods et al. (2018) rely on the ionization of hydrogen, which requires considerably lower photon energies. In Fig. 2.7 is also shown for comparison the upper limits derived from pre-explosion archival *Chandra* X-ray data for SN2011fe, which has the lowest upper limits of the ten SNe Ia studied by Nielsen et al. (2012). The upper limits for SN2011fe are slightly

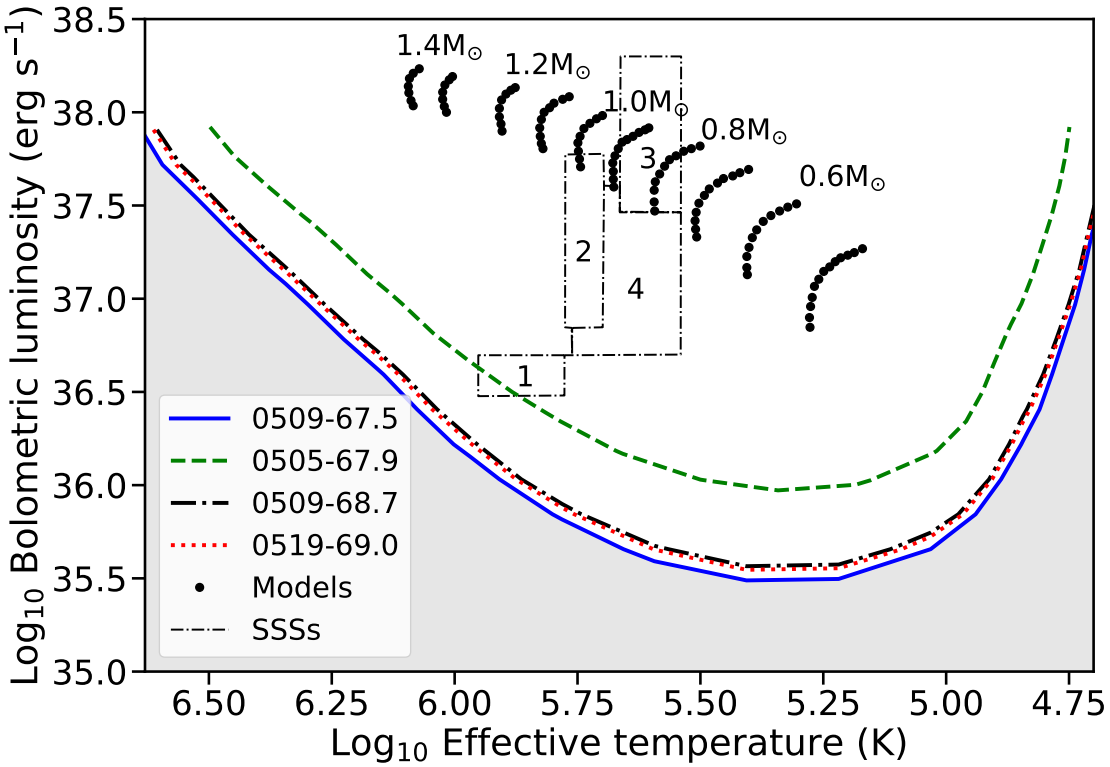

Figure 2.4: 3σ upper limits on the bolometric luminosity as a function of the assumed emission colour temperature for the progenitors of the four SNRs studied here. The blue, green, black, and red lines show the upper limits for SNR 0509-67.5, SNR 0505-67.9, SNR 0509-68.7, and SNR 0519-69.0, respectively. In all cases in this figure, the ambient gas density is set at 1 cm^{-3}, the temperature is calculated self-consistently, and the calculations terminated when the temperature dropped below 3000 K. For comparison, the black dotted lines show the accreting nuclear-burning WD models of Wolf et al. (2013) with the mass increasing from 0.51 M$_\odot$ on the left to 1.4 M$_\odot$ on the right. For ease of reading, only every second model is labelled. The black dash-dotted boxes represent the parameter ranges of four well-known SSSs: 1. CAL87; 2. 1E 0035.4-7230; 3. RX J0513.9-6951; and 4. CAL 83 (Greiner 2000).

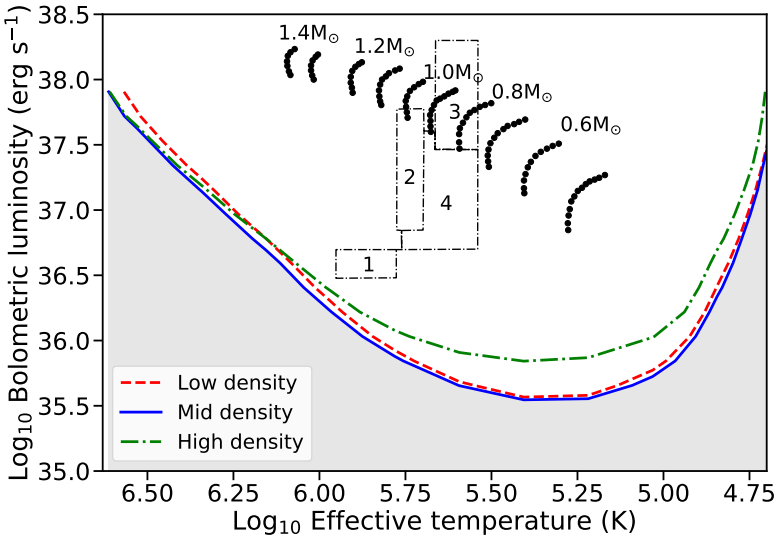

Figure 2.5: 3σ upper limits on the bolometric luminosity of the progenitor of SNR 0519-69.0 with different densities. The densities 0.5, 1, and 2.4 cm^{-3} are shown in red dashed, blue solid, and green dot–dashed lines, respectively. Also shown are the nuclear burning WD models and SSSs, as in Fig. 2.4.

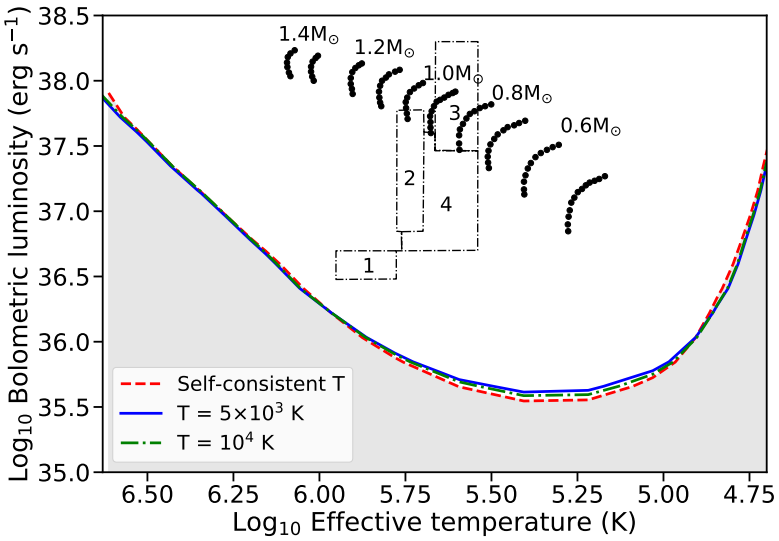

Figure 2.6: 3σ upper limits on the bolometric luminosity for SNR 0519-69.0 with different electron temperatures. The temperatures are either calculated self-consistently (red dashed line) or fixed at 5000 (blue solid) or 10000 K (green dot–dashed). The density is set to 1 cm^{-3} in all cases. Also shown are the nuclear burning WD models and SSSs, as in Fig. 2.4.

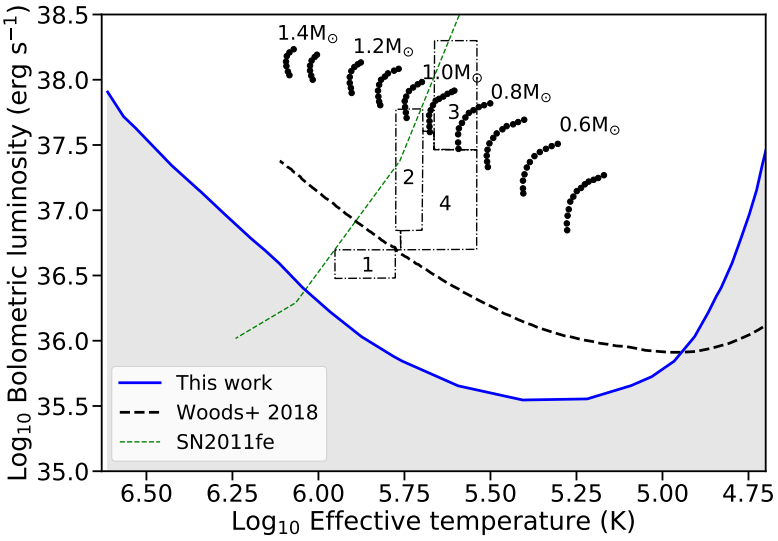

Figure 2.7: 3σ upper limits on the bolometric luminosity as a function of the emission colour temperature for the progenitor of SNR 0519-69.0. In this figure, the ambient gas density is set at 1 cm^{-3}, the temperature is calculated self-consistently and the calculations terminated when the temperature dropped below 3000 K. The solid blue line shows the upper limits derived in this paper, and for comparison the black dashed line shows the upper limit for SNR 0519-69.0 derived by Woods et al. (2018) using the Balmer-dominated shocks. The green dashed line shows the upper limit from pre-explosion archival X-ray data for SN 2011fe (Nielsen et al. 2012). Also shown are the nuclear burning WD models and SSSs, as in Fig. 2.4.

lower than our results for SNR 0519-69.0 in high temperatures ($\gtrsim 10^6$ K), for the part that there exists data for SN2011fe. In the high temperature regime our results become less constraining, because increasing the photon energies leads to less efficient ionizing of the ambient gas, which is due to the ionizing cross section of a hydrogen-like ion decreasing as a function of energy, approximately as $\sigma \propto E^{-3}$ (Hummer & Seaton 1963).

2.5 Discussion

The super-soft X-ray sources have long been suggested as possible progenitors for Type Ia supernovae. However, recent studies have constrained their viability as a progenitor channel both for large populations (Di Stefano 2010; Gilfanov & Bogdán 2010; Woods & Gilfanov 2013; Johansson et al. 2014; Woods & Gilfanov 2016) and individual supernova remnants (Nielsen et al. 2012; Woods et al. 2017, 2018; Graur & Woods 2019). In this paper, we have presented a novel method for constraining supernova progenitor properties, and using this method, we have strongly disfavoured the super-soft progenitor channel for

four Type Ia supernova remnants in the Large Magellanic Cloud.

With this method we have focused only on the He II 4686Å emission line, because its high ionization potential makes it a very distinct signature of a conventional super-soft source. However, there are also other emission lines, e.g. Hβ and [O III] 5007Å, present in the spectra of the ISM around the SNRs, as is evident from Fig. 2.2. These emission lines, while expected to be bright in a SSS nebula (Rappaport et al. 1994), are present also in a typical warm ISM in the LMC (e.g. Pellegrini et al. 2012) and thus with these lines one encounters the problem of disentangling the ionization caused by the possible progenitor from the contributions of other sources, such as the diffuse background and the shock emission (Smith et al. 1994; Ghavamian et al. 2000). For example, in the case of the most luminous allowed (by the He II analysis) source with a temperature of 10^5 K, the predicted Hβ emission line brightness is a factor of 5 lower and [O III] 5007Å brightness is 10 times lower than observed around SNR 0519-69.0.

Our results add to the growing body of evidence supporting the double degenerate scenario as a progenitor channel for these remnants. For SNR 0519-69.0 Edwards et al. (2012) ruled out all post-main-sequence stars as possible surviving ex-companions and thus claim that among the published single-degenerate models, only the super-soft X-ray source model is a possibility for this remnant. In addition, SNR 0519-69.0 has a tilted axisymmetric morphology and high oxygen abundance, which points to an oxygen-rich merger (Kosenko et al. 2010, 2015). Taking these together with our results, which rule out a SSS as a plausible progenitor, it seems clear that the only viable origin of SNR 0519-69.0 was the merger of two white dwarfs. Similarly for SNR 0509-67.5 Schaefer & Pagnotta (2012) ruled out all possible surviving companion stars in the centre of the remnant, and thus ruled out all single degenerate scenarios as a progenitor channel for this remnant, which is in good agreement with our results.

Our results disfavour SSSs as possible progenitors, but we made some simplifications along the way, which should be considered in detail. Firstly, we assumed that the luminosity remained constant throughout stable accretion and nuclear burning, although in reality these sources exhibit complex variability. However, for variable sources, the parameter of interest is the time-averaged luminosity, which determines the average ionization state of the gas, and thus given a sufficiently long time-scale, the system can be well approximated with a constant luminosity case (Chiang & Rappaport 1996; Woods et al. 2017). The detailed structure of ionization nebulae may change based on the behaviour of the central source, for example in the case of nova outbursts. Such cases, and the time variability of the source and nebulae, will be addressed in future studies.

Secondly, the calculations were carried out in steady-state, i.e. assuming an equilibrium state between ionization and recombination, where the central source continues to supply the nebula with ionizing photons. This is obviously not the case for SNRs, where the possible central ionizing source has exploded and the emission has ceased. Nevertheless, this is a reasonable assumption in the case of young SNRs, where the age (¡ 1000 yrs) is much smaller than the typical recombination time-scale of the ISM ($\sim 10^5$ yrs). This argument raises the question, however, of whether there could be a long delay between the explosion and the ionizing phase. This can be achieved with spin-up/spin-down models

(Justham 2011), where the accreting WD is spun up because of the accreted angular momentum. Because of the high spin rates, the mass of the WD can increase beyond the critical mass, and only after accretion has ceased and the spin rate of the WD has decreased can the WD explode as a supernova. If the spin-down time is longer than the recombination time, this model can produce super-Chandrasekhar single-degenerate explosions surrounded by neutral gas. In addition, by the time of the explosion, the donor star may have exhausted its stellar envelope and become a WD, rendering it difficult to detect in post-explosion companion searches (Di Stefano et al. 2011). In fact, such super-Chandrasekhar explosions would be preferentially overluminous, "1991T-like" events (Fisher et al. 1999). This is thought to be the case for SNR 0509-67.5, which Rest et al. (2008) showed to be a 1991T-like event using its light echoes, a result at which Badenes et al. (2008) also arrived independently, using the remnant dynamics and X-ray spectroscopy. Super-Chandrasekhar-mass explosions, however, can also result from double-degenerate mergers, which lack the issues facing spin-up/spin-down models, such as the scarcity of observed rapidly-spinning WDs (Di Stefano et al. 2011; Maoz et al. 2014).

Thirdly, in the analysis presented here, we have considered only unobscured sources, where all the emitted radiation contributes to the ionization of the surrounding gas. The emission could, however, be obscured by a fast-moving and optically-thick stellar wind, if the WD were accreting at higher rates than the steady nuclear-burning regime (Hachisu et al. 1996; Wolf et al. 2013). If the wind mass-loss rate were high enough to obscure the central source, however, the wind should excavate a large ($\gtrsim$ 10 pc) low-density cavity around the progenitor, which should be easily distinguished from the undisturbed ISM. Such large cavities are incompatible with the remnants' dynamics for the three young supernova remnants studied here (Badenes et al. 2007), and the densities (see Table 2.1) and evolution of the remnants are consistent with expansion into a uniform and undisturbed ISM (Maggi et al. 2016). In addition to a wind from the accreting WD, a slow and dense wind from a giant companion star may obscure the ionizing radiation, if the mass-loss rate is $\gtrsim 10^{-6}$ $M_\odot$ yr^{-1} (Nielsen & Gilfanov 2015). However, such a scenario is disfavoured for SNe Ia progenitors, given the strong constrains on circumstellar interactions both from radio (Chomiuk et al. 2012, 2016) and X-ray observations (Margutti et al. 2012, 2014), and the lack of detected giant companions (Edwards et al. 2012; Schaefer & Pagnotta 2012; Olling et al. 2015).

Therefore, we may conclude that none of the progenitors of the Magellanic supernova remnants considered here were super-soft X-ray sources for a significant fraction of the last 100,000 years preceding their detonation. Future spectroscopic observations can extend these limits to all nearby, recent SNe Ia and supernova remnants, or in the event of a detection, provide the first measurement of the luminosity and temperature of a SN Ia progenitor.

Chapter 3

LIN 358: A symbiotic binary accreting above the steady hydrogen fusion limit

The contents of this chapter have been published in Kuuttila et al. (2021) Monthly Notices of Royal Astronomical Society, 500, 3763

Abstract Symbiotic binaries are long period interacting binaries consisting of a white dwarf (WD) accreting material from a cool evolved giant star via stellar winds. In this paper we study the symbiotic binary LIN 358 located in the SMC. We have observed LIN 358 with the integral field spectrograph WiFeS and obtained its line emission spectrum. With the help of the plasma simulation and spectral synthesis code CLOUDY, we have constructed a 2D photo-ionisation model of LIN 358. From comparison with the observations, we have determined the colour temperature of the WD in LIN 358 to be 19 eV, its bolometric luminosity $L = (1.02 \pm 0.15) \times 10^{38}$ erg s^{-1}, and the mass-loss rate from the donor star to be 1.2×10^{-6} M$_\odot$ yr^{-1}. Assuming a solar H to He ratio in the wind material, a lower limit to the accreted mass fraction in LIN 358 is 0.31. The high mass-accretion efficiency of a wind Roche lobe overflow implies that the WD is accreting above the upper boundary of stable hydrogen fusion and thus growing in mass with the maximal rate of $\approx 4 \times 10^{-7}$ M$_\odot$ yr^{-1}. This causes the WD photosphere to expand, which explains its low colour temperature. Our calculations show that the circumstellar material in LIN 358 is nearly completely ionized except for a narrow cone around the donor star, and that the WD emission is freely escaping the system. However, due to its low colour temperature, this emission can be easily attenuated by even moderate amounts of neutral ISM. We speculate that other symbiotic systems may be operating in a similar regime, thus explaining the paucity of observed systems.

3.1 Introduction

Symbiotic binaries, or symbiotic stars, are interacting binaries consisting of a hot compact object, usually a white dwarf (WD), though neutron stars are also possible, accreting material from a cool evolved giant. The donor star can be either a normal red giant (S-type) or a Mira type variable embedded in an optically thick dust shell (D-type). Symbiotic binaries have the longest orbital separations and periods among the interacting binaries, with the periods ranging up to tens of years in D-type binaries (e.g. 43.6 years for R Aqr; Gromadzki & Mikołajewska 2009). To date, there are 257 confirmed symbiotic binaries in the Milky Way and 66 extra-galactic objects (Akras et al. 2019a), which is much less than predicted by theoretical estimates, which range from 10^3 (e.g. Lü et al. 2006; Yungelson 2010) to a few times 10^5 (Magrini et al. 2003).

Symbiotic binaries are surrounded by a complex circumstellar environment, the result of the hot ionizing compact object being embedded in the dense neutral wind of the giant star, with both ionized and neutral regions present as well as dust forming regions, accretion discs and possibly jets. The vast array of differing conditions makes symbiotic binaries excellent test cases of late stages of stellar evolution and binary interactions. In addition, symbiotic binaries have been discussed in the context of the problem of progenitors of Type Ia supernovae (SNe Ia) (see Maoz et al. 2014, for a review), both in single and double degenerate channels, and also as a possible channel of neutron star formation via accretion-induced collapse (AIC; Nomoto & Kondo 1991; Wang 2018). For a thorough review of symbiotic binaries, see Mikołajewska (2012).

Symbiotic binaries may also exhibit other phenomena usually associated with accreting white dwarfs, such as thermonuclear novae, either slow or recurrent, where the hydrogen accreted from the giant onto the WD burns into heavier elements, either in a long outburst or in a short flash. These novae typically cause some amount of matter to be ejected from the WD, which may prevent the WD from growing in mass (Wolf et al. 2013), except in the case of short recurrence time novae, where the WD can retain a significant amount of the accreted material due to the higher interior temperature and thus less explosive burning (Hillman et al. 2016). If the WD in the binary is accreting material steadily, the system may appear as a super-soft X-ray binary (SSS), which is characterised by effective temperatures of 10^{5-6} K and luminosities of 10^{37-38} erg s^{-1} (Greiner 2000). In the SSS phase the accreted hydrogen is burned steadily on the surface of the white dwarf, which allows the mass of the WD to grow efficiently (van den Heuvel et al. 1992).

LIN 358, also known as RX J0059.1-7505, is an S-type symbiotic binary consisting of a WD and an asymptotic giant branch (AGB) star and located in the outskirts of the Small Magellanic Cloud (SMC) at coordinates RA = 00h 59m 12.3s, Dec = -75° 05′ 17.6″. It was first discovered by Lindsay (1961) and characterised as a symbiotic binary by Walker (1983) using optical observations. Muerset et al. (1997) analysed the ROSAT PSPC observations of LIN 358 and classified it as a super-soft X-ray source based on its X-ray spectrum. Kahabka & Haberl (2006) observed LIN 358 with XMM-Newton and obtained an effective temperature of $T_h = 227.5 \pm 30$ kK and luminosity $L_h = 1.0 \times 10^{38}$ erg s^{-1} for the hot component of the binary from their black-body fit to the super-soft component (0.13 – 1.0

keV). LIN 358 was also studied by Skopal (2015), who used multi-wavelength modelling of the spectral energy distribution to determine the effective temperature $T_h = 250 \pm 10$ kK and luminosity $\log_{10}(L_h) = 38.03 \pm 0.11$ erg s^{-1} for the WD, in agreement with the previous X-ray analysis. In addition, Skopal (2015) derived the effective temperature $T_{\rm g} = 4000 \pm 200$ K, bolometric luminosity $L_g = (2.8 \pm 0.8) \times 10^{37}\,(d/60{\rm kpc})^2$ erg s^{-1}, and the radius $R_g = 178\,(d/60{\rm kpc})^2$ R$_\odot$ for the giant star. Skopal (2015) determined the properties of the giant by matching the photometric *BVJHK* flux points with a synthetic spectrum calculated for $T_{\rm g} = 4000 \pm 200$ K from a grid of giant atmosphere models calculated by Hauschildt et al. (1999). This is possible due to the fact that in the near-IR the emission from the AGB star dominates over the emission from both the WD, which peaks in the UV, and the ionized nebula, which is most prominent in the optical lines (Skopal 2005). Using these parameters Skopal (2015) classified the giant star in LIN 358 to be a type K5 Ib supergiant.

Apart from the temperatures and luminosities, not much is known about this system. In particular, the mass accretion rate and the mass of the WD, which are the most important parameters in determining the much speculated viability of symbiotic binaries as Type Ia supernova progenitors, are still unknown. In this work we determine the temperature, mass, and mass accretion rate of LIN 358 by using our new optical spectroscopic observations together with photoionization calculations performed with the spectral synthesis code Cloudy. This paper is organised as follows: In Sec. 3.2 we review the overall properties and geometry of LIN 358. In Sec. 3.3 we describe our observations and the data reduction procedure, in Sec. 3.4 we present the data, and in Sec. 3.5 we describe the Cloudy simulations. In Sec. 3.6 we present our results and discuss the possible implications.

3.2 LIN 358 overview

3.2.1 Mass estimation

Skopal (2015) classified the cool giant in LIN 358 to be a K5 Ib type supergiant by matching the photometric BVJHK flux points of Muerset et al. (1996) to the spectral models calculated by Hauschildt et al. (1999). These models were calculated for a mass of 5 M$_\odot$, which is a quite typical mass for a cool supergiant AGB star of this spectral type (Hohle et al. 2010), so we have adopted 5 M$_\odot$ to be the mass of the giant star in LIN 358.

The mass of the giant star is important in estimating a lower limit for the WD mass, assuming that both of the stars in the binary were born at the same time. If the current giant has a mass of 5 M$_\odot$, then the progenitor star of the WD should have had larger initial mass in order to evolve before the current giant star. According to the initial mass – WD mass relationship of Cummings et al. (2018), a star with an initial mass >5 M$_\odot$ should create a WD with mass >1 M$_\odot$. In addition, the X-ray spectral fits of LIN358 by Orio et al. (2007) indicate a WD mass > 1.18 M$_\odot$. In the rest of the paper we have assumed a mass of 1 M$_\odot$ for the WD. We note, however, that our results are only weakly sensitive to the adopted masses, because they affect only the orbital separation of the binary (Sec. 3.2.2),

which in turn does not affect our results significantly (see Sec. 3.7).

The mass of the WD has important implications on the composition of the WD, because the maximum mass of a newborn carbon and oxygen (CO) rich WDs is ~ 1.2 $M_\odot$. AGB stars with masses $\gtrsim 6$ $M_\odot$ produce higher mass WDs, which are believed to be formed as oxygen, neon, and magnesium (ONeMg) rich. This in turn affects the possible end results of the binary, because only CO WDs are thought to produce SNe Ia and ONeMg WDs are believed to form neutron stars via AIC (Nomoto 1984; Nomoto & Kondo 1991).

The mass estimates can be affected also by the pre-WD binary evolution. When the current WD went through the AGB phase, it lost the majority of its mass through stellar winds, and fraction of the mass lost may have been accreted by the second star, thus skewing the current mass ratio (van den Heuvel 1994). A careful modelling of the binary properties is required to examine this problem and is thus outside the scope of this paper. This effect, however, is likely not significant for our results, because the typical mass accreted mass is only ~ 10 % of the mass lost by the former AGB star. In the rest of the paper we have assumed that there were not any significant interactions before the current evolutionary stage.

3.2.2 Orbital parameters

Despite the large orbital periods, the WDs in symbiotic binaries are often accreting material efficiently from the AGB star. However, in most symbiotic binaries, the orbital separation is too large for the standard Roche lobe overflow (RLOF) scenario. In addition, interaction via RLOF from an AGB star with a deep convective envelope may often lead to unstable mass transfer (Hjellming & Webbink 1987; Chen & Han 2008, though see e.g., Woods & Ivanova 2011) and a common envelope phase (Paczynski 1976).

AGB stars are known to have strong stellar winds with mass-loss rates on the order of $10^{-8} - 10^{-5}$ $M_\odot$ yr^{-1} and low velocities on the order of $5 - 30$ km s^{-1} (Höfner & Olofsson 2018). Therefore, instead of RLOF, the WD is assumed to accrete material from the wind of the donor star. However, the standard Bondi-Hoyle-Lyttleton (BHL; Hoyle & Lyttleton 1939; Bondi & Hoyle 1944) wind accretion scenario often fails to explain the required mass accretion rates. The BHL description is a good approximation of the wind accretion when the outflow velocity is fast compared to the orbital velocity, which is not the case for typical AGB winds.

Recent simulations suggest a new mode of mass transfer, called wind Roche lobe overflow (WRLOF; Mohamed & Podsiadlowski 2007, 2012), where the star itself does not fill the Roche lobe, but the stellar wind is confined in the Roche lobe, because the wind acceleration radius R_d is larger than the Roche lobe radius $R_{L,1}$. In this situation the wind is focused towards the orbital plane (de Val-Borro et al. 2009), allowing an efficient mass transfer through the Lagrangian 1 (L1) point. In WRLOF the mass-transfer rate may exceed the estimated rates from the simple BHL accretion by up to 2 orders of magnitude.

The conditions necessary for WRLOF can be estimated with the ratio $R_d/R_{L,1}$. The Roche-lobe radius of the donor star $R_{L,1}$ depends on the mass ratio q and the binary

separation a, and can be estimated as (Eggleton 1983):

$$R_{L,1} \;=\; a \;\times\; \frac{0.49q^{2/3}}{0.6q^{2/3} + \ln(1+q^{1/3})}. \tag{3.1}$$

In AGB stars, the stellar winds are driven by dust (Höfner 2015; Höfner & Olofsson 2018), which means that the wind acceleration radius coincides with the dust condensation radius, i.e. the radius where the gas is cooled enough to form dust grains. This radius can be estimated as (Lamers & Cassinelli 1999; Höfner 2007):

$$R_d \;=\; \frac{1}{2} R_* \left(\frac{T_{\rm g}}{T_{\rm cond}} \right)^{\frac{4+p}{2}}, \tag{3.2}$$

where R_* is the stellar radius and T_g is the temperature of donor star. The condensation temperature $T_{\rm cond}$ and the exponent p are characteristics of the grain material and depend on the chemical composition.

LIN 358 is an S-type symbiotic binary (Muerset et al. 1996), which means the infrared emission is dominated by the stellar continuum and not the dust emission as in D-type binaries. The dust grains are important in driving the stellar wind (Höfner & Olofsson 2018), but the emission from the WD will later destroy the dust grains and ionize most of the wind (see Sec. 3.7.3).

The atmosphere of the AGB star in LIN358 is O-rich (Muerset et al. 1996), meaning the condensing grains are mainly various silicates. The exact nature of the O-rich condensates is still debated, but following Bladh & Höfner (2012); Bladh et al. (2015); Höfner et al. (2016); Höfner & Olofsson (2018), for the most efficient silicate grains $p \approx -1.0$ and $T_{\rm cond} \approx 1100$ K. Using these values in Eq. (3.2), we get $R_d = 617.2$ R$_\odot$ (≈ 2.9 AU).

Next, we can estimate the orbital separation a in LIN 358 by using the ratio of the wind acceleration radius and the Roche lobe radius of the donor $R_d/R_{L,1}$. Based on the hydrodynamical simulations of Mohamed & Podsiadlowski (2012); Abate et al. (2013), the maximal accretion efficiency is reached at $R_d/R_{L,1} = 1.5$. Using this with the Eq. (3.1), we can calculate the semi-major axis to be $a = 3.7$ AU, which corresponds to a orbital period of ≈ 2.9 years. This is well within the range of typical periods for S-type symbiotic binaries ($\sim 1 - 6$ years; Gromadzki et al. 2013).

In the rest of the paper we have used the $a = 3.7$ AU, but we note that our results are not particularly sensitive to this chosen value (see Sec. 3.7).

3.3 Observations

We observed LIN 358 on the nights of 2018 November 04–05 (P.I.: Seitenzahl; Proposal ID: 4180034) with the Wide Field Spectrograph (WiFeS) mounted on the Australian National University 2.3 m telescope at the Siding Spring Observatory. We present only a short summary of the data reduction method, which is described in detail by Dopita et al. (2016) and Ghavamian et al. (2017).

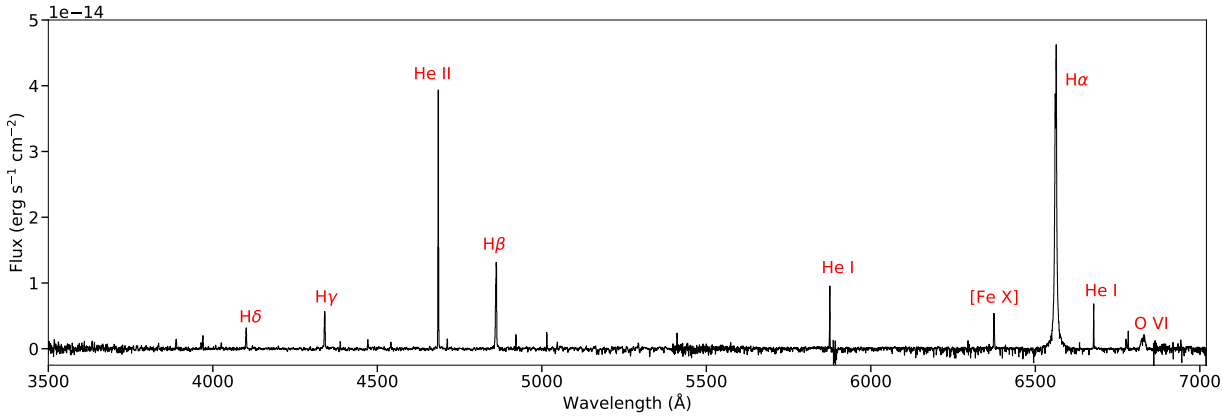

Figure 3.1: The spectrum of LIN 358 as observed with WiFeS.

The WiFeS is a double-beam spectrograph which provides simultaneous and independent channels for both the blue (3500–5700 Å) and red (5300–7000 Å) wavelength ranges. We used the B3000 and R7000 gratings which means the spectral resolution in the blue wavelength range is R = 3000 ($\Delta v \approx 100$ km s^{-1}) and in the red R = 7000 ($\Delta v \approx 45$ km s^{-1}). The observations were performed in the 'binned mode', which provided us a field of view of 25 × 35 spatial pixels (or spaxels), each of them 1″ × 1″ in angular size. This correspond to a field of view of 7.3 pc × 10.2 pc assuming a distance of 60 kpc to the SMC.[1] LIN 358 was observed in one pointing which was offset from the source by 15″ in the axis of the wider side of the WiFeS field of view (35 spaxels, or 35″). The observations consisted of 2 × 1800s on source exposures and 2 × 900s blank sky exposures, which were scaled and subtracted from the two co-added frames.

The data were reduced with the PYWIFES v0.7.3 pipeline (Childress et al. 2014a,b), which provided us a wavelength calibrated, sensitivity corrected, and photometrically calibrated data cube. The data were dereddened using the extinction curves for SMC bar of Weingartner & Draine (2001) with an assumed carbon abundance of zero and using the column density $N_H = 7.6 \times 10^{20}$ cm^{-2} obtained by Kahabka & Haberl (2006) from blackbody fits to the *XMM-Newton* data. LIN 358 is located in the outskirts of the SMC, not in the bar, but given the lack of an available extinction curve for this region, we use the curve for the SMC bar. This does not affect the results significantly because the dereddening factor for e.g. the He II 4686 Å line is only ≈ 1.04, so our measured fluxes may be underestimated at most by a few per cent, which is of the same order as the measured flux errors.

In addition, we corrected the data for the redshift of 185.2 km s^{-1}, which was measured from several narrow emission lines (SMC heliocentric radial velocity is 145.6 km s^{-1}; McConnachie 2012), and subtracted the continuum emission using the Locally Weighted Scatterplot Smoothing algorithm (LOWESS; Cleveland 1979) similarly to Vogt et al. (2017b,a).

[1] Scowcroft et al. (2016) found the the distance to SMC to be 62.0 ± 0.3 kpc, but for easier comparison with previous results we have assumed a 60 kpc distance in this paper.

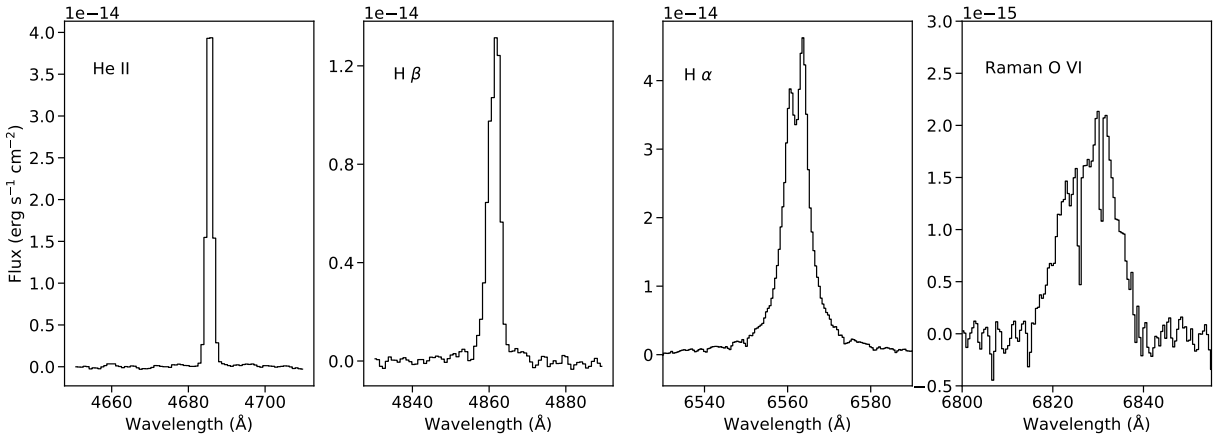

Figure 3.2: The observed line profiles from left to right: He II 4686Å, Hβ, Hα, and the Raman scattered O VI 6830 Å.

Table 3.1: List of the luminosities of the brightest observed emission lines.

Emission line	Luminosity $\times$ 10^{33} (erg s^{-1})
He II 4686	38.0 $\pm$ 1.2
H β	23.1 $\pm$ 2.7
He I 5876	6.2 $\pm$ 0.3
[Fe X] 6374	7.4 $\pm$ 0.4
H α	112.3 $\pm$ 8.1
He I 6678	4.3 $\pm$ 0.2

3.4 Data

After the data reduction process described in Sec. 3.3 we extracted the total source spectrum from the blue and red data cubes. The overall spectrum is show in Fig. 3.1. The spectrum consists of various emission lines: H Balmer series from Hα to the $n = 10 \rightarrow 2$ transition; various He I and He II lines, most notably He II 4686 Å, He I 5876 Å, and He I 6678 Å; [Fe X] 6374 Å, and the [O VI] 6830 Å Raman scattered feature. The usual nebular lines, such as [O III] 4959, 5007 Å and [S II] 6716, 6731 Å are notably absent in LIN 358. In our analysis we will focus mainly on the brightest observed lines, whose line luminosities are listed in Table 3.1 and whose properties are outlined below.

3.4.1 He II 4686 Å

The He II 4686 Å is the second brightest emission line in the spectrum with a luminosity L = $3.8 \pm 0.12 \times 10^{34}$ erg s^{-1}. This line comes from the n= 4 $\rightarrow$ 3 transition and is the brightest He II line in the optical. The high ionization potential of He II (54.4 eV) requires a hot ($\gtrsim 10^5$ K) ionizing source, which makes this emission line a clear and important

signature of an accreting white dwarf with steady nuclear burning (Rappaport et al. 1994). For this reason this emission line has been used extensively in previous accreting WD and Type Ia supernova studies (Woods & Gilfanov 2013; Johansson et al. 2014; Chen et al. 2015; Woods & Gilfanov 2016; Kuuttila et al. 2019). Other observed He II lines are at 4199 Å, 4541 Å, and 5411 Å.

3.4.2 He I lines

The two brightest He I lines are at 5876 Å and 6678 Å, which are produced by the singlet transition $3^1D \rightarrow 2^1P^0$ and the triplet transition $3^3D \rightarrow 2^3P^0$, respectively. Other observed He I lines include the triplet lines at 3889 Å and 4471 Å, and the singlet lines at 3965 Å, 4922 Å, and 5016 Å.

Due to the high meta-stability of the He I excited level 2^3S, and to a lesser extent 2^1S, collisional effects play a significant role in the production of He I emission lines. Of the recombinations to excited levels of He I, approximately one fourth are to the singlet levels and three fourths are to the triplet levels, all of which eventually cascade down to the meta-stable 2^3S level through radiative transitions (Osterbrock & Ferland 2006). The 2^3S level can decay to the ground state by emitting a photon, but at densities $\gtrsim 10^4$ cm^{-3} most of the 2^3S states are depopulated by collisional transitions, for example to the singlet level 2^1S and triplet 2^3P^0 (Bray et al. 2000). These collisional effects become even more important in the high densities and temperatures of symbiotic binaries. Calculating the luminosities of these lines thus requires a full treatment of all radiative and collisional processes.

3.4.3 Balmer lines

The Hα and Hβ emission lines are among the most important astrophysical lines and typically are very well understood. However, in the case of LIN 358, the high density makes the treatment of these lines quite difficult. In lower density environments (e.g., n $\ll 10^6$ cm^{-3}, see Hummer & Storey 1987), Hα and Hβ emissivities can be treated using the simple Case B approximation (Osterbrock & Ferland 2006). In the high density environment of symbiotic binaries, however, this is not the case, which is evident from the observed line ratio Hα/H$\beta \approx 4.9$, compared to the Case B line ratio Hα/H$\beta \sim 3$. The high densities and large optical depths in the nebulae around symbiotic binaries can cause the gas to become optically thick in the Balmer lines and self-absorption to occur.This will drastically change the Balmer line ratios, as has been observed in some active galactic nuclei (Netzer 1975) and also other symbiotic binaries (Davidsen et al. 1977). These conditions require a full radiative transfer treatment to fully model the line luminosities and ratios.

The observed Hα and Hβ line profiles are shown in Fig. 3.2. Hα requires four Gaussians components to be explained well: two narrow peaks, an intermediate component, and very broad ($\sim$ 2000 km/s) wings. These kind of emission line profiles have been previously observed in many planetary nebulae and symbiotic binaries (e.g. Arrieta & Torres-Peimbert 2003; Chang et al. 2018). There are several different possible formation mechanisms for

the broad wings, e.g. optically thin stellar winds from the hot component (Skopal 2006), Thomson scattering by free electrons (Sekeráš & Skopal 2012), and Raman scattering of Lyβ photons (Nussbaumer et al. 1989; Lee 2000). The Raman scattering is favoured by the fact that there are no clear broad components in the other hydrogen lines, because with Thomson wings Hα and Hβ would have the same width that is proportional to $T_e^{1/2}$, which is not the case in LIN 358. However, according to simulations of Chang et al. (2018), the Raman wings of Hα are about three times wider than the Raman wings of Hβ due to the different cross sections for Lyβ and Lyγ, which fits the picture of LIN 358. In addition, the observed O VI 6830 Å Raman feature shows that the conditions for Raman scattering are met, so it is reasonable to assume that the Balmer lines include a contribution from Raman scattering as well.

In order to estimate the Balmer emission coming from the ionized region around the WD, we modelled the Raman scattered component with the simulated line profile of Chang et al. (2018, Fig. 6) for $N_{\rm HI} = 10^{20}$ cm^{-2}. After subtracting the Raman scattered component, the resulting line profile can be well fitted with two Gaussians, one emission line and one absorption line, see Fig. 3.3.

3.4.4 [Fe X] 6374 Å

The coronal [Fe X] 6374 Å line is the only forbidden line present in our data. This lines comes from the $^2P_{1/2} \rightarrow ^2P_{3/2}$ transition of Fe^{9+}. The ionisation energy of Fe^{9+} is 233.6 eV, which makes this line very dependent on the temperature and thus a good, almost model independent test case. The complicated and poorly known wind and accretion structures of symbiotic binaries make simulating the low energy lines, e.g. He I and Balmer lines, a very difficult task, but the high ionisation energy of Fe^{9+} means that the emission originates from very close to the WD, which means that this line is insensitive to the large scale wind structure.

3.4.5 O VI 6830 Å Raman feature

The broad O VI 6830 Å feature is due to inelastic scattering of O VI 1032 Å photons by hydrogen atoms. In this Raman scattering process the O VI photons are absorbed by a hydrogen atom at the ground state ($1s^2$S), which is then excited to an intermediate state. A photon with $\lambda \sim 6830$ Å is then emitted and the hydrogen is left in an excited state ($2s^2$S) (Schmid 1989). This Raman scattering process requires an ionising source hot enough to produce O VI in the vicinity of large amount of neutral hydrogen. The Raman scattering cross-section is $7.5 \times \sigma_{\rm T} \approx 5 \times 10^{-24}$ cm^2, where $\sigma_{\rm T}$ is the Thomson cross-section (Schmid 1989; Lee & Lee 1997). For an optical depth of 1, column densities of $N_H \approx 1/\sigma \approx 2 \times 10^{23}$ cm^2 are needed. Such densities are typically reached only in the innermost parts of the wind, or in the photosphere of the donor star (see also Fig. 3.13).

The Raman scattered feature is observed almost exclusively in symbiotic binaries ($\approx$ 55% of them in the Milky Way; Akras et al. 2019a), together with the 7088 Å feature, which comes from Raman scattering of O VI 1038 Å (this is outside of the WiFeS R7000

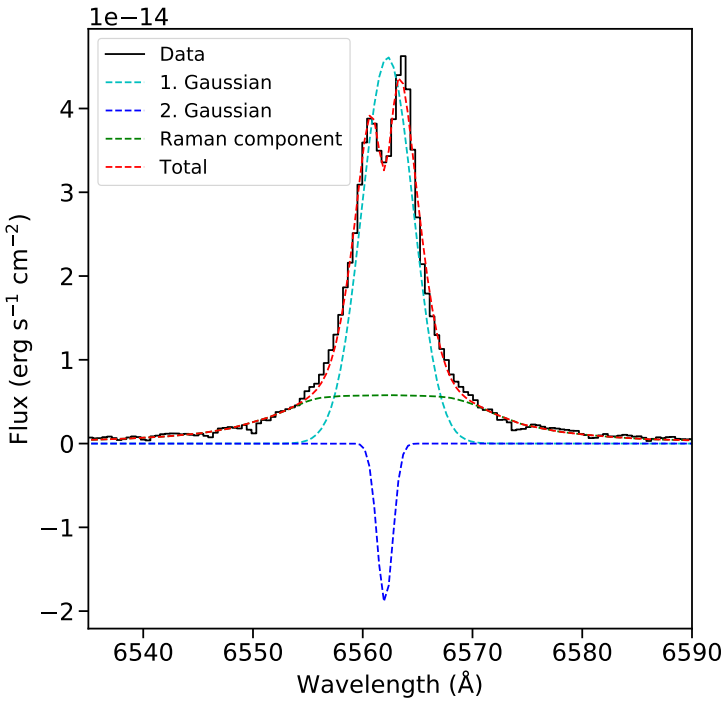

Figure 3.3: The Hα line profile with fitted components. The black line is the observed data, green dashed line is the simulated line profile of Chang et al. (2018, Fig. 6) for N_{HI} = 10^{20} cm^{-2}, in cyan and blue dashed lines are the two Gaussian components, and in the red is the sum of all three.

wavelength range). Other Raman scattered lines, e.g. He II 1025 Å → 6545 Å (Sekeráš & Skopal 2015), have also been detected in some symbiotic systems, but these are mostly very faint and thus not detectable in our observations of LIN 358.

3.5 Cloudy simulations setup

As described in Sec. 3.4, many of the observed lines in the high density nebulae around symbiotic binaries are products of complicated radiative and collisional processes, and thus explaining the source properties via these emission lines requires a detailed, simultaneous and self-consistent treatment of all the necessary complex processes. To tackle this problem, we used the open source spectral synthesis code Cloudy[2] version 17.01 (Ferland et al. 2017) to simulate the LIN 358 system.

We calculated a grid of photoionization models while assuming that the central ionizing source (the WD) emitted a blackbody spectrum, which is a reasonable approximation for the ionizing emission of nuclear burning WDs (Woods & Gilfanov 2016). We have ignored the radiation from the giant star, because of its low effective temperature (4000 K). While

[2]www.nublado.org

the giant star dominates the infrared emission, its contribution to the optical line emission is very small compared to the white dwarf.

In our simulations the metallicity of the gas was set to one fifth of solar metallicity from Lee et al. (2005); Grevesse et al. (2010), corresponding roughly to a typical SMC metallicity. A diffuse background radiation field was included in the calculations in the standard way it is implemented in Cloudy, where the radiation field shape and intensity were set to describe the cosmic radio to X-ray background (Ostriker & Ikeuchi 1983; Ikeuchi & Ostriker 1986; Vedel et al. 1994) with the cosmic microwave background included, and the extra heating and ionisation of cosmic rays were included in the calculations according to the mean ionisation rate of Indriolo et al. (2007).

3.5.1 Density structure

As mentioned in Sec. 3.2, the ionising source in symbiotic binaries sits in the dense wind emitted by the giant donor star, which makes the density structure around the WD asymmetric. This makes simulating these complex objects with Cloudy problematic, because Cloudy is a one dimensional code. LIN 358 and other symbiotic binaries have been previously studied with Cloudy (see Orio et al. 2007, for LIN 358). However, our initial attempts to compute the nebula spectrum in 1D Cloudy calculations grossly failed in explaining our observations. This is probably not surprising, given that the density profile towards the donor star is very different from the density profile in the opposite direction. For this reason, we constructed a model where we calculate the ionized gas structure with Cloudy along a number of paths from the WD and combine the results to get the 2D gas structure. We assume that the WD and the giant star are separated by 3.7 AU (see Sec. 3.2) and that the mass-loss from the giant is spherically symmetric so that the ionization structure becomes rotationally symmetric along the axis between the WD and the giant star, and we can restrict the calculations to a 2D plane.

The real situation is naturally more complex. The wind in AGB stars is driven by stellar pulsations and thus variable both in direction and time. However, the long-term average mass-loss is still often well approximated by a spherically symmetric formula (Höfner & Olofsson 2018). Furthermore, hydrodynamical simulations (e.g. Mohamed & Podsiadlowski 2007, 2012; de Val-Borro et al. 2009) show that the wind in symbiotic binaries is focused towards the binary orbital plane. Accurately accounting for this effect would require full 3D radiative transfer simulations, which is outside the scope of this paper. We note, however, that the wind focusing in this system appears to be moderate, given that our 2D simulations were able to correctly reproduce the global ionisation structure of the wind, as confirmed by the good consistency of the simulated spectra with observations, despite the richness and high statistical quality of the observational data. On the other hand, our initial experiments showed that these effects are escaping the 1D ionisation simulations which grossly fail in explaining the observed spectrum of LIN 358. Our calculations presented here are a significant improvement on the earlier 1D calculations and we have achieved consistent results at a significantly lower cost compared to what would be required for 3D simulations.

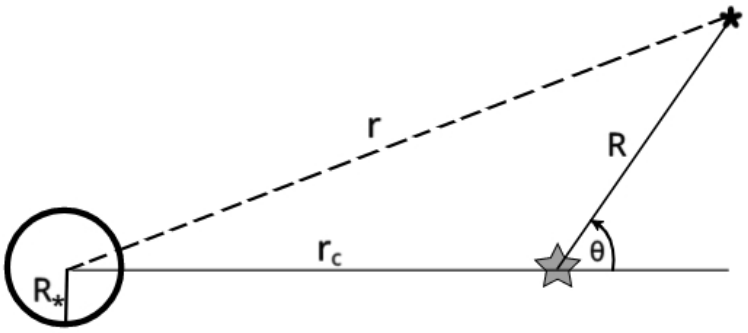

Figure 3.4: The geometrical configuration of our simulations. The giant star and the centre of the spherically symmetric density distribution is marked with the black open circle. The white dwarf is marked with the grey star at the distance r_c from the density centre. A test particle at distance r from the centre of the density distribution will have coordinates (R, θ) in the WD-centred reference system.

We assume the mass-loss to be of the form

$$\dot{M} = 4\,\pi\,\mu\,m_{\rm H}\,v\,r^2\,n(r)\,\left(1 - \frac{R_*}{r}\right), \tag{3.3}$$

where μ is the mean molecular weight, $m_{\rm H}$ is the mass of a hydrogen atom, $v = 15$ km s^{-1} is the assumed constant wind velocity (Chen et al. 2017), $R_* = 178$ R$_\odot$ is the origin of the stellar wind, i.e. the radius of the giant star, r is the distance from the centre of the giant star, and $n(r)$ is the number density at distance r. The main consequence of Eq. (3.3) is that the wind density structure follows a power-law (r^{-2}) distribution when $r \gg R_*$, but at the surface of the giant star the density becomes very high. We set the maximum density to $n = 10^{14}$ cm^{-3} to avoid the infinite density at $r = R_*$. With this wind structure the ionising source is sitting off-centre at a distance r_c, but the density distribution from the white dwarfs point of view can easily be calculated following Arthur (2007). First, we can write the density distribution in a form:

$$n(r) = n_c\,\left(\frac{r}{r_c}\right)^{-2}\,\left(1 - \frac{R_*}{r}\right)^{-1}, \tag{3.4}$$

where n_c is the number density at the distance r_c, i.e. at the position of the WD. We can now change the coordinates and centre the reference system to the position of the WD so that we can write

$$r^2 = R^2 + r_c^2 - 2Rr_c\cos(\pi - \theta)\,, \tag{3.5}$$

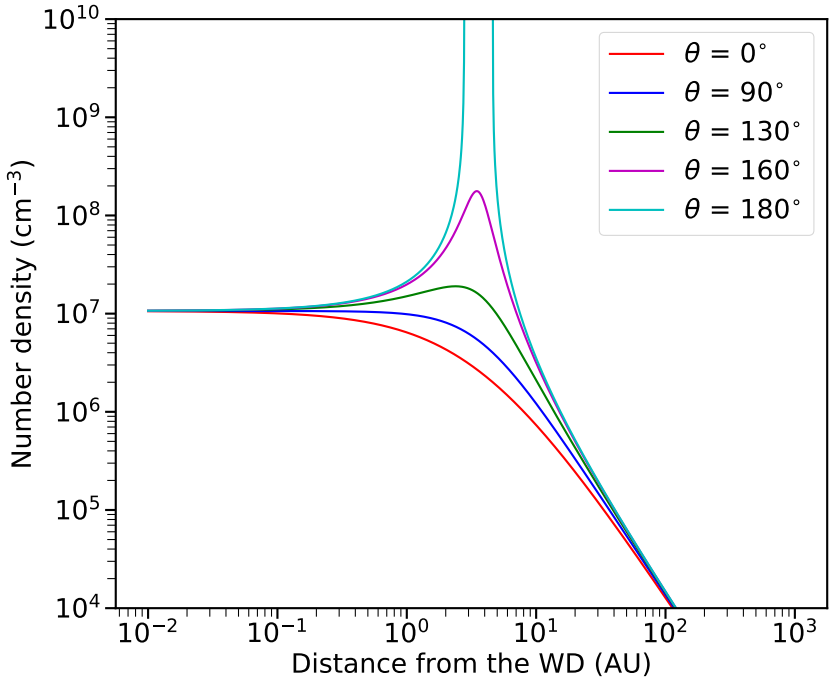

Figure 3.5: The density distribution as seen by the WD with $n_c = 10^7$ cm^{-3} and $r_c = 3.7$ AU calculated for various angles.

where R is the distance measured from the WD to the direction of θ, where the angle θ is measured from the symmetry axis between the WD and the giant star, and the giant star is in the direction $\theta = \pi$; see Fig. 3.4. Combining equations (3.4) and (3.5), we can write the density distribution from the white dwarfs point of view as

$$n(R,\theta) = \frac{n_c\, r_c^2}{R^2 + r_c^2 + 2Rr_c\cos\theta}\left(1 - \frac{R_*}{R^2 + r_c^2 + 2Rr_c\cos\theta}\right)^{-1}. \tag{3.6}$$

With Eq. (3.6) we can calculate the density distribution along any line of sight, which is illustrated in Fig. 3.5 with $n_c = 10^7$ cm^{-3} and $r_c = 3.7$ AU.

3.6 Results

Using the setup explained in Sec. 3.5 we performed simulations to see if we can reproduce the observed characteristics of the LIN 358 by varying the main parameters of the problem: temperature T_h and luminosity L of the WD and the mass-loss rate $\dot{M}_{\rm loss}$ of the donor star. Strictly speaking, the WD luminosity is not an independent parameter. It is determined by the mass accretion rate modulo the regimes of the nuclear burning on the WD surface, whereas for the given binary system parameters, the mass accretion rate depends on the

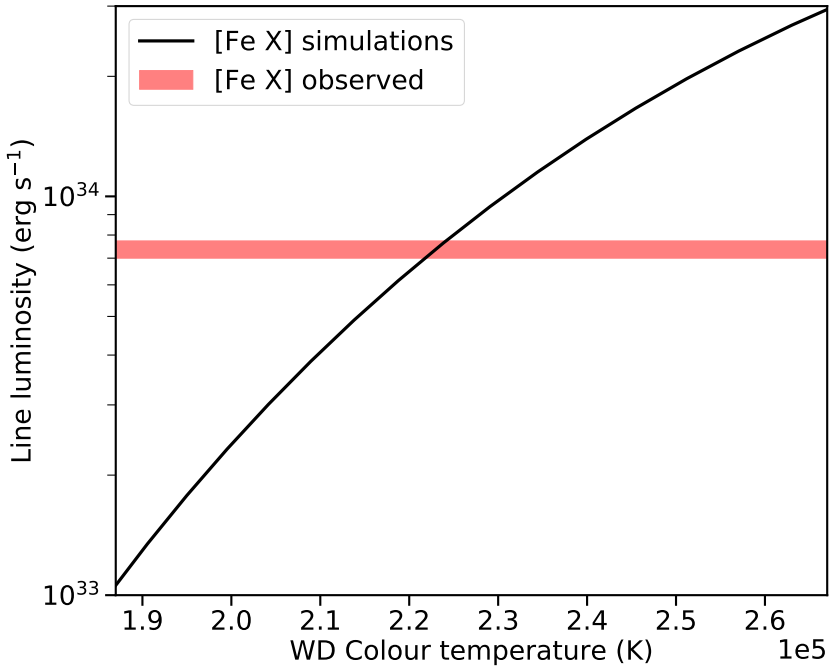

Figure 3.6: Simulated [Fe X] 6374 Å luminosity as a function of the WD blackbody temperature calculated with $L = 10^{38}$ erg s^{-1} and $\dot{M}_{\rm loss} = 1.2 \times 10^{-6}$ M$_\odot$ yr^{-1}.

mass loss rate of the donor star. On the other hand, line luminosities scale with the gas density which in turn is proportional to the mass loss rate. Due to the non-linear nature of the problem, we varied $\dot{M}_{\rm loss}$, L and T_h in an ad hoc iterative procedure to reach the values that best described the observed properties of LIN 358. In this procedure, we considered only the high excitation lines of He II 4686 and [Fe X] 6374 Å for which the line luminosities are robustly predicted in our simulations. As, in the relevant parameter range, the line luminosities are monotonic functions of temperature, WD luminosity and the donor mass-loss rate, the so found solution would be unique. Other significantly detected lines were used for an a posteriori consistency check.

3.6.1 Colour temperature of the white dwarf

First, we determined the temperature of the ionising source by matching the observed [Fe X] 6374 Å emission line to the simulations. As mentioned in Sec. 3.4.4, this emission line is produced close to the white dwarf and is very sensitive to the temperature of ionizing radiation but insensitive to the structure of the stellar wind at large distances from the white dwarf (see also Fig. 3.8). The simulations and the comparison to the observed line luminosity is shown in Fig. 3.6. In this figure, the WD luminosity and the wind mass loss rate are fixed at the values, determined in the above mentioned iterative procedure. From

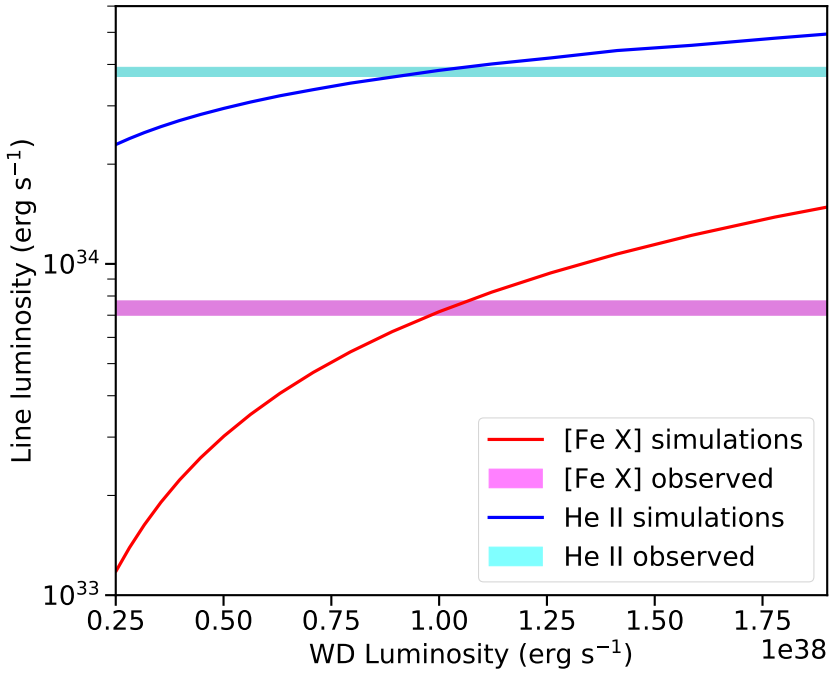

Figure 3.7: Simulated [Fe X] 6374 Å (red) and He II 4686 Å (blue) line luminosity as a function of the WD luminosity for $T = 19$ eV and $\dot{M}_{\rm loss} = 1.2 \times 10^{-6}$ M$_\odot$ yr^{-1}.

this plot we can derive for the temperature:

$$T_h \; = \; (\, 2.22 \pm 0.03 \,) \; \times \; 10^5 \text{ K} \;\; \approx \; 19 \text{ eV}, \tag{3.7}$$

where the error correspond to the statistical error of the [Fe X] 6374 Å line luminosity. The so obtained value of the WD colour temperature is close to the temperatures $T_h = (2.275 \pm 0.3) \times 10^5$ K and $T_h = (2.50 \pm 0.1) \times 10^5$ K derived previously by Kahabka & Haberl (2006) and Skopal (2015), respectively. In addition, this temperature is in agreement with the simple formula of Iijima (1981) used to estimate the effective temperature of a central source from the nebular emission line fluxes:

$$T(10^4 K) = 19.38 \sqrt{\frac{2.22 F_{4686}}{4.16 F_{H\beta} + 9.94 F_{4471}}} + 5.13, \tag{3.8}$$

where F_{4686}, $F_{H\beta}$, and F_{4471} are the fluxes of He II 4686, H β, and He I 4471 emission lines, respectively. Using this formula for LIN 358, we get $T_{\rm eff} = 2.36 \times 10^5$ K. In all of the following calculations we have used the temperature derived from the [Fe X] 6374 Å emission line in Eq. (3.7).

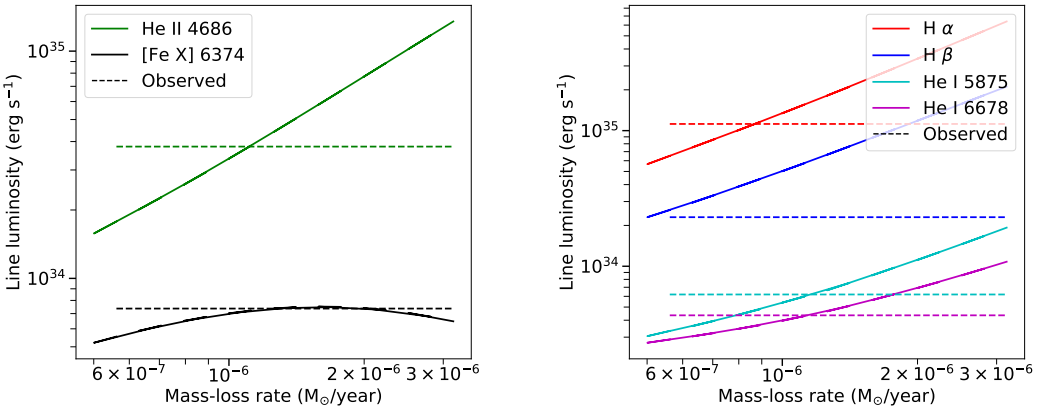

Figure 3.8: The observed and simulated line luminosities for main emission lines in the spectrum of LIN 358 shown as a function of the mass-loss rate of the giant star. In the left panel we show the high excitation lines of He II 4686 and [Fe X] 6374 Å which luminosities are robustly predicted in our simulations. In the right panel we show the Hα, Hβ, He I 5875, and He I 6678 Å lines which are more sensitive to the collisional effects, self-absorption and detail of the wind structure near the donor star. The solid lines are predicted by the CLOUDY simulations and the dashed horizontal lines show the observed values from Table 3.1. The mass-loss rate on the x-axis is from the Eq. (3.3) with $v = 15$ km s^{-1}, $r = 3.7$ AU, and $R_* = 178$ R$_\odot$.

3.6.2 White dwarf luminosity

To justify the choice of the WD luminosity we used the two high-excitation lines [Fe X] 6374 Å and He II 4686 Å. The comparison between simulations and observations is shown in Fig. 3.7, demonstrating that the two lines give consistent estimates of the WD luminosity. From this we can derive the WD luminosity:

$$L = (1.02 \pm 0.15) \times 10^{38} \text{ erg s}^{-1}. \tag{3.9}$$

This value is consistent with the previous values of Kahabka & Haberl (2006) and Skopal (2015).

3.6.3 Mass-loss rate of the donor star

The density structure of the wind is related to the mass-loss rate from the donor star via Eq. (3.3) with $v = 15$ km s^{-1}, $r = 3.7$ AU, and $R_* = 178$ R$_\odot$. Simulated and observed line luminosities of the two high excitation lines of He II 4686 and [Fe X] 6374 Å are shown in the left panel of Fig. 3.8. From this figure one can see that the luminosities of our two main diagnostic lines can be explained with a consistent mass-loss rate of

$$\dot{M}_{\text{loss}} \approx 1.2 \times 10^{-6} \text{ M}_\odot \text{ yr}^{-1}$$

The right hand panel in Fig. 3.8 shows luminosities of other principal emission lines. As one can see from this plot, the He I lines are consistent with the high excitation lines, but the Balmer lines show some scatter in mass-loss rate values, which however is not dramatic and its origin is reasonably well understood, as discussed in Sec. 3.7.

3.6.4 Structure of the emission regions of principal lines

With our simulations we can investigate where the majority of the nebular emission in a symbiotic binary originates. This is illustrated in the top two panels in Fig. 3.9, where we show the volume emissivity of several emission lines. The emissivity is shown in an arbitrary plane, because we have assumed an azimuthal symmetry. From these figures one can see that the emissivity distribution for low excitation lines is quite asymmetric along the line connecting the white dwarf and the donor star. Indeed, in the simple Strömgren sphere case, the radius of the ionized region in a constant density nebula containing only hydrogen is:

$$\mathrm{R_S} = \left(\frac{3}{4\pi}\frac{\dot{\mathrm{N}}_{\mathrm{ph}}}{\mathrm{n}^2\alpha}\right)^{\frac{1}{3}} \approx 155\mathrm{AU}\left(\frac{\dot{\mathrm{N}}_{\mathrm{ph}}}{10^{48}\mathrm{s}^{-1}}\right)^{\frac{1}{3}}\left(\frac{\mathrm{n}}{10^{7}\mathrm{cm}^{-3}}\right)^{-\frac{2}{3}}, \tag{3.10}$$

where α is the recombination coefficient, $\dot{\mathrm{N}}_{\mathrm{ph}}$ is the number of ionizing photons per second, and n is the number density of the ISM. The lower density away from the giant star (i.e. increasing x-coordinate in Fig. 3.9) causes the ionized region to be more extended in this direction than towards the giant star. The dark cone to the left is the "shadow" of the giant star, which blocks the emission from the WD propagating to the left.

From the Fig. 3.9 one can see that most of the emission originates from the vicinity of the giant star, where the density is higher. This is further illustrated by Fig. 3.10 where we show the simulated line luminosity as a function of the angle θ (see Fig. 3.4) for various emission lines. These figures also highlight the differences between different lines: the [Fe X] 6374 Å line originates roughly spherically from the immediate surroundings of the ionizing source, as already mentioned in Sec. 3.4.4, whereas virtually all of the He I emission comes from a small region near the giant star, where the gas is not too highly ionized and the density is high enough that the collisional processes dominate the emission mechanisms. The emissivity as a function of the distance from the ionising source for several angles is shown in Fig. 3.11. Also in this figure one can clearly see the same differences in the emission lines: the [Fe X] 6374 Å emissivity peaks much to the WD than the H and He I lines, which all peak roughly at the same distance close to the giant star. For He I lines the emissivity peak is very sharp near the donor star, while for the others the emissivity is more extended.

3.7 Discussion

We have used 2D radiative transfer calculations based on the CLOUDY photoionization code to study ionization of the wind from the AGB donor star by the emission from the nuclear

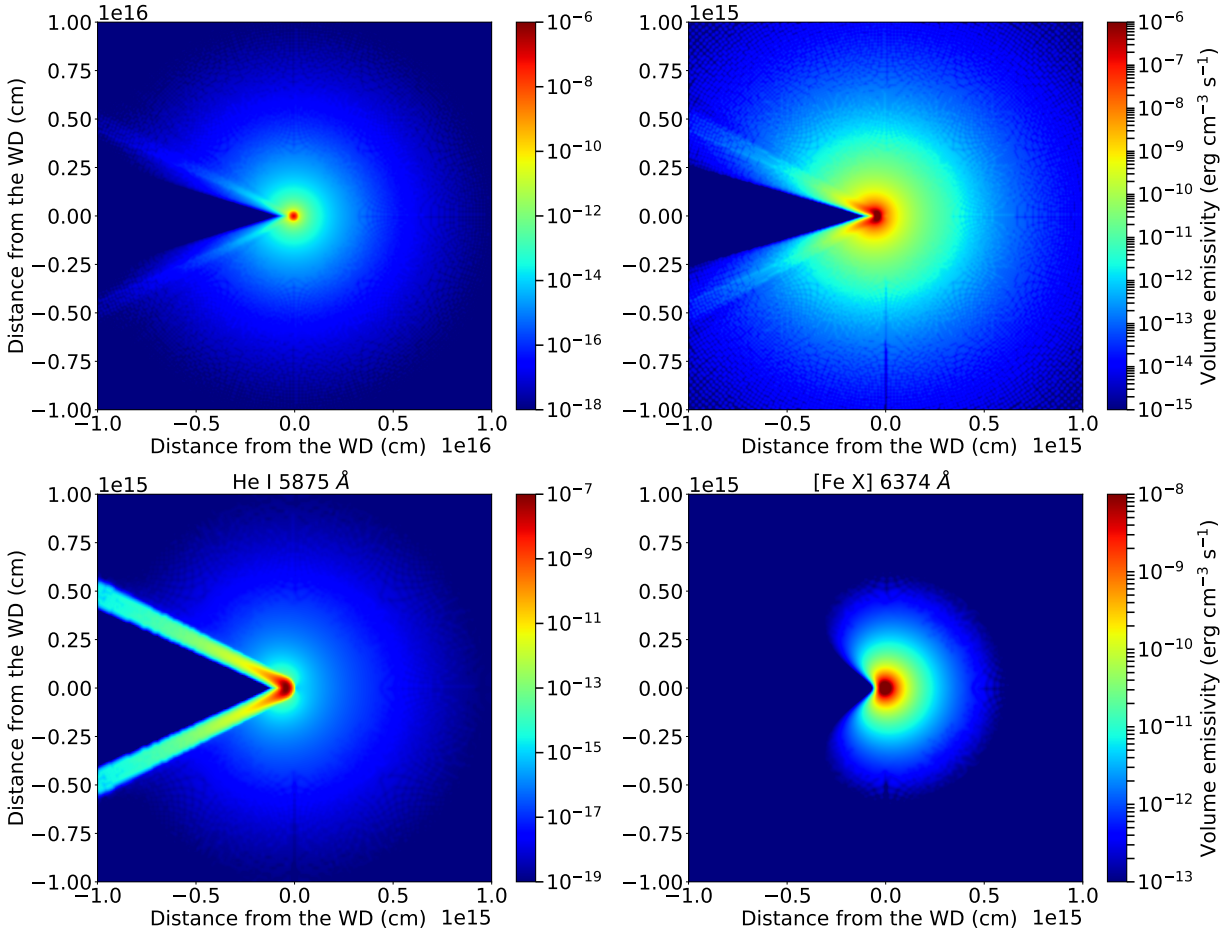

Figure 3.9: Structure of the emission region in our best-fitting simulation (L = 10^{38} erg s^{-1} and $\dot{M}_{\rm loss} = 1.2 \times 10^{-6}$ M$_\odot$ yr^{-1}) for different emission lines. The top row shows emissivity of Hα line with two different length scales of 10^{16} cm (left) and 10^{15} cm (right). The lower panels show emissivity of He I on the left and of [Fe X] 6374 Å on the right at the length scale of 10^{15} cm. The colours represent the line volume emissivity in erg s^{-1} cm^{-3} according to the colour-bars. In this representation the WD is located at the centre of the image at coordinates (0, 0) and the donor star is to the left of the WD at a distance of 3.7 AU (5.5×10^{13} cm).

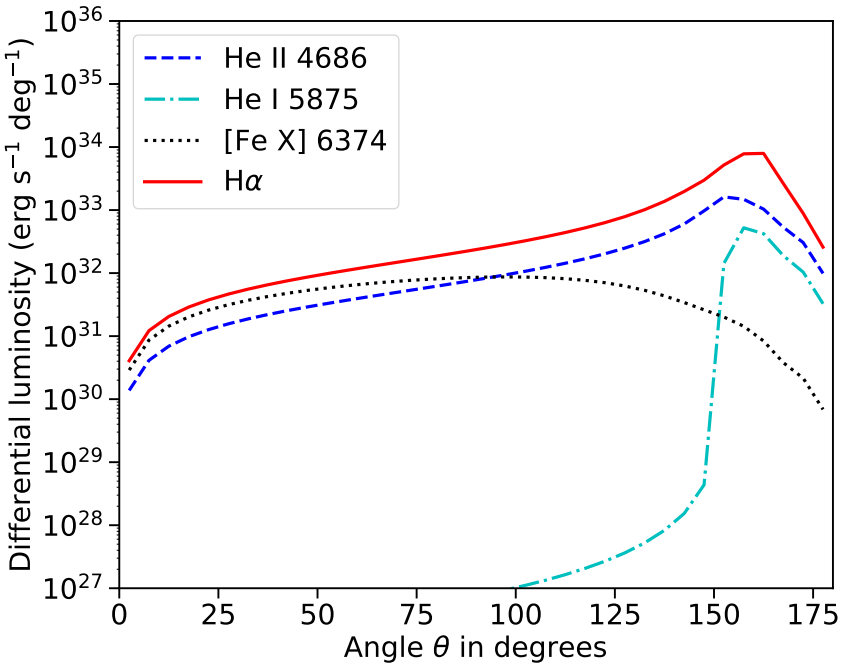

Figure 3.10: Distribution of line luminosity around the white dwarf as a function of angle θ (see Fig. 3.4). The lines are calculated for L = 10^{38} erg s^{-1} and $\dot{M}_{\rm loss} = 1.2 \times 10^{-6}$ M$_\odot$ yr^{-1}.

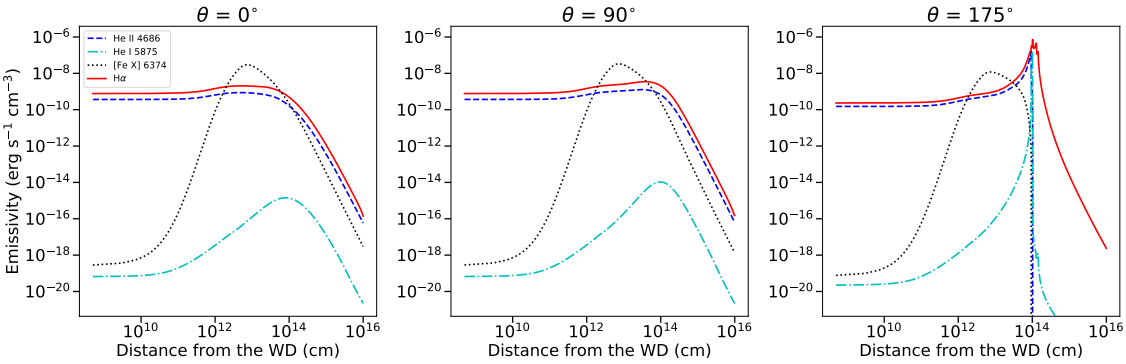

Figure 3.11: The emissivity of various emission lines shown as a function of the distance from the ionising source with three different angles (see Fig. 3.4): $\theta = 0°$ (left), $\theta = 90°$ (middle), and $\theta = 175°$ (right). The lines are calculated for L = 10^{38} erg s^{-1} and $\dot{M}_{\rm loss} = 1.2 \times 10^{-6}$ M$_\odot$ yr^{-1}.

burning white dwarf in the LIN 358 system. As discussed in Sec. 3.5, the real geometry of the wind in symbiotic binaries is not spherically symmetric and strictly speaking requires 3D simulations. However, our 2D simulations do capture correctly the main geometrical aspects of the photoionization nebula around the white dwarf – significant asymmetry of the density distribution towards the donor star, away from it and in the direction normal to the orbital plane of the system. With this, our simulations successfully explain all the main emission lines except for the Balmer lines, which are modified by self-absorption and have complicated line profiles. Our approach enabled us to significantly improve on the 1D calculations (which in our runs failed to explain the observed spectrum) while also keeping the computational effort manageable. Based on our calculations we provide a self-consistent description of the observed optical spectrum and derived the main parameters of the problem – wind mass loss rate of the AGB donor star, luminosity of the white dwarf and the colour temperature of its emission.

The orbital parameters of LIN 358 are not known whereas the orbital separation of the system is an important parameter in our calculations. To this end, we used estimates based on numerical modelling and an analytical description of the wind Roche Lobe overflow accretion regime, as described in Sec. 3.2.2. As these estimates bear some uncertainty we investigated the dependence of our results on the assumed binary separation a and found that they are relatively insensitive to a in the relevant range of values of a. In particular, we have found that increasing a by a factor of two increases the derived mass-accretion rate by only $\sim$20%, and the temperature and luminosity change by $\sim$2%. Similarly, decreasing the binary separation to 2 AU on the other hand decreases the mass accretion rate by $\sim$15%.

3.7.1 Low excitation lines

Although absolute luminosities of Hα and Hβ lines can be roughly accounted in our simulations (Fig. 3.8) their observed line ratio is not reproduced. The line ratio in our simulations remains constant at ≈ 3, as expected from the Case B recombination (Osterbrock & Ferland 2006), but the observed line ratio is higher, Hα/H$\beta \approx 4.9$. This higher Balmer decrement could have been caused by ISM dust absorption, but this is unlikely, given the small value of interstellar reddening towards the source (see Sec. 3.3). The most likely reason for the high Balmer decrement is self-absorption, which is not fully captured by our simple simulation setup. High Hα/Hβ line ratios have been previously observed in e.g. AGN and other symbiotic binaries, and our observed value can be explained by e.g. the calculations done by Netzer (1975), but the complicated high density structure near the surface of the giant star and inside the wind acceleration radius, where the collisional effects play a major role in the production of Balmer lines, cannot be fully described by our simple simulation setup. The wind structure is likely more complicated than a smooth power-law profile and there can be clumps, inhomogeneities, and shock waves. In addition, the wind can be gravitationally focused towards the orbital plane of the binary (de Val-Borro et al. 2009; Shagatova et al. 2016), and simulating this would require full 3D calculations.

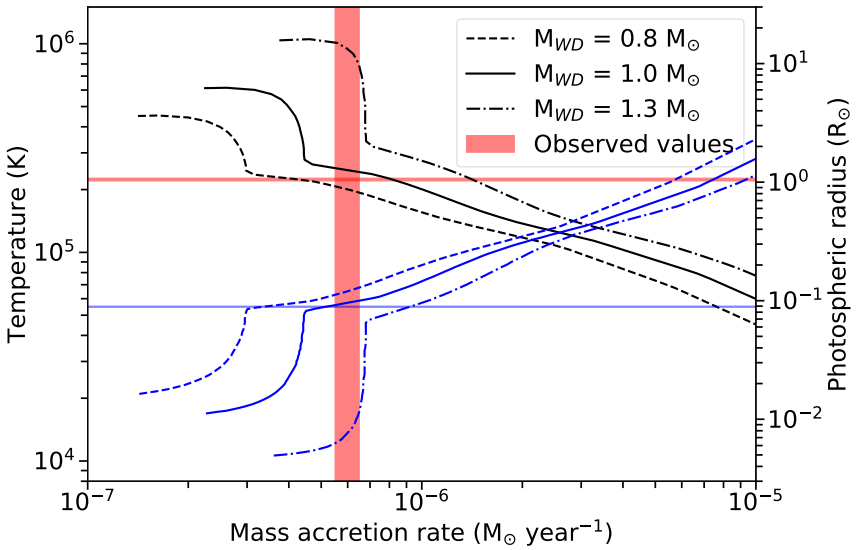

Figure 3.12: The photospheric temperature (black lines) and radius (blue lines) of the white dwarf shown as a function of the mass-accretion rate. The dashed, solid, and dash-dotted lines show the results of Hachisu et al. (1999) for WD masses of 0.8, 1.0, and 1.3 $M_\odot$, respectively. The red areas show our results for LIN 358, and the blue horizontal line shows the photospheric WD radius derived by Skopal (2015).

3.7.2 Mass accretion rate

Steady nuclear burning on the white dwarf surface can occur only in a rather narrow range of mass-accretion rates, below which the WD exhibits nova outbursts, and above which the WD is believed to have an expanded photosphere and lose the excess mass via high velocity winds (Hachisu et al. 1996; Nomoto et al. 2007; Wolf et al. 2013).

Our results suggest that the giant star in the LIN 358 system is losing mass through stellar winds with a mass-loss rate of $\dot{M}_{\rm loss} \approx 1.2 \times 10^{-6}$ $M_\odot$ yr^{-1}. This value is well within the range of typical mass-loss rates for O-rich AGB stars like LIN 358 (Ramstedt et al. 2009; Groenewegen & Sloan 2018). How much of this material ends up on the WD is not fully clear, but using the same method as described by e.g. Abate et al. (2018); Iłkiewicz et al. (2019); Belloni et al. (2020) we can estimate the accretion efficiency to be ≈ 0.5 which means the WD would accrete material at rate $\dot{M}_{\rm acc} \approx 6 \times 10^{-7}$ $M_\odot$ yr^{-1}. Recalling that for a 1 $M_\odot$ white dwarf stable nuclear fusion can occur in the range of mass accretion rates from $\approx 2 \times 10^{-7}$ $M_\odot$ yr^{-1} to $\approx 4 \times 10^{-7}$ $M_\odot$ yr^{-1} (Nomoto et al. 2007; Wolf et al. 2013), we conclude that the white dwarf in LIN 358 accretes above the stability strip. In this regime, only a fraction of accreted material can be retained, the maximal rate given by the upper boundary of the stability strip, $\approx 4 \times 10^{-7}$ $M_\odot$ yr^{-1} for a 1 $M_\odot$ white dwarf, the rest being blown away in a radiation driven wind (Hachisu et al. 1996; Nomoto et al. 2007; Wolf et al. 2013). The high velocity WD wind will further complicate the geometry of the photoionization problem. Interestingly, the upper boundary of the stability strip,

$\dot{M} = 4 \times 10^{-7}$ M$_\odot$ yr^{-1}, corresponds to the bolometric luminosity of $L = 1.1 \times 10^{38}$ erg s^{-1}, which is very close to the luminosity of the white dwarf derived in our photoionisation calculations, $L = (1.02 \pm 0.15) \times 10^{38}$ erg s^{-1}. We emphasise that this value of WD bolometric luminosity was obtained in Sec. 3.6 on completely different grounds.

Conversely, we can use bolometric luminosity of the WD derived from photoionisation calculations to constrain the accretion efficiency in LIN358. Indeed, given the efficiency of the nuclear burning and assuming solar abundances, a luminosity of 1.02×10^{38} erg s^{-1} requires the mass accretion rate of $\dot{M} = 3.7 \times 10^{-7}$ M$_\odot$ yr^{-1}. Given the mass-loss rate of $\dot{M}_{\rm loss} \approx 1.2 \times 10^{-6}$ M$_\odot$ yr^{-1} in LIN 358, the accretion efficiency is 0.31. Taking into account that the bolometric luminosity is close to the upper boundary of the stability strip for 1 M$_\odot$ WD, this value should be considered as a lower limit. We also note that if LIN 358 harbours a more massive white dwarf as suggested e.g. in Orio et al. (2007), the conclusion that the WD is accreting above the stable nuclear burning limit would not change as the value of $\dot{M} = 3.7 \times 10^{-7}$ M$_\odot$ yr^{-1}, corresponding to the luminosity of 1.02×10^{38} erg s^{-1}, exceeds the lower boundary of the stability strip for any WD mass up to about 1.3 M$_\odot$. On the other hand, we argue that the mass of the WD in LIN358 is larger than 0.9 M$_\odot$ as for smaller masses the luminosity of 10^{38} erg s^{-1} could not be maintained for extended period.

Furthermore, we use the wind solution from Hachisu et al. (1999) to plot in Fig. 3.12 the photospheric temperature and radius of an accreting WD as a function of the mass-accretion rate. In this plot we also show our best fit WD colour temperature, our estimate of the mass accretion rate and the WD photospheric radius measurement from Skopal (2015). As one can see, the lines cross between the 0.8 and 1 $M_\odot$ curves derived from Hachisu et al. (1999) calculations.

Conversely, we can use bolometric luminosity of the WD derived from photoionisation calculations to constrain the accretion efficiency in LIN358. Indeed, given the efficiency of the nuclear burning and assuming solar abundances, a luminosity of 10^{38} erg s^{-1} requires the mass accretion rate of $\dot{M} = 3.5 \times 10^{-7}$ M$_\odot$ yr^{-1}. Given the mass-loss rate of $\dot{M}_{\rm loss} \approx 1.2 \times 10^{-6}$ M$_\odot$ yr^{-1} in LIN 358, the accretion efficiency is ≈ 0.3. Taking into account that the bolometric luminosity is close to the upper boundary of the stability strip for 1 M$_\odot$ WD, this value should be considered as a lower limit. We also note that if LIN 358 harbours a more massive white dwarf as suggested e.g. in Orio et al. (2007), the conclusion that the WD is accreting above the stable nuclear burning limit would not change as the value of $\dot{M} = 3.5 \times 10^{-7}$ M$_\odot$ yr^{-1} corresponding to the luminosity of 10^{38} erg s^{-1} exceeds the lower boundary of the stability strip for any WD mass up to about 1.3 M$_\odot$. On the other hand, we argue that the mass of the WD in LIN358 is larger than 0.9 M$_\odot$ as for smaller masses the luminosity of 10^{38} erg s^{-1} could not be maintained for extended period.

Notably, any high velocity winds ($\sim$ 100's – 1000 km s^{-1}) driven from the WD, as is predicted for accretion rates above the stable accretion regime (Hachisu et al. 1999), should prove strongly supersonic within the red giant wind medium. This would produce a strong shock, in a manner analogous to the colliding winds found in some high-mass binaries (e.g., Dougherty et al. 2005). Detecting such emission in LIN 358 should be feasible; indeed, shock emission from colliding winds has previously been detected in a massive binary in

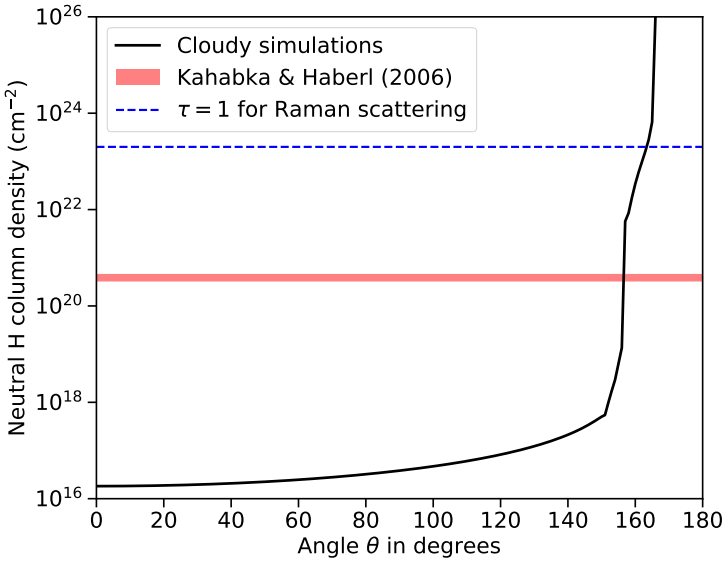

Figure 3.13: The neutral hydrogen column density around the WD as a function of the angle θ (see Fig. 3.4) calculated for L = 10^{38} erg s^{-1} and $\dot{M}_{\rm loss} = 1.2 \times 10^{-6}$ M$_\odot$ yr^{-1}. The black line shows the simulation results, red line shows the upper limit from Kahabka & Haberl (2006, see text), and the blue dashed line shows the column density at which the optical depth for Raman scattering equals unity (see Sec. 3.4.5).

the SMC (Nazé et al. 2007). Modelling the additional emission expected from such a shock is, however, beyond the present scope; we address this, as well as prospects for constraining WD accretion physics, in a subsequent effort.

3.7.3 Circumstellar absorption

X-ray spectral fitting of LIN 358 gave the column density of neutral material intrinsic to SMC of $(3.9 \pm 0.6) \times 10^{20}$ cm^2 (on top of Galactic absorption of 3.7×10^{20} cm^2) (Kahabka & Haberl 2006). This number includes contributions from the neutral ISM in the SMC as well as the neutral circumstellar material (CSM) around LIN 358. In a more general context, attenuation by the dense wind from the giant star is often proposed to explain the paucity of observed symbiotic binaries. However, in many cases the wind should be too highly ionized to provide significant level of attenuation (Nielsen & Gilfanov 2015).

Our calculations show that this is also true for LIN 358, where the circumstellar material is mostly ionized except for a narrow cone towards the donor star. We show in Fig. 3.13 the neutral hydrogen column density N$_{\rm H}$ obtained from our simulations as a function of the viewing angle from the WD. From this figure one can see that the wind is highly ionized everywhere except angles $\Theta \gtrsim 150^\circ$ where a large amount of neutral gas is present with column densities in excess of N$_{\rm H} \gtrsim 10^{22}$ cm^{-2}. However, the solid angle subtended by the regions of large column density is only about ~ 0.07 of 4π. Therefore, even if the binary inclination angle is sufficiently small, large N$_{\rm H}$ values will only be observed in the narrow

range of binary orbital phase, when the donor star is close to the line of sight.

We thus conclude that in the case of LIN 358, the circumstellar material can not provide any notable attenuation of the white dwarf emission, and that the excess absorption (above the Galactic value) observed in the X-ray spectrum of the source is due to the ISM in the SMC. Given the low colour temperature of LIN 358, even a modest amount of absorption by the neutral gas in the Milky Way and SMC is sufficient to attenuate its emission by a large factor.

Although in LIN 358 the white dwarf emission freely escapes the surrounding CSM, we did not detect any extended ($\gtrsim$ 1 pc) ionized nebula around the source. Super-soft X-ray sources are expected to ionize the surrounding ISM and create a distinct H II region around them (Rappaport et al. 1994; Remillard et al. 1995; Woods & Gilfanov 2016). The expected presence of such ionized nebulae around accreting WDs has been used to constrain their accretion history and their role in producing Type Ia supernovae (Woods & Gilfanov 2016; Woods et al. 2017, 2018; Graur & Woods 2019; Kuuttila et al. 2019; Farias et al. 2020), but the ambient ISM density around LIN 358 appears to be too low for a nebula to be detectable.

3.7.4 LIN 358 in the context of the origin of SN Ia

Our results suggest that the white dwarf in LIN 358 is growing in mass with a rate of $\approx 4 \times 10^{-7}$ M$_\odot$ yr^{-1}. For this reason LIN 358 and symbiotic systems in general have been considered as prospective SN Ia progenitors (see Maoz et al. 2014, for a review). One of the well known problems of this scenario, limiting the possible contribution of symbiotic systems to SN Ia production, is the short lifetime of an AGB star, of the order of $\sim 10^5$ years (Yungelson & Livio 1998). Indeed, even a WD accreting above the steady burning limit and growing its mass at the maximum rate, similar to LIN 358, would gain only ~ 0.04 M$_\odot$ in the course of the symbiotic phase. The WD would have to be initially very massive in order to reach the Chandrasekhar mass, but such massive WDs are thought to be formed as ONeMg-rich WDs, which are thought to rather form a neutron star via AIC instead of exploding (Nomoto 1984; Nomoto & Kondo 1991). The explosion and collapse mechanisms are however not yet fully understood and recent simulations show that ONeMg-rich WDs can explode (see e.g. Marquardt et al. 2015; Jones et al. 2016, 2019). Nevertheless, symbiotic binaries are thought of as possible progenitor candidates for some peculiar SNe Ia, especially those exhibiting signatures of interaction with hydrogen-rich circumstellar material (SNe Ia-CSM; e.g. SN 2002ic Hamuy et al. 2003). These supernovae exhibit strong early time Hα emission, consistent with the supernova ejecta interacting with dense circumstellar material (Silverman et al. 2013a). In addition, SNe Ia-CSM show large Hα/ Hβ ratios (e.g. > 7 for PTF11kx; Silverman et al. 2013b) caused by collisional excitation and Balmer self-absorption in a high density gas, similar to LIN 358 and many other symbiotic binaries.

While an AIC is a more likely outcome of a symbiotic binary than a SN Ia (Yungelson 2010), given that the highest mass WDs formed are ONeMg-rich, the formation of neutron stars via AIC from AGB+WD binaries faces the same issue as SNe Ia progenitors, which is

the short lifetime of the AGB star. The number of AIC progenitors with an AGB donor in the Galaxy has recently been estimated to be ~ 30 by Ruiter et al. (2019), who assumed a BHL wind description and a time-averaged accretion rate of $\sim 10^{-8}$ $M_\odot$ yr^{-1}. However, as shown here, the accretion rate can be much higher than that, meaning that the AGB+WD binaries like LIN 358 can form neutron stars more efficiently.

As mentioned above, however, symbiotic binaries can be difficult to detect, especially in X-rays, while in other wavelengths they can be difficult to separate from other astrophysical sources. For example, in the infrared the symbiotic binaries are dominated by emission from the AGB star and thus they can be difficult if not impossible to separate from e.g. single AGB stars. The best wavelength range to unambiguously detect symbiotic binaries may be the optical spectrum, because symbiotic binaries like LIN 358 are often very bright in the He II 4686 Å emission line, which is a clear signature of an accreting white dwarf. This line, together with some possible high excitation state forbidden lines such as [Fe X] 6374 Å, can be used to identify possible symbiotic candidates, but perhaps the most important identifiers are the Raman scattered O VI features at 6830 Å and 7088 Å. These features are observed almost exclusively in symbiotic binaries, and in the Milky Way the presence of the Raman scattered lines is confirmed in about 55% of the symbiotic population; in the SMC the percentage is 92% (Akras et al. 2019a). Future surveys focusing on these Raman features, like the RAMSES II search (Angeloni et al. 2019), can shed more light on the true population of symbiotic binaries and therefore provide some constraints on the birthrates of SNe Ia and AICs from the symbiotic channel.

3.8 Conclusions

We have examined the properties of the SMC symbiotic binary LIN 358 by comparing our optical spectroscopic observations with 2D radiative transfer simulations performed with the help of the CLOUDY photoionization code. Comparing the results of our simulations and observations, we have determined the colour temperature of the WD to be $T = (2.23 \pm 0.03) \times 10^5$ K, its bolometric luminosity of $L = (1.02 \pm 0.15) \times 10^{38}$ erg s^{-1}, and the mass-loss rate of the donor star to be $\dot{M}_{\rm loss} = 1.2 \times 10^{-6}$ $M_\odot$ yr^{-1}. Assuming a solar H to He ratio in the wind material, a lower limit to the accreted mass fraction in LIN358 is 0.31 We also determined the accretion rate on to the white dwarf to be $\dot{M}_{\rm acc} \approx 6 \times 10^{-7}$ $M_\odot$ yr^{-1}. These results indicate that the WD in LIN 358 is accreting material at a rate above the stability strip of hydrogen fusion and may be loosing a fraction of the accreted mass via a high velocity wind. At these high accretion rates the photosphere of the white dwarf expands to a fraction of the solar radius, thus explaining the low colour temperature of the white dwarf emission. We speculate that many symbiotic systems may be operating in this regime, which explains the paucity of detected systems. For the mass of ≈ 1 $M_\odot$, the white dwarf in LIN 358 is growing its mass at the maximum possible rate of $\approx 4 \times 10^{-7}$ $M_\odot$ yr^{-1}. It is however unlikely that the white dwarf in LIN 358 will ever reach the Chandrasekhar limit due to the short lifetime of the AGB donor star. Our calculations show that the circumstellar material in LIN 358 is nearly completely ionized everywhere except for a

narrow cone around the donor star with an opening angle of 30 degrees, and the radiation of the white dwarf freely escapes from the system. The low energy absorption detected in the X-ray spectrum of this system is due to neutral ISM in the Milky Way and in the SMC.

Chapter 4

Observational properties of symbiotic binaries

To be submitted to Monthly Notices of Royal Astronomical Society

Abstract Symbiotic stars are long-period interacting binaries and they represent important astrophysical laboratories to study the various stages of stellar evolution, binary interaction and accretion processes. Thus far a considerably smaller number of symbiotic binaries have been detected than what is predicted. In addition the observational appearances between different binaries vary considerably and many source can be confused with e.g. planetary nebulae. In this paper we study the observational properties of symbiotic binaries, mostly in terms of optical emission lines. We use the plasma simulation and spectral synthesis code CLOUDY to perform 2D photoionization simulations of a white dwarf (WD) that is ionizing the dense wind of a giant donor star. We treat the system in a self-consistent manner where most relevant parameters, e.g. temperature and luminosity of the WD, are not treated as free parameters but calculated from the binary properties. With this method we can solve for the ionization and emission structure of the circumstellar medium (CSM) around the WD and thus predict the luminosity of various emission lines. We compare the predicted emission line ratios to the diagnostic diagrams used to distinguish symbiotic binaries from other sources and show how the mass-accretion rate of the WD affects these diagrams. In addition, our calculations show that the CSM around majority of the symbiotic binaries is nearly fully ionized, except for the "shadow" behind the donor star.

4.1 Introduction

Symbiotic binaries are interacting binaries consisting of an evolved giant donor star and a compact object, typically a white dwarf (WD) but also a neutron star. The compact object is often accreting gas efficiently from the wind of the donor star, which heats up the accretor to high ($\gtrsim 10^5$ K) temperatures. Symbiotic binaries are thus often characterised by emission lines from high ionization states, for example He II, O VI, and Fe X, in addition to many bright lower ionization state lines such as H Balmer lines. Symbiotic binaries are also characterised by a complex circumstellar environment resulting from the hot ionizing compact object embedded in the dense neutral wind of the donor star. For a recent review of symbiotic binaries see Mikołajewska (2012); Munari (2019).

The radii of the red giants are in the order of astronomical units, so also the orbital separations in symbiotic binaries are measured in AUs. Consequently, the orbital periods of (S-type) symbiotic binaries range mostly from 1 to 6 years (Gromadzki et al. 2013), while some Mira type variables (D-type) have longer periods, up to tens of years (e.g. Gromadzki & Mikołajewska 2009). Thus measuring the periods of symbiotic binaries can be a difficult task, which is made even more difficult by the variable nature of these binaries. Instead of long monitoring programs, some insight into the symbiotic binaries can be gained from the optical spectrum of the system. Especially some high ionization state lines, for example [Fe X], are very sensitive to binary properties and thus detecting and measuring these lines can provide vital information of the symbiotic binaries quite easily.

So far only ~ 300 symbiotic binaries are known in the Milky Way (Akras et al. 2019a; Merc et al. 2019), which is much lower than predicted by the simulations, which range from a few thousand up to 4×10^5 (Magrini et al. 2003; Lü et al. 2006; Yungelson 2010). The reason is not fully clear, but the possible explanations include significant absorption by circumstellar and interstellar medium, and the confusion with other similar sources. Especially symbiotic binaries have been mistaken for planetary nebulae and dense H II regions (Belczyński et al. 2000), while confusion with Be stars and young stellar objects is also notable (Corradi et al. 2008; Rodríguez-Flores et al. 2014). So far the most reliable features to identify the symbiotic binaries are the Raman scattered O VI features at $\lambda\lambda$6830 and 7088 ÅÅ, which are almost exclusively observed in the symbiotic binaries. However, these features are present only in 55% of the Galactic symbiotic binaries (Allen 1980; Schmid 1989; Akras et al. 2019a).

Various methods have been proposed to distinguish symbiotic binaries from planetary nebulae and other sources. Gutierrez-Moreno et al. (1995) used the [O III] and Balmer emission lines for the classification, but this method is not always applicable, because the [O III] are not always detected. Iłkiewicz & Mikołajewska (2017) explored various other emission lines including [N II], [Ne III], and He I lines, in order to distinguish planetary nebulae from symbiotic binaries. They found out that among the forbidden lines only the [O III] and [N II] lines can be used due to their high critical densities. However, there exists many symbiotic binaries with no or little forbidden line emission and thus these methods cannot be used.

Recently Kuuttila et al. (2021) studied a symbiotic binary LIN 358 with a combination

of optical spectroscopy and 2D photoionization simulations and measured e.g. the mass-loss rate from the giant donor star. Here we expand on this method and simulate the emission from a large variety of symbiotic binaries using these 2D photoionization simulations. We present grids of emission models for a large range of mass-loss rates and orbital separations and provide observational predictions for various emission lines as a function of the mass-loss rate and binary separation. In addition we investigate how these parameters affect the previously used emission line diagrams and their usage for distinguishing between symbiotic binaries and planetary nebulae.

The paper is organised as follows: in Sec. 4.2 we introduce our model and simulations, in Sec. 4.3 we present our results, and then we conclude by summarising our findings in Sec. 4.4.

4.2 Model description

4.2.1 Cloudy simulations

In order to study the emission lines of accreting symbiotic binaries, we have calculated a grid of simulations with the photoionization and spectral synthesis code CLOUDY version 17.02 (Ferland et al. 2017). The simulations were performed in a 2D configuration as introduced by Kuuttila et al. (2021). In this method the ionizing source, i.e. the white dwarf, is located at a distance r_c from the centre of the spherically symmetric density distribution, i.e. the centre of the mass-losing donor star. We assume the mass-loss to be of the form (Nussbaumer & Vogel 1987)

$$\dot{M} = 4\,\pi\,\mu\,m_{\rm H}\,v_w\,r^2\,n(r)\,\left(1-\frac{R_*}{r}\right), \tag{4.1}$$

where μ is the mean molecular weight, $m_{\rm H}$ is the mass of a hydrogen atom, $v_w = 15$ km s^{-1} is the assumed constant wind velocity, R_* is the radius of the donor star where the stellar wind is launched, r is the distance from the centre of the donor star, and $n(r)$ is the number density at distance r. The maximum number density at $r = R_*$ is set to 10^{15} cm^{-3} due to the limitations of CLOUDY (see section 3.6 in part 2 of CLOUDY documentation 'Hazy') .

Introducing an angle θ as the angle between the orbital plane and the line of sight from the WD (see Fig. 4.1), we can write the density distribution from the white dwarfs point of view as

$$n(R,\theta) = \frac{n_c\,r_c^2}{R^2+r_c^2+2Rr_c\cos\theta}\left(1-\frac{R_*}{R^2+r_c^2+2Rr_c\cos\theta}\right)^{-1}. \tag{4.2}$$

In our simulations we assumed a solar metallicity from Grevesse et al. (2010), a diffuse background radiation field was included following (Ostriker & Ikeuchi 1983; Ikeuchi & Ostriker 1986; Vedel et al. 1994) with the cosmic microwave background included, and

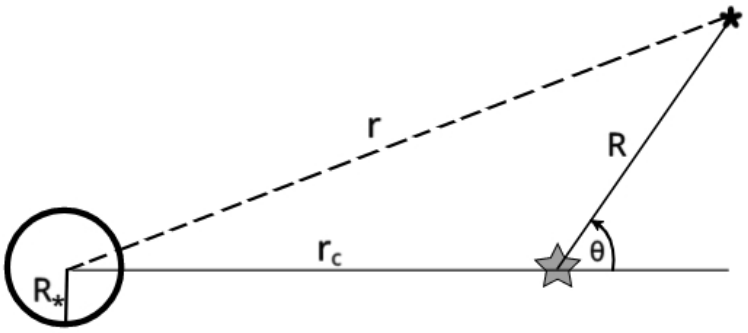

Figure 4.1: The geometrical configuration of our simulations from Kuuttila et al. (2021). The giant star and the centre of the spherically symmetric density distribution is marked with the black open circle. The white dwarf is marked with the grey star at the distance r_c from the density centre. A test particle at distance r from the centre of the density distribution will have coordinates (R, θ) in the WD-centred reference system.

the cosmic rays were included in the calculations according to the mean ionisation rate of Indriolo et al. (2007). We ignored the radiation from the donor star, because the temperature of the donor star (3000 K) is low compared to the WD's temperature ($\gtrsim 10^5$ K) and thus does not significantly contribute to the ionization of the CSM.

4.2.2 Binary parameters

Our aim is to study the emission lines of symbiotic binaries and their dependence on mass-loss rate of the donor star and the binary separation. To do this, we need to fix several other parameters of the system.

We carried out our simulations for two different WD masses: 0.6 $M_\odot$ and 1.0 $M_\odot$. The mass of the donor star was fixed to 1.0 $M_\odot$ and 1.66 $M_\odot$, respectively, so that the mass ratio $q = M_{\rm WD}/M_{\rm donor}$ was fixed to 0.6. This was done because the wind Roche lobe overflow formalism of Abate et al. (2013) is based on hydrodynamical simulations (Mohamed & Podsiadlowski 2012), where $q = 0.6$ was fixed. Abate et al. (2013) introduced a $\propto q^2$ scaling to the accretion efficiency formula (see Eq. (4.4)) based on the scaling in the Bondi-Hoyle-Lyttleton formalism, but as the validity of this scaling has not been verified, we focus only on the original $q = 0.6$. For both masses we assumed the donor star temperature to be 3000 K and the radius to be 200 $R_\odot$, while also assuming the dust in the donor star to be carbon rich (see Eq. (4.5)).

We varied the mass-loss rate from the donor star from 10^{-8} to 10^{-5} $M_\odot$, which corresponds to the typical mass-loss rates from AGB stars (Höfner & Olofsson 2018). The

orbital separation between the donor star and the WD was varied 2 to 14 au (period from 2.2 to 37 years). One should note that for separations $\lesssim 2$ AU the Roche lobe radius of the donor approaches the radius of the star and the accretion transitions to the traditional Roche lobe overflow. For 2 AU separation the Roche lobe size of the donor is 182 $R_\odot$, which is already smaller than the assumed donor size (200 $R_\odot$). Our simulations focus on the wind accretion regime and do not cover the Roche lobe overflow mechanism.

4.2.3 Accretion rate

Given the mass-loss rate from the donor star, we calculate the mass-accretion rate on the WD using the same method as in Abate et al. (2013). In this method the accretion rate is calculated with both the standard Bondi-Hoyle-Lyttleton (BHL) formalism (Hoyle & Lyttleton 1939; Bondi & Hoyle 1944) and the wind Roche lobe overflow (WRLOF) formalism (Mohamed & Podsiadlowski 2007, 2012), and the higher of the two is chosen. The maximum accretion rate is set to 50% of the mass-loss rate.

The accretion efficiency in the BHL formalism is given by (Boffin & Jorissen 1988):

$$\beta_{\rm BHL} = \frac{\alpha}{2\sqrt{1-e^2}} \left(\frac{G\,M_{\rm WD}}{r_{\rm c}\,v_{\rm w}^2} \right)^2 \left[1 + \left(\frac{v_{\rm orb}}{v_{\rm w}} \right)^2 \right]^{-3/2}, \tag{4.3}$$

where $\alpha = 1.5$ is a constant, e is the eccentricity (assumed zero), and $v_{\rm orb}$ is the orbital velocity. The accretion efficiency in the WROLF formalism is given by (Abate et al. 2013):

$$\beta_{\rm WRLOF} = \frac{25}{9}\,q^2 \left[-0.284 \left(\frac{R_{\rm d}}{R_{\rm L}} \right)^2 + 0.918 \frac{R_{\rm d}}{R_{\rm L}} - 0.234 \right], \tag{4.4}$$

where $q = M_{\rm WD}/M_{\rm donor}$ is the mass ratio, $R_{\rm d}$ is the dust formation radius, and $R_{\rm L}$ is the Roche lobe radius of the donor star (Eggleton 1983). The dust formation radius can be calculated by (Höfner 2007):

$$R_{\rm d} = \frac{1}{2} R_* \left(\frac{T_{\rm d}}{T_{\rm eff}} \right)^{-\frac{4+p}{2}}, \tag{4.5}$$

where R_* is the radius of the donor star, $T_{\rm d}$ is the dust condensation temperature, $T_{\rm eff}$ is the temperature of the donor star, and p is a parameter characterising the opacity of the dust. For amorphous carbon dust grains $T_{\rm d} = 1500$ K and $p = 1$ (Höfner 2007).

In each of our simulations, for a given mass-loss rate and binary separation, we calculated the mass-accretion rate with the equations (4.3) and (4.4) and chose the higher value, i.e.

$$\dot{M}_{\rm acc} = \max\left\{ \beta_{\rm BHL}(r_c), \beta_{\rm WRLOF}(r_c) \right\} \times \dot{M}_{\rm loss}. \tag{4.6}$$

4.2.4 Luminosity and temperature of the WD

Instead of treating the temperature and luminosity of the WD as free parameters, we calculated them directly from the mass-accretion rate and other parameters. The calculations were done in two different ways, depending on whether the accretion rate was above the steady nuclear burning limit or below.

If the accretion rate is high enough to sustain steady nuclear burning of hydrogen, we determined the colour temperature and the photospheric radius of the WD based on the calculations of Hachisu et al. (1999, see Figs. 3 and 4), for a given WD mass and accretion rate. The spectrum of the WD was assumed to be black-body, so the luminosity was then calculated with Stefan-Boltzmann law.

For lower accretion rates the total luminosity was assumed to be the accretion luminosity:

$$L_{\rm acc} = \frac{GM_{\rm WD}\dot{M}}{R_{\rm WD}}. \tag{4.7}$$

Half of this luminosity was assumed to be radiated by a geometrically thin and optically thick accretion disk (Shakura & Sunyaev 1973) with a multi-colour black-body spectrum (Mitsuda et al. 1984). The maximum temperature of the disk is $T_{\rm max} = 0.488\,T_*$, where

$$T_* = \left(\frac{3GM_{\rm WD}\dot{M}}{8\pi R_{\rm WD}^3\sigma_{\rm SB}}\right)^{1/4}, \tag{4.8}$$

where $R_{\rm WD}$ is the radius of the WD and $\sigma_{\rm SB}$ is the Stefan-Boltzmann constant.

The other half of the accretion luminosity was assumed to be radiated by a boundary layer (BL). For WDs with high accretion rates ($\gtrsim 10^{16}$ g s^{-1}; Pringle & Savonije 1979; Popham & Narayan 1995), the BL is optically thick with temperatures of 10^{5-6} K, while for lower accretion rates the BL is optically thin with temperatures up to 10^8 K (Pringle 1977; Popham & Narayan 1995; Suleimanov et al. 2014). We have focused only on the high accretion rate regime, so we have assumed a BL emitting a black body spectrum with temperature of (Frank et al. 2002)

$$T_{\rm BL} = T_*\left(\frac{3GM_{\rm WD}\mu m_{\rm H}}{8kR_{\rm WD}T_*}\right)^{1/8}, \tag{4.9}$$

where μ is the mean molecular weight and k is the Boltzmann constant. This simple formula is in agreement with the theoretical BL simulations of Hertfelder et al. (2013); Suleimanov et al. (2014).

In Fig. 4.2 we show the temperature and the luminosity of the WD as a function of the mass-loss rate from the donor star (upper panel) and the orbital separation (lower panel). The mass of the WD in this figure is set to 0.6 M$_\odot$.

We note that this method ignores the thermal stability of the WD. Accreting WDs with accretion rates below the steady nuclear burning limit ($\lesssim 10^{-7}$ M$_\odot$ yr^{-1}) exhibit explosive nuclear burning, i.e novas, at certain intervals depending on the accretion rate (Wolf et al.

2013). The nova eruptions will significantly affect the emission and structure of the CSM, but studying these novae is outside the scope of this paper and will be addressed in a future work.

4.3 Results

Using our model described in Sec. 4.2, we can calculate self-consistently the two dimensional temperature, ionization and emission structure of the CSM around symbiotic binaries. With this method we can study the emission originating from this system and how the mass-loss rate from the donor star and the orbital separation of the binary affect this emission.

4.3.1 Column density of the CSM

The emission from symbiotic binaries is often thought to be heavily obscured by the dense neutral wind from the donor star. In fact, the X-ray emission is often observed to be heavily absorbed, but this is mostly due to the low colour temperature of the WD and efficient ISM absorption (Nielsen & Gilfanov 2015). With our simulations we can show that the CSM in symbiotic binaries is in fact mostly ionized (see also Kuuttila et al. 2021).

For each simulation, we have calculated the neutral hydrogen column density N_H along each line of sight from the WD, i.e. as a function of θ (see Fig. 4.1). These results are illustrated in Fig. 4.3, where we show the fraction of the full solid angle 4π around the WD with the column density of neutral hydrogen $\mathrm{N_H} > 10^{20}$ cm^{-2}, minus the solid angle occupied by the donor star, i.e.:

$$f = \frac{\Omega_{\mathrm{N_H}>10^{20}} - \Omega_{\mathrm{donor}}}{4\pi}, \tag{4.10}$$

as a function of the orbital separation and mass-loss rate from the donor. This figure illustrates the fraction of the sky, from the WD's point of view, where the wind is mostly ionized and thus transparent. For the observer this illustrates the probability of observing the WD with a large amount of absorption by neutral hydrogen in the CSM.

From this figure one can see that the gas around the WD is mostly ionized in large set of the parameter space. The CSM becomes mostly neutral, or is at least obscuring, for very high mass-loss rates $\sim 10^{-5}$ M$_\odot$ yr^{-1} and high mass-loss rates and large separations, when the steady nuclear burning has not started and the accretion luminosity is insufficient in ionizing the dense wind. In addition, for separation of 2 AU below the burning limit the wind is mostly neutral due to the WD's proximity to the donor star.

4.3.2 Line emission

The main observable of symbiotic binaries is the luminosity of various important emission lines. Symbiotic binaries and other accreting WDs are often bright in H Balmer lines, He

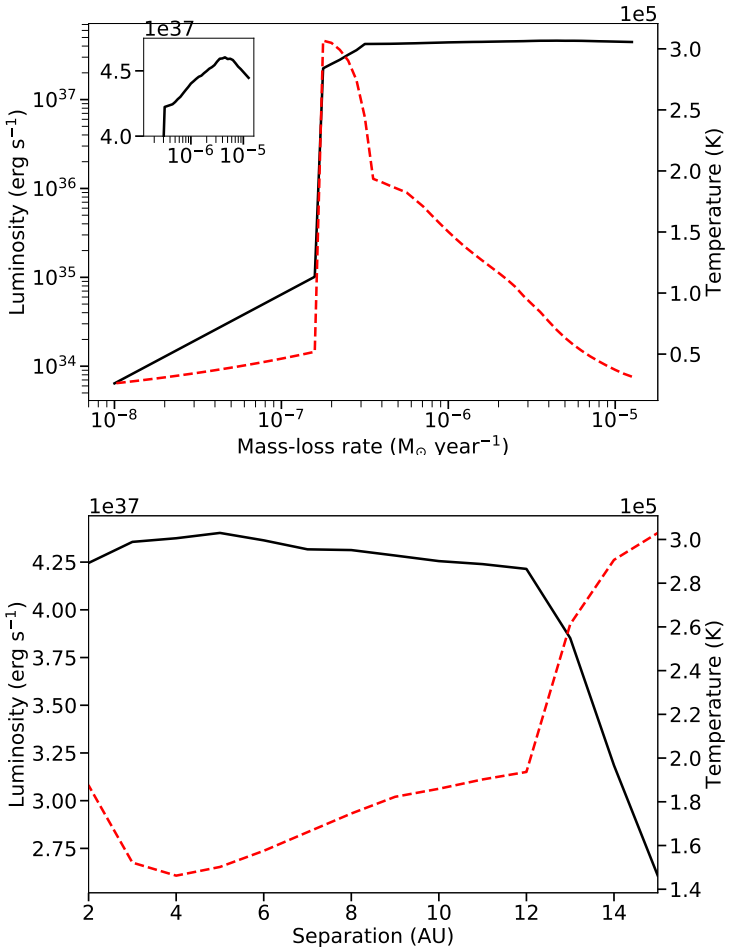

Figure 4.2: *Upper panel:* The luminosity and temperature of the WD as a function of the mass-loss rate from the donor star with constant separation of 5 AU. The y-axis on the left shows the luminosity in erg s^{-1} (black line) in logarithmic scale, and the y-axis on the right shows the temperature in K (red dashed line) in linear scale. The insert on the top left shows the luminosity in linear scale in the high mass-loss regime. The sharp rise in both temperature and luminosity at $\sim 2 \times 10^{-7}$ M$_\odot$ yr^{-1} is because of the onset of the nuclear burning on the WD.
Lower panel: The luminosity and temperature of the WD as a function of separation with a constant mass-loss rate of 10^{-6} M$_\odot$ yr^{-1}. The y-axis on the left shows the luminosity (black line) in linear scale, and the y-axis on the right shows the temperature (red dashed line) in linear scale. For low mass-loss rates with no steady burning the temperature shown is the maximum temperature of the accretion disk.

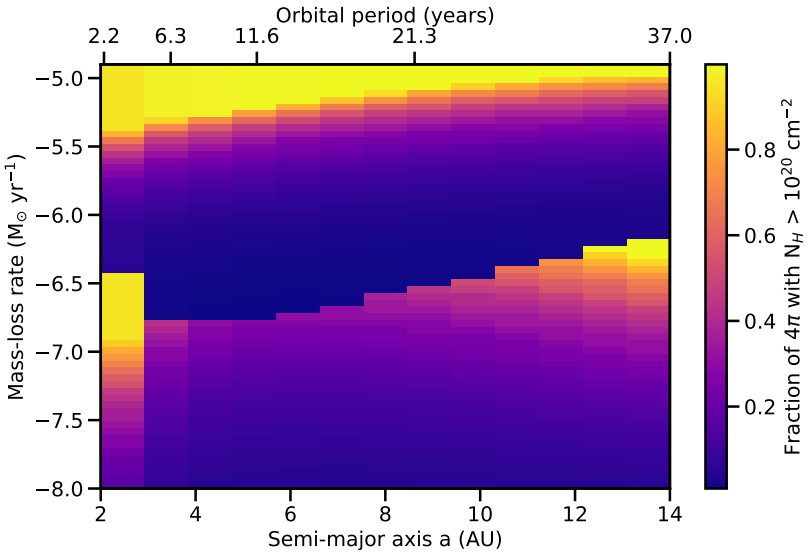

Figure 4.3: The neutral fraction of the CSM around the WD. The x-axis shows the orbital separation at the bottom and the Keplerian orbital period on top, and the y-axis shows the mass-loss rate from the donor star. The colour in this figure illustrates the fraction of the solid angle, where $N_H > 10^{20}$ cm^{-2}, minus the fraction of the sky covered by the donor star. The jump between 10^{-7} and $10^{-6.5}$ M$_\odot$ yr^{-1} is caused by the onset of steady nuclear burning on the WD.

II 4686Å, and various emission lines. Notably, high ionization state iron lines, e.g. [Fe X] 6374Å, have also been often been observed in symbiotic binaries. We have studied how this emission depends on the mass-loss rate of the donor star and the orbital separation between the two components of the binary.

From our simulations we get the volume emissivity of each line, which is then integrated over the simulated volume to get the total line luminosity, as also explained in Kuuttila et al. (2021). In Fig. 4.4 we show the line luminosity for four different emission lines: Hα, He II 4686, [O III] 5007, and [Fe X] 6374 Å, as a function of the mass-loss rate and the orbital separation. The onset of nuclear burning can be seen as jump in the line luminosities between 10^{-7} and $10^{-6.5}$ M$_\odot$ yr^{-1}.

From Fig. 4.4 one can see that the Hα emission increases monotonically with the mass-loss rate with little dependence on the orbital separation. The situation is almost the same for He II 4686Å, except for the decreasing emission at very high mass-loss rates, when the photosphere of the WD is inflated and the colour temperature decreasing.

For [O III] 5007Å the emission first increases with the increasing mass-loss rate, but then decreases sharply at the onset of nuclear burning, when the CSM becomes too highly ionized (see Sec. 4.3.2). Then the emission increases again with increasing mass-loss rates until the density becomes very high. For [Fe X] 6374 Å the emission is sharply peaked at the peak of the steady nuclear burning. Without nuclear burning the WD is not hot and luminous enough to produce appreciable amounts of [Fe X] emission, and with high mass-

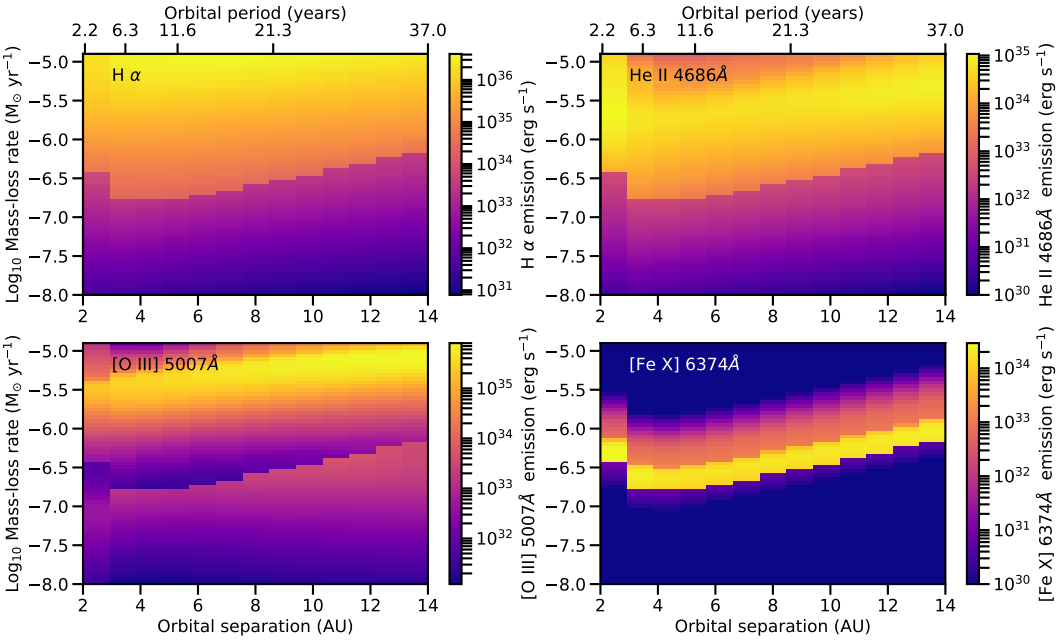

Figure 4.4: The line luminosity (in erg s^{-1}) for four different emission lines as predicted by the CLOUDY simulations. The x-axis shows the orbital separation r_c in AUs and the Keplerian orbital period in years for a WD mass 0.6 $M_\odot$. The colour shows the line luminosity for Hα (top left), He II 4686 (top right), [O III] 5007 (bottom left), and [Fe X] 6374 Å (bottom right).

loss rates ($\gtrsim 10^{-6}$ $M_\odot yr^{-1}$) the decreasing colour temperature of the WD is not enough to produce highly ionized iron. Thus [Fe X] 6374 Å emission line is a clear signature of an accreting and steadily burning WD within the stability strip.

In Fig. 4.5 we show the line emission for many different emission lines as a function of mass-loss rate for orbital separation of 3 AU, and in Fig. 4.6 we show the same lines separation of 14 AU. The lines included in these figures are: Hα, Hβ, and Hγ (top left), He I 5875, 6678 and He II 4686 Å (top right), [O III] 5007, [O I] 6300, [N II] 6583, and [S II] 6731 Å (bottom left), and [Fe VII] 6087, [Fe X] 6374, [Fe XI] 7892, and [Fe XIV] 5303 Å (bottom right).

The emission from high ionization state iron lines is strongly peaked and the shape of these curves follow closely the temperature function (see Fig. 4.2). For [Fe VII] emission there is a decrease at the same mass-loss rates where higher ionization state lines peak, because the gas is more strongly ionized.

Overall, from Figs. 4.4, 4.5, and 4.6 one can see that there is no strong dependence on the orbital separation. The behaviour as a function of mass-loss rate is nearly same for all separations, but with the peaks and jumps shifted to higher mass-loss rates due to the decreasing mass-accretion efficiency with the increasing separation.

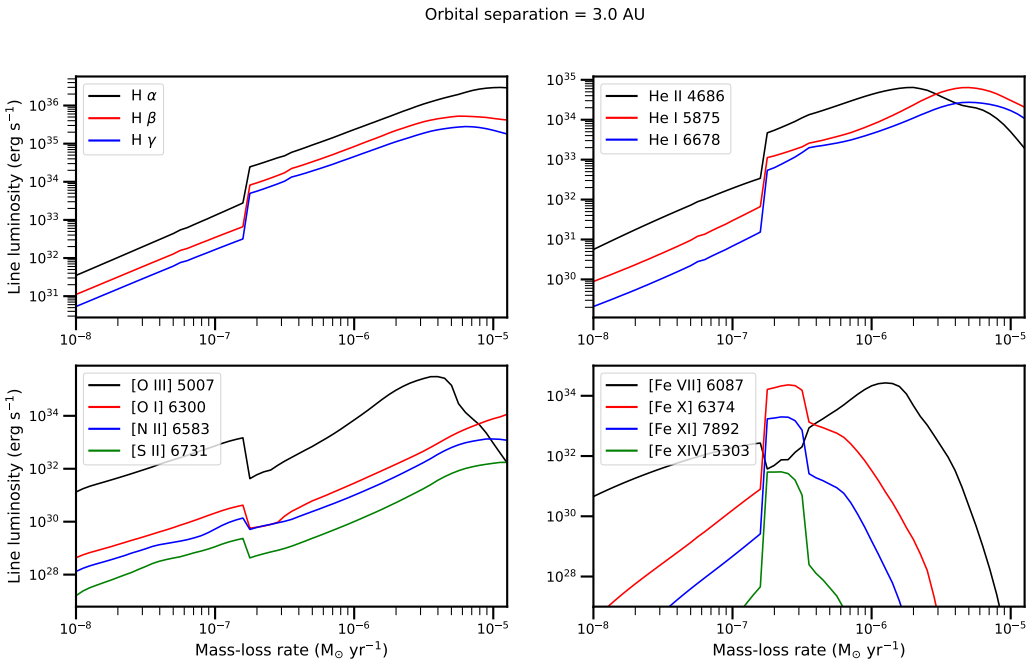

Figure 4.5: The line luminosity (in erg s^{-1}) as a function of the mass-loss rate for various emission lines. The orbital separation is set to 3 AU. The top left panel shows the line luminosity for Hα (black line), Hβ (red line), and Hγ (blue line). The top right shows the He II 4686 (black), He I 5875 (red), and He I 6678 Å lines. The bottom left shows the common forbidden [O III] 5007 (black), [O I] 6300 (red), [N II] 6583 (blue), and [S II] 6731 Å (green) emission lines. The bottom right panel shows various iron lines: [Fe VII] 6087 (black), [Fe X] 6374 (red), [Fe XI] 7892 (blue), and [Fe XIV] 5303 Å (green).

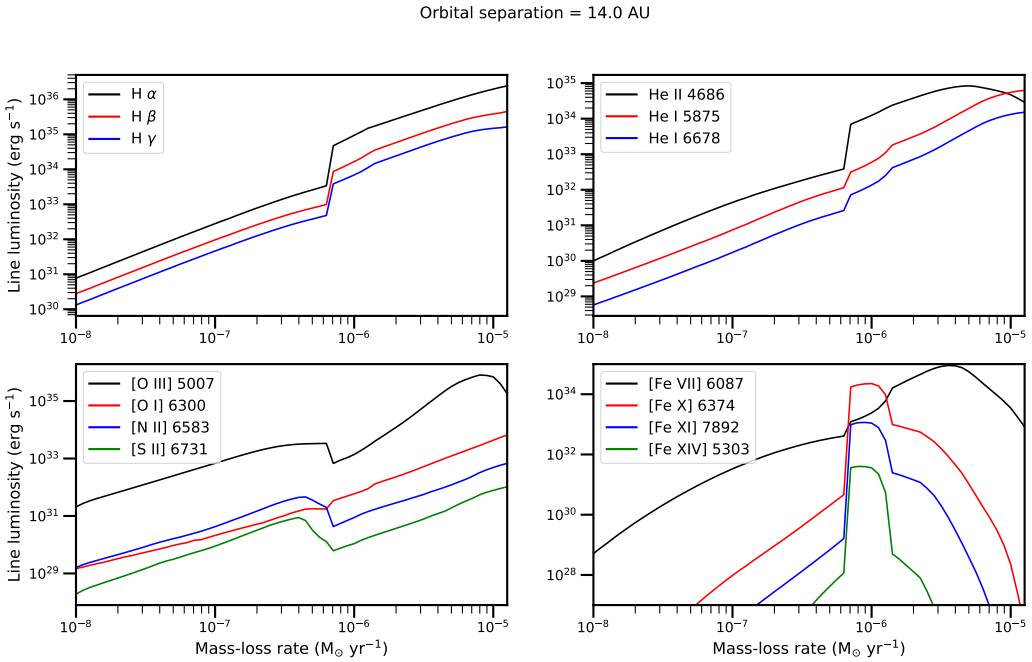

Figure 4.6: Same as Fig. 4.5 but for separation of 14 AU.

Forbidden emission lines

In some symbiotic binaries none of the common nebular forbidden emission lines are observed (e.g. LIN358; Kuuttila et al. 2021) due to the high density of the gas surrounding the WD. But as shown in Fig. 4.5, there is still a noticeable amount of e.g. [O III] 5007 emission even with high mass-loss rates, although the [O III] 5007 / Hβ ratio is small.

Interestingly, the common forbidden lines shown in Fig. 4.5 increase in brightness with increasing mass-loss rate, except at very high mass-loss rates. The sharp decrease in the line emission at about 2×10^{-7} M$_\odot$yr^{-1} is due to the increased ionization state of the gas at the onset of the nuclear burning, not due to the increased density. Thus, we can say that in many symbiotic binaries the lack of forbidden detected emission lines may be related also to the high ionization state and not only to the high density, although the density is much higher than the critical density for e.g. [O III] 5007 Å. Overall the forbidden emission is very faint, and e.g. the [O III] 5007/H β ratio is very small.

4.3.3 Line ratios

Various emission line ratios have been used in the past to characterise emission line objects and separate symbiotic binaries from e.g. planetary nebulae, Be stars and young stellar objects (e.g. Gutierrez-Moreno et al. 1995; Rodríguez-Flores et al. 2014; Iłkiewicz & Mikołajewska 2017). We have investigated how our emission models of symbiotic binaries fit to these previously presented line ratio classification diagrams and how the line ratios

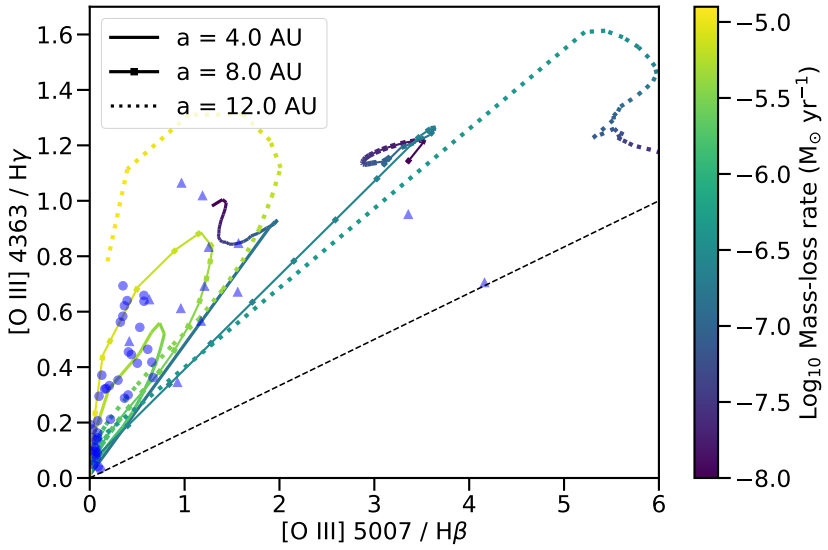

Figure 4.7: [O III] 5007/Hβ vs. [O III] 4363/Hγ line ratio diagram of Gutierrez-Moreno et al. (1995). The solid, solid-dotted, and the dotted lines show the line ratios for 4, 8, and 12 AU separations, respectively. The colour of the lines show the mass-loss rate according to the colourbar on the right. The blue circles show the S-type and the blue triangles show the D-type symbiotic binaries. The black dashed lines shows the classification criterion of Gutierrez-Moreno et al. (1995): objects above this line are classified as symbiotic binaries.

depend on the mass-loss rate and orbital separation.

In Figure 4.7 we show our models in the [OIII] diagnostic diagram of (Gutierrez-Moreno et al. 1995). In this figure is shown the [O III] 5007/Hβ vs. [O III] 4363/Hγ line ratios for three orbital separations: 4, 8, and 12 AU, while the colour of the line shows the mass-loss rate of the donor star. All three lines lines start with loss mass-loss rates from the top right part of the figure, i.e. high [O III] 5007/Hβ and [O III] 4363/Hγ ratios. With the start of the nuclear burning both of these ratios decrease close to zero and then with form a loop with increasing mass-loss rate. The behaviour with all separations is similar, but there is larger variation in the line ratios with larger separations. For comparison, we show the observed line ratios of various symbiotic binaries in this figure: the blue circles denote the S-type and the blue triangles mark the D-type binaries (Mikolajewska et al. 1997; Pereira et al. 1998; Belczyński et al. 2000; Luna & Costa 2005). All the S-type symbiotics lie in the lower left corner of this figure, with smaller separations, while the D-type binaries have larger line ratios indicating larger separations, as expected (Allen 1984; Gromadzki et al. 2013). Also shown in this figure with a black dashed line is the criteria of Gutierrez-Moreno et al. (1995) used to separate symbiotics from planetary nebulae; all our models lie above this line where the symbiotic binaries are.

In Figure 4.8 we also show two diagrams of Kniazev et al. (2008) used to distinguish

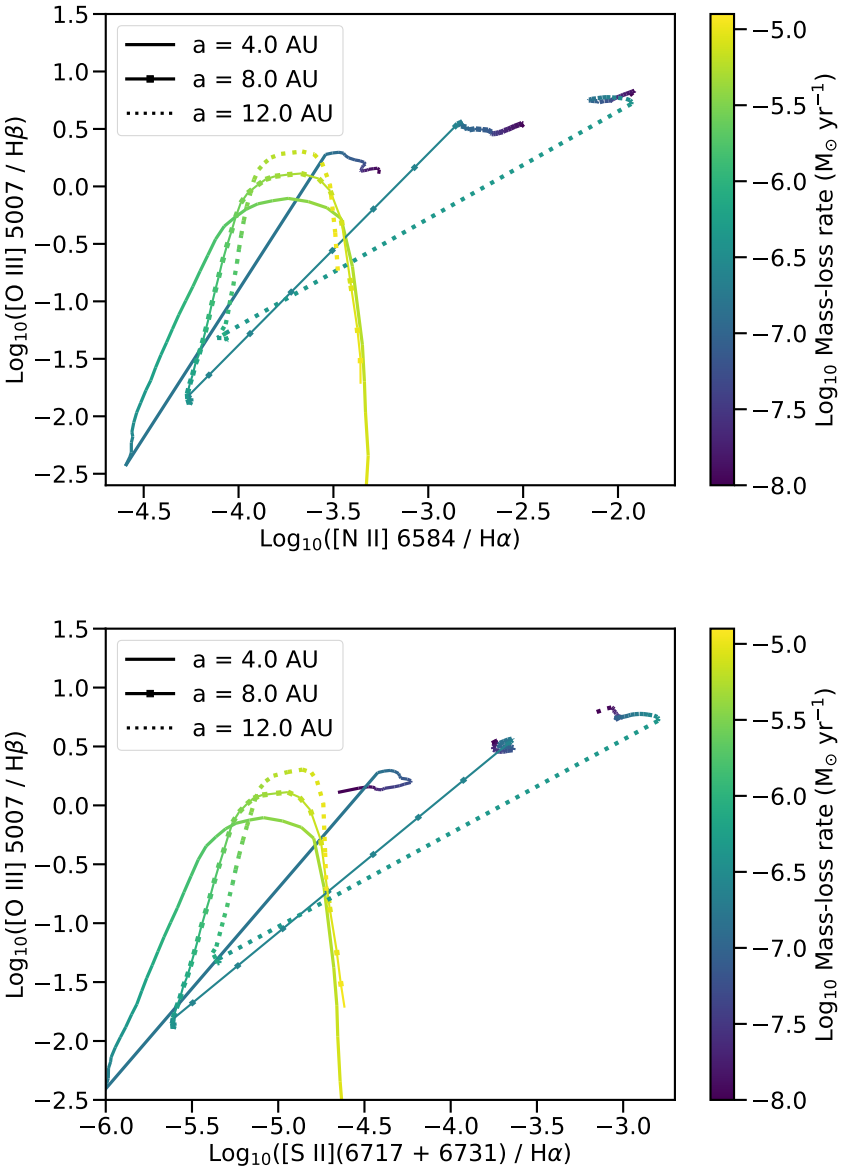

Figure 4.8: The line ratio diagrams of Kniazev et al. (2008) used to distinguish between planetary nebulae and H II regions. The top panel shows the [N II] 6583/Hα vs. [O III] 5007/Hβ ratios and the bottom panel shows the [S II] (6717+6731)/Hα vs. [O III] 5007/Hβ ratios.

between planetary nebulae and H II regions. Symbiotic binaries were not included in these diagrams originally, but due to the common confusion between the different sources, we included these diagrams as well. In Figure 4.8 is shown the [O III] 5007/Hβ ratio vs. [N II] 6583/Hα and [S II] (6717+6731)/Hα, similar to the Fig. 4.7.

Iłkiewicz & Mikołajewska (2017) studied the line ratios of many observed symbiotic binaries and planetary nebulae and proposed several new line ratio diagrams to distinguish between these two types of sources. We investigated two of the most promising diagrams in the context of our simulations. In Figure 4.9 we show the [Ne III] 3869/[O III] 4363 vs. [O III] 5007/[N II] 5755 and the [Ne III] 3869/[O III] 4363 vs. [Ne III] 3869/[O III] 5007 line ratio diagrams in a similar manner to Fig. 4.7. Here one can see that there is no strong dependence on the orbital separation. Especially in higher mass-loss rates all three separations form a similar curve in this figure. Below the steady burning limit the ratios do not change much and lie close to each other making it difficult to infer the binary parameters from these line ratios. Also included in this figure is the classification criteria of Iłkiewicz & Mikołajewska (2017). In the top panel of Fig. 4.9 the models lie in the region of symbiotics, except for the small part of the highest separation and lowest mass-loss rate model. In the bottom panel all the models lie partly outside the region of symbiotic binaries, especially for $\dot{M} > 10^{-6}$ $M_{\odot}yr^{-1}$.

All of these presented line ratio diagrams rely on the forbidden emission lines. However, there are many symbiotic binaries with few or no forbidden emission lines in the optical spectrum. For example, the only forbidden line present in LIN 358 is the [Fe X] 6374 Å line Kuuttila et al. (2021). For such sources different classification criteria are needed. One promising method is to use the He I lines, which are also bright in LIN 358. The He I lines are quite sensitive to the density of the CSM, because they are mainly collisionally excited from the meta-stable 2^3S level. Thus these lines originate from near the donor star where the density is the highest.

Similarly to Fig. 4.7, we show in Figure 4.10 the He I line ratio diagram with He I 6678/He I 5876 vs. He I 7065/He I 5876 line ratios, but this time for many different orbital separations ranging from 2 AU to 14 AU. Below the steady burning regime all the models are nearly indistinguishable, regardless of the orbital separation and mass-loss rate, and the line ratios stay close to the Case B values (e.g. He I 6678/He I 5876 ≈ 0.25). However, at higher mass-loss rates and small separations the ratios deviate significantly from the these values due to the collisional depopulation of the meta-stable 2^3S to the higher states (Bray et al. 2000; Osterbrock & Ferland 2006). With separations of 2–4 AU especially the He I 6678/He I 5876 line ratio increases significantly. For separations of $\gtrsim 7$ AU, the line ratios are nearly independent of the separation. Similar behaviour has been previously observed by Proga et al. (1994), who used these line ratios to distinguish between the long period D-type and the shorter period S-type symbiotic binaries.

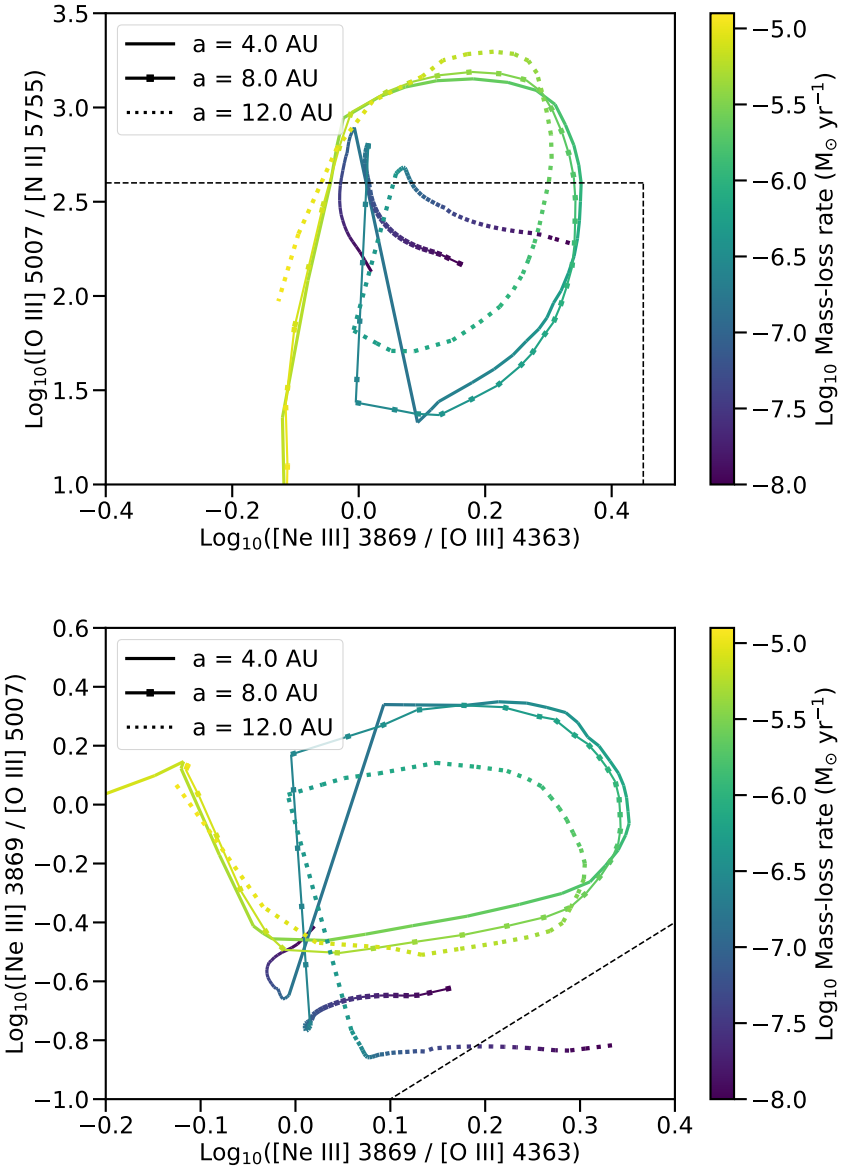

Figure 4.9: Two different line ratio diagrams of Iłkiewicz & Mikołajewska (2017). On the left is shown [Ne III] 3869/[O III] 4363 vs. [O III] 5007/[N II] 5755 and on the right is shown [Ne III] 3869/[O III] 4363 vs. [Ne III] 3869/[O III] 5007 line ratios. The solid, solid-dotted, and the dotted lines show the line ratios for 4, 8, and 12 AU separations, respectively. The colour of the lines show the mass-loss rate according to the colourbar on the right. The black dashed lines show the the criteria for symbiotic binaries proposed by Iłkiewicz & Mikołajewska (2017).

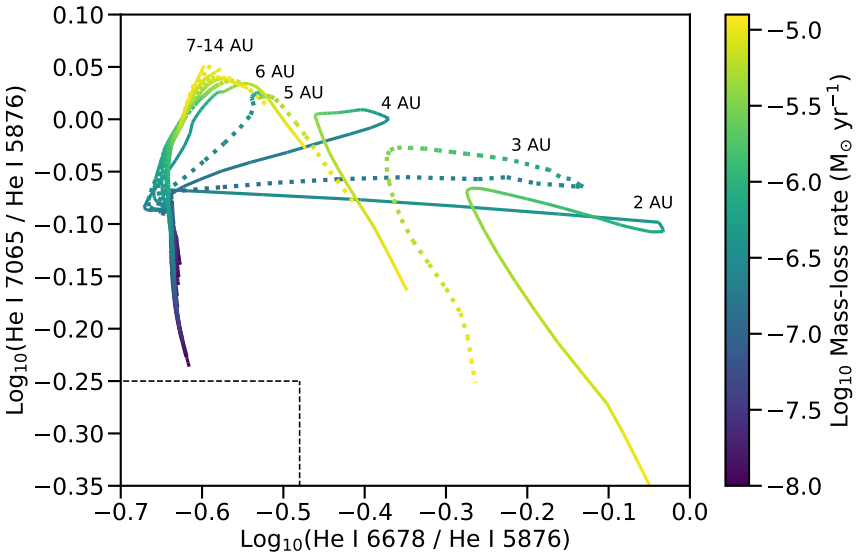

Figure 4.10: The He I line ratio diagram. The X-axis shows the He I 6678/He I 5876 line ratio and the y-axis shows the He I 7065/He I 5876 line ratio. The alternating solid and dashed lines show the line ratios calculated for various orbital separations from 2 AU to 14 AU. The colour of the lines show the mass-loss rate according to the colourbar on the right. The black dashed lines shows the classification criterion proposed by Iłkiewicz & Mikołajewska (2017): objects above and to the right of this line are classified as symbiotic binaries.

4.4 Conclusions

In this work we have studied symbiotic binaries and their observational properties with photoionization simulations. We have used a 2D simulations method to run simulations with the spectral synthesis code CLOUDY presented in Kuuttila et al. (2021). Assuming a spherically symmetric wind mass-loss and a binary separation, we calculate the mass-accretion rate, temperature, and luminosity of the white dwarf instead of treating them as free parameters. With CLOUDY we can solve the emission and ionization structure of the circumstellar medium around the white dwarf and predict e.g. the emission line strengths originating from the ionized gas.

With our simulations we show that the circumstellar medium around symbiotic binaries is mostly ionized (Fig. 4.3), especially in the steady nuclear burning regime, and thus there is no significant obscuration of the emission from the WD by the dense winds from the donor star. This is important in the context of ionized nebulae around white dwarfs (Rappaport et al. 1994), because such nebulae should then exist also around symbiotic binaries, although none have been detected up to date (Remillard et al. 1995). This is also related to the single degenerate type Ia supernova progenitor channel, wherein the progenitor is expected to create a long lasting nebula, which can be used to constrain the progenitor channels (Graur et al. 2014; Woods & Gilfanov 2016; Woods et al. 2017, 2018; Kuuttila et al. 2019; Graur & Woods 2019; Farias et al. 2020).

We have also presented emission line strength maps of several important emission lines and show how the line brightness depends on the orbital separation and mass-loss rate of the donor star (Fig. 4.4). While the behaviour of many emission lines, e.g. Balmer lines, is quite smooth, some emission lines exhibit more varied behaviour (Figs. 4.5 and 4.6). Many forbidden lines show a sharp decrease in brightness at the onset of nuclear burning on the surface of the WD, when the ionization state of the gas increases. Otherwise, while still faint, there is notable emission in the common nebular forbidden emission lines well beyond their critical densities. In addition, we have studied the various iron emission lines. Certain high ionization state iron lines, e.g. [Fe X] 6374 and [Fe XIV] 5303 Å, have been detected in many symbiotic binaries, and we show that they are an excellent indicator of the stable nuclear burning on the WD. These lines are very sensitive to the colour temperature of the WD and thus the emission peaks sharply at the stable nuclear burning regime, while other iron lines with lower ionization state, e.g. [Fe VII] 6087, decrease in brightness in the same regime (Figs. 4.5).

In addition, we have explored the various emission line ratio diagrams used to separate symbiotic binaries from other sources (e.g. Proga et al. 1994; Gutierrez-Moreno et al. 1995; Iłkiewicz & Mikołajewska 2017). There is a broad consistency between our calculations and the previously derived empirical line ratio diagrams. We have shown how the various line ratios change with the orbital separation and mass-loss rate, how this is seen in the context of S- and D-type symbiotic binaries, and how useful the certain line ratio diagrams are in separating symbiotic binaries with e.g. orbital period (Figs. 4.7, 4.8, 4.9, and 4.10). Many of these line ratios involve forbidden lines, which may be absent in many symbiotic binaries, making the usage of these diagrams difficult. Thus the most useful, and the

only one without forbidden lines, is the He I line ratio diagram (Fig. 4.10), which has been previously used to distinguish between S- and D-type symbiotic binaries (Proga et al. 1994). The helium lines are especially sensitive to the density and thus serve as a clear indicator of the distance between the WD and the donor star.

In this work we have focused on the optical emission lines in order to shed some light on the symbiotic binaries. We note, however, that for the complete picture other wavelengths should be considered in addition. For symbiotic binaries especially the infrared emission is important due to the nature of the donor star and the ease of IR observations. Recently, Akras et al. (2019b) used machine-learning approach to the 2MASS and WISE surveys to present a new approach for identifying and distinguishing symbiotic binaries from other sources (see also Akras et al. 2019a, 2021). Similar efforts focusing on multi-wavelength data in addition to specific surveys focusing on e.g. the Raman scattered features (Angeloni et al. 2019) may eventually yield more information on the paucity of observed symbiotic binaries and their contribution to e.g. type Ia supernova progenitors and formation of neutron stars via accretion induced collapse.

Chapter 5

Conclusions

In this thesis I have studied accreting and nuclear burning white dwarfs, how their emission affects the surrounding material, and how they may be connected to the Type Ia supernovae. In the classical picture the white dwarf accretes matter from a companion star and grows in mass via nuclear burning of the accreted material on its surface until it reaches the Chandrasekhar mass and explodes. This implies that the progenitor will be very luminous with typical luminosities of 10^{37-38} erg s^{-1} and effective temperatures of 10^{5-6} K making it a very efficient ionizing source. Thus these progenitors should be surrounded by large ionized regions, which will remain observable for a long time after the ionizing source has been turned off due to the long recombination time of the interstellar gas ($\sim 10^5$ years). Searching for these ionized nebulae has been proven to be a powerful tool to constrain the progenitor channels of Type Ia supernovae.

In Chapter 2 we employed for the first time the method of searching for the ionized nebulae around young Type Ia supernova remnants directly with optical integral-field spectroscopic observations. We studied four different young remnants located in the Large Magellanic Cloud observed with the wide-field imaging spectrograph WiFeS on the 2.3m ANU telescope in Siding Spring Observatory (observation IDs: 4140118 and 4150145, PI: I. Seitenzahl). We focused especially on the He II 4686 Å emission line, which is a clear signature of an accreting and nuclear burning white dwarf, because the typical temperatures of these sources make them very efficient in ionizing Helium II. We did not detect an ionized nebula around any of the four supernova remnants and thus, in combination with photoionization simulations, we placed stringent upper limits on the temperature and luminosity of the progenitors of these supernova remnants before the explosion. These upper limits rule out the classical single degenerate progenitor scenario for these supernovae.

Despite the simple theoretical prediction, that every steadily accreting and nuclear burning white dwarf should create an ionized nebulae, only one such nebula has been detected so far around CAL83. While the favoured explanation is the low density of the surrounding interstellar medium and thus low surface brightness of the nebula, other possibilities exist also, such as time variability of the ionizing source and obscuration of the white dwarf emission by the circumstellar material. We observed many of these accreting white dwarfs with WiFeS in order to shed some light on the problem of missing ionized

nebulae. In Chapter 3 we present the results for one of the observed sources called LIN 358, which is a steadily accreting and nuclear burning symbiotic binary located in the Small Magellanic Cloud. We did not detect an ionized nebula around this source, but using the observations together with our newly develop method to simulate the optical spectrum of the ionized circumstellar material around the white dwarf with 2D photoionization simulations we were able to measure the properties of this system. Especially we measured the temperature and luminosity of the white dwarf, in addition to the mass-loss rate from the giant donor star, which allowed us also to estimate the mass-accretion rate on the white dwarf. With our simulations we also showed that despite the high density in the stellar wind of the donor star, the circumstellar material around the white dwarf is almost fully ionized and thus incapable to obscure the emission from the white dwarf significantly.

While in Chapter 3 we focused on one individual source, in Chapter 4 we expand those results to cover symbiotic binaries in general. We use the method developed in the previous chapter to employ the photoionization code CLOUDY to perform a large grid of 2D radiative transfer simulations. With this method we explore how the mass-loss rate from the donor star and the orbital separation affect the ionization and emission structure of the circumstellar medium around the ionizing white dwarf. In particular we model the emergent optical spectrum and the emission line luminosities of the symbiotic binaries and how these are affected by the system parameters. With these simulations grid we are able to generalise the results of Chapter 3 and show that in the majority of symbiotic binaries the stellar wind from the donor star is mostly ionized and so most of the emission from the white dwarf is able to escape the system freely. In addition we show how the wind mass-loss rate and the orbital separation determine the emission line ratios used for classification of different emission line objects. With our simulations we show in detail how e.g. the He I line ratios, which are used to classify the S- and D-type symbiotic binaries, depend on the orbital separation and thus affect the classification scheme. With this work we present a theoretical explanation for some of the observed phenomenology of symbiotic binaries and explain part of the varied observational appearances of these systems.

Although the long-standing problem of Type Ia supernova progenitors remains unsolved, our results presented here add to the growing evidence disfavouring the classical single degenerate progenitor scenario. While the single degenerate scenario remains plausible especially for some peculiar Type Ia supernovae, it seems that it cannot explain a large fraction of the supernova population. However, more work is needed to fully ascertain the contribution from the single degenerate channel. This is emphasised by the many uncertainties in the observed populations of accreting and nuclear burning white dwarfs. For example, the number of observed symbiotic binaries is only a few hundred, but theoretical works estimate that their number should be comparable to $\sim 0.5\%$ of the total red giant population of a galaxy, which in the Milky Way would mean a few $\times 10^5$ symbiotic binaries. Thus, while they are disfavoured as classical single degenerate progenitors due to the short lifetime of the donor stars, they contribute significantly to the population of white dwarf binaries. The increasing knowledge of their observational appearances makes searching for them more feasible and reduces the chance of misclassification, which together with the upcoming surveys gives hope that this situation will be resolved in the future.

Bibliography

Abate, C., Pols, O. R., Izzard, R. G., Mohamed, S. S., & de Mink, S. E. 2013, A&A, 552, A26

Abate, C., Pols, O. R., & Stancliffe, R. J. 2018, A&A, 620, A63

Akras, S., Gonçalves, D. R., Alvarez-Candal, A., & Pereira, C. B. 2021, MNRAS, 502, 2513

Akras, S., Guzman-Ramirez, L., Leal-Ferreira, M. L., & Ramos-Larios, G. 2019a, ApJS, 240, 21

Akras, S., Leal-Ferreira, M. L., Guzman-Ramirez, L., & Ramos-Larios, G. 2019b, MNRAS, 483, 5077

Allen, D. A. 1980, MNRAS, 190, 75

Allen, D. A. 1984, Proceedings of the Astronomical Society of Australia, 5, 369

Angeloni, R., Gonçalves, D. R., Akras, S., et al. 2019, AJ, 157, 156

Arnett, W. D. 1982, ApJ, 253, 785

Arrieta, A. & Torres-Peimbert, S. 2003, ApJS, 147, 97

Arthur, S. J. 2007, ApJ, 670, 471

Badenes, C., Hughes, J. P., Bravo, E., & Langer, N. 2007, ApJ, 662, 472

Badenes, C., Hughes, J. P., Cassam-Chenaï, G., & Bravo, E. 2008, ApJ, 680, 1149

Belczyński, K., Mikołajewska, J., Munari, U., Ivison, R. J., & Friedjung, M. 2000, A&AS, 146, 407

Belloni, D., Mikołajewska, J., Iłkiewicz, K., et al. 2020, MNRAS, 496, 3436

Bisnovatyi-Kogan, G. S. 1972, Azh, 49, 453

Bladh, S. & Höfner, S. 2012, A&A, 546, A76

Bladh, S., Höfner, S., Aringer, B., & Eriksson, K. 2015, A&A, 575, A105

Boffin, H. M. J. & Jorissen, A. 1988, A&A, 205, 155

Bondi, H. & Hoyle, F. 1944, MNRAS, 104, 273

Branch, D. & Tammann, G. A. 1992, ARA&A, 30, 359

Bray, I., Burgess, A., Fursa, D. V., & Tully, J. A. 2000, A&AS, 146, 481

Canal, R., Méndez, J., & Ruiz-Lapuente, P. 2001, ApJ, 550, L53

Chang, S.-J., Lee, H.-W., Lee, H.-G., et al. 2018, ApJ, 866, 129

Chen, H.-L., Woods, T. E., Yungelson, L. R., Gilfanov, M., & Han, Z. 2015, MNRAS, 453, 3024

Chen, X. & Han, Z. 2008, MNRAS, 387, 1416

Chen, Z., Frank, A., Blackman, E. G., Nordhaus, J., & Carroll-Nellenback, J. 2017, MNRAS, 468, 4465

Chiang, E. & Rappaport, S. 1996, ApJ, 469, 255

Childress, M., Vogt, F., Nielsen, J., & Sharp, R. 2014a, PyWiFeS: Wide Field Spectrograph data reduction pipeline, Astrophysics Source Code Library

Childress, M. J., Vogt, F. P. A., Nielsen, J., & Sharp, R. G. 2014b, Ap&SS, 349, 617

Chomiuk, L., Soderberg, A. M., Chevalier, R. A., et al. 2016, ApJ, 821, 119

Chomiuk, L., Soderberg, A. M., Moe, M., et al. 2012, ApJ, 750, 164

Cleveland, W. S. 1979, J. Am. Stat. Assoc., 74, 829

Corradi, R. L. M., Rodríguez-Flores, E. R., Mampaso, A., et al. 2008, A&A, 480, 409

Cummings, J. D., Kalirai, J. S., Tremblay, P. E., Ramirez-Ruiz, E., & Choi, J. 2018, ApJ, 866, 21

Davidsen, A., Malina, R., & Bowyer, S. 1977, ApJ, 211, 866

de Val-Borro, M., Karovska, M., & Sasselov, D. 2009, ApJ, 700, 1148

de Val-Borro, M., Karovska, M., Sasselov, D. D., & Stone, J. M. 2017, MNRAS, 468, 3408

Di Stefano, R. 2010, ApJ, 712, 728

Di Stefano, R., Voss, R., & Claeys, J. S. W. 2011, ApJ, 738, L1

Doherty, C. L., Gil-Pons, P., Siess, L., & Lattanzio, J. C. 2017, Publ. Astron. Soc. Australia, 34, e056

Doherty, C. L., Gil-Pons, P., Siess, L., Lattanzio, J. C., & Lau, H. H. B. 2015, MNRAS, 446, 2599

Dopita, M., Hart, J., McGregor, P., et al. 2007, Ap&SS, 310, 255

Dopita, M., Rhee, J., Farage, C., et al. 2010, Ap&SS, 327, 245

Dopita, M. A., Seitenzahl, I. R., Sutherland, R. S., et al. 2016, ApJ, 826, 150

Dougherty, S. M., Beasley, A. J., Claussen, M. J., Zauderer, B. A., & Bolingbroke, N. J. 2005, ApJ, 623, 447

Edwards, Z. I., Pagnotta, A., & Schaefer, B. E. 2012, ApJ, 747, L19

Eggleton, P. P. 1983, ApJ, 268, 368

Farias, D. A., Clocchiatti, A., Woods, T. E., & Rest, A. 2020, MNRAS, 497, 3234

Ferland, G. J., Chatzikos, M., Guzmán, F., et al. 2017, Rev. Mex. Astron. Astrofis., 53, 385

Filippenko, A. V. 1997, ARA&A, 35, 309

Fisher, A., Branch, D., Hatano, K., & Baron, E. 1999, MNRAS, 304, 67

Frank, J., King, A., & Raine, D. J. 2002, Accretion Power in Astrophysics: Third Edition (Cambridge University Press)

Ghavamian, P., Rakowski, C. E., Hughes, J. P., & Williams, T. B. 2003, ApJ, 590, 833

Ghavamian, P., Raymond, J., Hartigan, P., & Blair, W. P. 2000, ApJ, 535, 266

Ghavamian, P., Raymond, J., Smith, R. C., & Hartigan, P. 2001, ApJ, 547, 995

Ghavamian, P., Seitenzahl, I. R., Vogt, F. P. A., et al. 2017, ApJ, 847, 122
Gilfanov, M. & Bogdán, Á. 2010, Nature, 463, 924
Graur, O., Maoz, D., & Shara, M. M. 2014, MNRAS, 442, L28
Graur, O. & Woods, T. E. 2019, MNRAS, 484, L79
Greiner, J. 2000, New Astron., 5, 137
Grevesse, N., Asplund, M., Sauval, A. J., & Scott, P. 2010, Ap&SS, 328, 179
Groenewegen, M. A. T. & Sloan, G. C. 2018, A&A, 609, A114
Gromadzki, M. & Mikołajewska, J. 2009, A&A, 495, 931
Gromadzki, M., Mikołajewska, J., & Soszyński, I. 2013, Acta Astron., 63, 405
Gruyters, P., Exter, K., Roberts, T. P., & Rappaport, S. 2012, A&A, 544, A86
Gutierrez-Moreno, A., Moreno, H., & Cortes, G. 1995, PASP, 107, 462
Hachisu, I., Kato, M., & Nomoto, K. 1996, ApJ, 470, L97
Hachisu, I., Kato, M., & Nomoto, K. 1999, ApJ, 522, 487
Hamuy, M., Phillips, M. M., Suntzeff, N. B., et al. 2003, Nature, 424, 651
Hauschildt, P. H., Allard, F., Ferguson, J., Baron, E., & Alexander, D. R. 1999, ApJ, 525, 871
Hertfelder, M., Kley, W., Suleimanov, V., & Werner, K. 2013, A&A, 560, A56
Hillebrandt, W., Kromer, M., Röpke, F. K., & Ruiter, A. J. 2013, Frontiers of Physics, 8, 116
Hillman, Y., Prialnik, D., Kovetz, A., & Shara, M. M. 2016, ApJ, 819, 168
Hjellming, M. S. & Webbink, R. F. 1987, ApJ, 318, 794
Hoeflich, P., Khokhlov, A., Wheeler, J. C., et al. 1996, ApJ, 472, L81
Höfner, S. 2007, in Astronomical Society of the Pacific Conference Series, Vol. 378, Why Galaxies Care About AGB Stars: Their Importance as Actors and Probes, ed. F. Kerschbaum, C. Charbonnel, & R. F. Wing, 145
Höfner, S. 2015, in Astronomical Society of the Pacific Conference Series, Vol. 497, Why Galaxies Care about AGB Stars III: A Closer Look in Space and Time, ed. F. Kerschbaum, R. F. Wing, & J. Hron, 333
Höfner, S., Bladh, S., Aringer, B., & Ahuja, R. 2016, A&A, 594, A108
Höfner, S. & Olofsson, H. 2018, A&ARv, 26, 1
Hohle, M. M., Neuhäuser, R., & Schutz, B. F. 2010, Astronomische Nachrichten, 331, 349
Hoyle, F. & Lyttleton, R. A. 1939, Proceedings of the Cambridge Philosophical Society, 35, 405
Hughes, J. P., Hayashi, I., & Koyama, K. 1998, ApJ, 505, 732
Hummer, D. G. & Seaton, M. J. 1963, MNRAS, 125, 437
Hummer, D. G. & Storey, P. J. 1987, MNRAS, 224, 801
Iben, Jr., I. & Tutukov, A. V. 1984, ApJS, 54, 335
Iijima, T. 1981, in Photometric and Spectroscopic Binary Systems, ed. E. B. Carling & Z. Kopal, 517

Ikeuchi, S. & Ostriker, J. P. 1986, ApJ, 301, 522

Iłkiewicz, K. & Mikołajewska, J. 2017, A&A, 606, A110

Iłkiewicz, K., Mikołajewska, J., Belczyński, K., Wiktorowicz, G., & Karczmarek, P. 2019, MNRAS, 485, 5468

Indriolo, N., Geballe, T. R., Oka, T., & McCall, B. J. 2007, ApJ, 671, 1736

Johansson, J., Woods, T. E., Gilfanov, M., et al. 2014, MNRAS, 442, 1079

Jones, S., Röpke, F. K., Fryer, C., et al. 2019, A&A, 622, A74

Jones, S., Röpke, F. K., Pakmor, R., et al. 2016, A&A, 593, A72

Justham, S. 2011, ApJ, 730, L34

Kahabka, P. & Haberl, F. 2006, A&A, 452, 431

Kahabka, P. & van den Heuvel, E. P. J. 1997, ARA&A, 35, 69

Kniazev, A. Y., Pustilnik, S. A., & Zucker, D. B. 2008, MNRAS, 384, 1045

Kosenko, D., Helder, E. A., & Vink, J. 2010, A&A, 519, A11

Kosenko, D., Hillebrandt, W., Kromer, M., et al. 2015, MNRAS, 449, 1441

Kosenko, D., Vink, J., Blinnikov, S., & Rasmussen, A. 2008, A&A, 490, 223

Kuuttila, J., Gilfanov, M., Seitenzahl, I. R., Woods, T. E., & Vogt, F. P. A. 2019, MNRAS, 484, 1317

Kuuttila, J., Gilfanov, M., Woods, T. E., Seitenzahl, I. R., & Ruiter, A. J. 2021, MNRAS, 500, 3763

Lamers, H. J. G. L. M. & Cassinelli, J. P. 1999, Introduction to Stellar Winds (Cambridge University Press)

Leahy, D. A. & Leahy, J. C. 2015, Computational Astrophysics and Cosmology, 2, 4

Lee, H.-W. 2000, ApJ, 541, L25

Lee, H. W. & Lee, K. W. 1997, MNRAS, 287, 211

Lee, J. K., Rolleston, W. R. J., Dufton, P. L., & Ryans, R. S. I. 2005, A&A, 429, 1025

Leung, S.-C. & Nomoto, K. 2018, ApJ, 861, 143

Li, W., Bloom, J. S., Podsiadlowski, P., et al. 2011, Nature, 480, 348

Lindsay, E. M. 1961, AJ, 66, 169

Liu, Z. W., Pakmor, R., Röpke, F. K., et al. 2013, A&A, 554, A109

Long, K. S., Helfand, D. J., & Grabelsky, D. A. 1981, ApJ, 248, 925

Lü, G., Yungelson, L., & Han, Z. 2006, MNRAS, 372, 1389

Luna, G. J. M. & Costa, R. D. D. 2005, A&A, 435, 1087

Maggi, P., Haberl, F., Kavanagh, P. J., et al. 2016, A&A, 585, A162

Magrini, L., Corradi, R. L. M., & Munari, U. 2003, in Astronomical Society of the Pacific Conference Series, Vol. 303, Symbiotic Stars Probing Stellar Evolution, ed. R. L. M. Corradi, J. Mikolajewska, & T. J. Mahoney, 539

Maoz, D., Mannucci, F., & Nelemans, G. 2014, ARA&A, 52, 107

Margutti, R., Parrent, J., Kamble, A., et al. 2014, ApJ, 790, 52

Margutti, R., Soderberg, A. M., Chomiuk, L., et al. 2012, ApJ, 751, 134

Marietta, E., Burrows, A., & Fryxell, B. 2000, ApJS, 128, 615
Marquardt, K. S., Sim, S. A., Ruiter, A. J., et al. 2015, A&A, 580, A118
Matteucci, F. & Greggio, L. 1986, A&A, 154, 279
McConnachie, A. W. 2012, AJ, 144, 4
McKee, C. F. & Ostriker, J. P. 1977, ApJ, 218, 148
Merc, J., Gális, R., & Wolf, M. 2019, Research Notes of the American Astronomical Society, 3, 28
Mikołajewska, J. 2012, Baltic Astronomy, 21, 5
Mikolajewska, J., Acker, A., & Stenholm, B. 1997, A&A, 327, 191
Mitsuda, K., Inoue, H., Koyama, K., et al. 1984, PASJ, 36, 741
Mohamed, S. & Podsiadlowski, P. 2007, in Astronomical Society of the Pacific Conference Series, Vol. 372, 15th European Workshop on White Dwarfs, ed. R. Napiwotzki & M. R. Burleigh, 397
Mohamed, S. & Podsiadlowski, P. 2012, Baltic Astronomy, 21, 88
Muerset, U., Schild, H., & Vogel, M. 1996, A&A, 307, 516
Muerset, U., Wolff, B., & Jordan, S. 1997, A&A, 319, 201
Munari, U. 2019, arXiv e-prints, arXiv:1909.01389
Nazé, Y., Corcoran, M. F., Koenigsberger, G., & Moffat, A. F. J. 2007, ApJ, 658, L25
Ness, J.-U., Osborne, J. P., Henze, M., et al. 2013, A&A, 559, A50
Netzer, H. 1975, MNRAS, 171, 395
Nielsen, M. T. B. & Gilfanov, M. 2015, MNRAS, 453, 2927
Nielsen, M. T. B., Voss, R., & Nelemans, G. 2012, MNRAS, 426, 2668
Nomoto, K. 1984, ApJ, 277, 791
Nomoto, K. & Iben, I., J. 1985, ApJ, 297, 531
Nomoto, K. & Kondo, Y. 1991, ApJ, 367, L19
Nomoto, K., Saio, H., Kato, M., & Hachisu, I. 2007, ApJ, 663, 1269
Nugent, P. E., Sullivan, M., Cenko, S. B., et al. 2011, Nature, 480, 344
Nussbaumer, H., Schmid, H. M., & Vogel, M. 1989, A&A, 211, L27
Nussbaumer, H. & Vogel, M. 1987, A&A, 182, 51
Olling, R. P., Mushotzky, R., Shaya, E. J., et al. 2015, Nature, 521, 332
Orio, M., Zezas, A., Munari, U., Siviero, A., & Tepedelenlioglu, E. 2007, ApJ, 661, 1105
Osterbrock, D. E. & Ferland, G. J. 2006, Astrophysics of gaseous nebulae and active galactic nuclei (University Science Books)
Ostriker, J. P. & Ikeuchi, S. 1983, ApJ, 268, L63
Paczyński, B. 1971, ARA&A, 9, 183
Paczynski, B. 1976, in IAU Symposium, Vol. 73, Structure and Evolution of Close Binary Systems, ed. P. Eggleton, S. Mitton, & J. Whelan, 75
Pakmor, R., Hachinger, S., Röpke, F. K., & Hillebrandt, W. 2011, A&A, 528, A117
Pakmor, R., Kromer, M., Röpke, F. K., et al. 2010, Nature, 463, 61

Pakmor, R., Kromer, M., Taubenberger, S., et al. 2012, ApJ, 747, L10
Pan, K.-C., Ricker, P. M., & Taam, R. E. 2013, ApJ, 773, 49
Pellegrini, E. W., Oey, M. S., Winkler, P. F., et al. 2012, ApJ, 755, 40
Pequignot, D., Petitjean, P., & Boisson, C. 1991, A&A, 251, 680
Pereira, C. B., Landaberry, S. J. C., & Junqueira, S. 1998, A&A, 333, 658
Perlmutter, S., Aldering, G., Goldhaber, G., et al. 1999, ApJ, 517, 565
Phillips, M. M. 1993, ApJ, 413, L105
Phillips, M. M., Lira, P., Suntzeff, N. B., et al. 1999, AJ, 118, 1766
Podsiadlowski, P., Mazzali, P., Lesaffre, P., Han, Z., & Förster, F. 2008, New Astron. Rev., 52, 381
Podsiadlowski, P., Rappaport, S., & Pfahl, E. D. 2002, ApJ, 565, 1107
Popham, R. & Narayan, R. 1995, ApJ, 442, 337
Pringle, J. E. 1977, MNRAS, 178, 195
Pringle, J. E. & Savonije, G. J. 1979, MNRAS, 187, 777
Proga, D., Mikolajewska, J., & Kenyon, S. J. 1994, MNRAS, 268, 213
Ramstedt, S., Schöier, F. L., & Olofsson, H. 2009, A&A, 499, 515
Rappaport, S., Chiang, E., Kallman, T., & Malina, R. 1994, ApJ, 431, 237
Remillard, R. A., Rappaport, S., & Macri, L. M. 1995, ApJ, 439, 646
Rest, A., Matheson, T., Blondin, S., et al. 2008, ApJ, 680, 1137
Rest, A., Suntzeff, N. B., Olsen, K., et al. 2005, Nature, 438, 1132
Riess, A. G., Filippenko, A. V., Challis, P., et al. 1998, AJ, 116, 1009
Rodríguez-Flores, E. R., Corradi, R. L. M., Mampaso, A., et al. 2014, A&A, 567, A49
Ruiter, A. J., Ferrario, L., Belczynski, K., et al. 2019, MNRAS, 484, 698
Saio, H. & Nomoto, K. 1985, A&A, 150, L21
Saio, H. & Nomoto, K. 1998, ApJ, 500, 388
Saladino, M. I., Pols, O. R., & Abate, C. 2019, A&A, 626, A68
Saladino, M. I., Pols, O. R., van der Helm, E., Pelupessy, I., & Portegies Zwart, S. 2018, A&A, 618, A50
Schaefer, B. E. & Pagnotta, A. 2012, Nature, 481, 164
Schenck, A., Park, S., & Post, S. 2016, AJ, 151, 161
Schmid, H. M. 1989, A&A, 211, L31
Scowcroft, V., Freedman, W. L., Madore, B. F., et al. 2016, ApJ, 816, 49
Sekeráš, M. & Skopal, A. 2012, MNRAS, 427, 979
Sekeráš, M. & Skopal, A. 2015, ApJ, 812, 162
Shagatova, N., Skopal, A., & Cariková, Z. 2016, A&A, 588, A83
Shakura, N. I. & Sunyaev, R. A. 1973, A&A, 500, 33
Shappee, B. J., Stanek, K. Z., Pogge, R. W., & Garnavich, P. M. 2013, ApJ, 762, L5
Shen, K. J. & Bildsten, L. 2007, ApJ, 660, 1444
Silverman, J. M., Nugent, P. E., Gal-Yam, A., et al. 2013a, ApJS, 207, 3

Silverman, J. M., Nugent, P. E., Gal-Yam, A., et al. 2013b, ApJ, 772, 125
Skopal, A. 2005, A&A, 440, 995
Skopal, A. 2006, A&A, 457, 1003
Skopal, A. 2015, New Astron., 36, 116
Smith, R. C., Raymond, J. C., & Laming, J. M. 1994, ApJ, 420, 286
Strömgren, B. 1939, ApJ, 89, 526
Suleimanov, V., Hertfelder, M., Werner, K., & Kley, W. 2014, A&A, 571, A55
Umeda, H., Nomoto, K., Yamaoka, H., & Wanajo, S. 1999, ApJ, 513, 861
van den Heuvel, E. P. J. 1994, in Saas-Fee Advanced Course 22: Interacting Binaries, ed. S. N. Shore, M. Livio, E. P. J. van den Heuvel, H. Nussbaumer, & A. Orr, 263–474
van den Heuvel, E. P. J., Bhattacharya, D., Nomoto, K., & Rappaport, S. A. 1992, A&A, 262, 97
van der Heyden, K. J., Behar, E., Vink, J., et al. 2002, A&A, 392, 955
Vedel, H., Hellsten, U., & Sommer-Larsen, J. 1994, MNRAS, 271, 743
Vogt, F. P. A., Seitenzahl, I. R., Dopita, M. A., & Ghavamian, P. 2017a, A&A, 602, L4
Vogt, F. P. A., Seitenzahl, I. R., Dopita, M. A., & Ruiter, A. J. 2017b, PASP, 129, 058012
Walker, A. R. 1983, MNRAS, 203, 25
Wang, B. 2018, Research in Astronomy and Astrophysics, 18, 049
Webbink, R. F. 1984, ApJ, 277, 355
Weingartner, J. C. & Draine, B. T. 2001, ApJ, 548, 296
Whelan, J. & Iben, Jr., I. 1973, ApJ, 186, 1007
Wiersma, R. P. C., Schaye, J., & Theuns, T. 2011, MNRAS, 415, 353
Williams, B. J., Borkowski, K. J., Reynolds, S. P., et al. 2014, ApJ, 790, 139
Wolf, W. M., Bildsten, L., Brooks, J., & Paxton, B. 2013, ApJ, 777, 136
Woods, T. E., Ghavamian, P., Badenes, C., & Gilfanov, M. 2017, Nature Astronomy, 1, 800
Woods, T. E., Ghavamian, P., Badenes, C., & Gilfanov, M. 2018, ApJ, 863, 120
Woods, T. E. & Gilfanov, M. 2013, MNRAS, 432, 1640
Woods, T. E. & Gilfanov, M. 2016, MNRAS, 455, 1770
Woods, T. E. & Ivanova, N. 2011, ApJ, 739, L48
Woosley, S. E., Heger, A., & Weaver, T. A. 2002, Reviews of Modern Physics, 74, 1015
Yamaguchi, H., Badenes, C., Petre, R., et al. 2014, ApJ, 785, L27
Yaron, O., Prialnik, D., Shara, M. M., & Kovetz, A. 2005, ApJ, 623, 398
Yungelson, L. & Livio, M. 1998, ApJ, 497, 168
Yungelson, L. R. 2010, Astronomy Letters, 36, 780

Acknowledgements

I would like to thank Rashid Sunyaev for welcoming me in the High Energy group and supporting me during my studies. I am very thankful to Marat Gilfanov for all of his valuable guidance and support during the years, and without whom this thesis would not have been possible.

I would also like to thank my collaborates Tyrone Woods, Ashley Ruiter, Frederic Vogt and especially Ivo Seitenzahl, who helped me a lot with the observations that a big part of this thesis is based on.

A big thanks go also to all of my fellow students and friends that I met during these years in Munich and who made my time here much more memorable. A special thanks to Maria for all the great times and trips we had together.

Finally, I want to thank my family and especially my parents for all the love, support and encouragement that I have received during my whole life and which made it possible for me to reach for the stars.